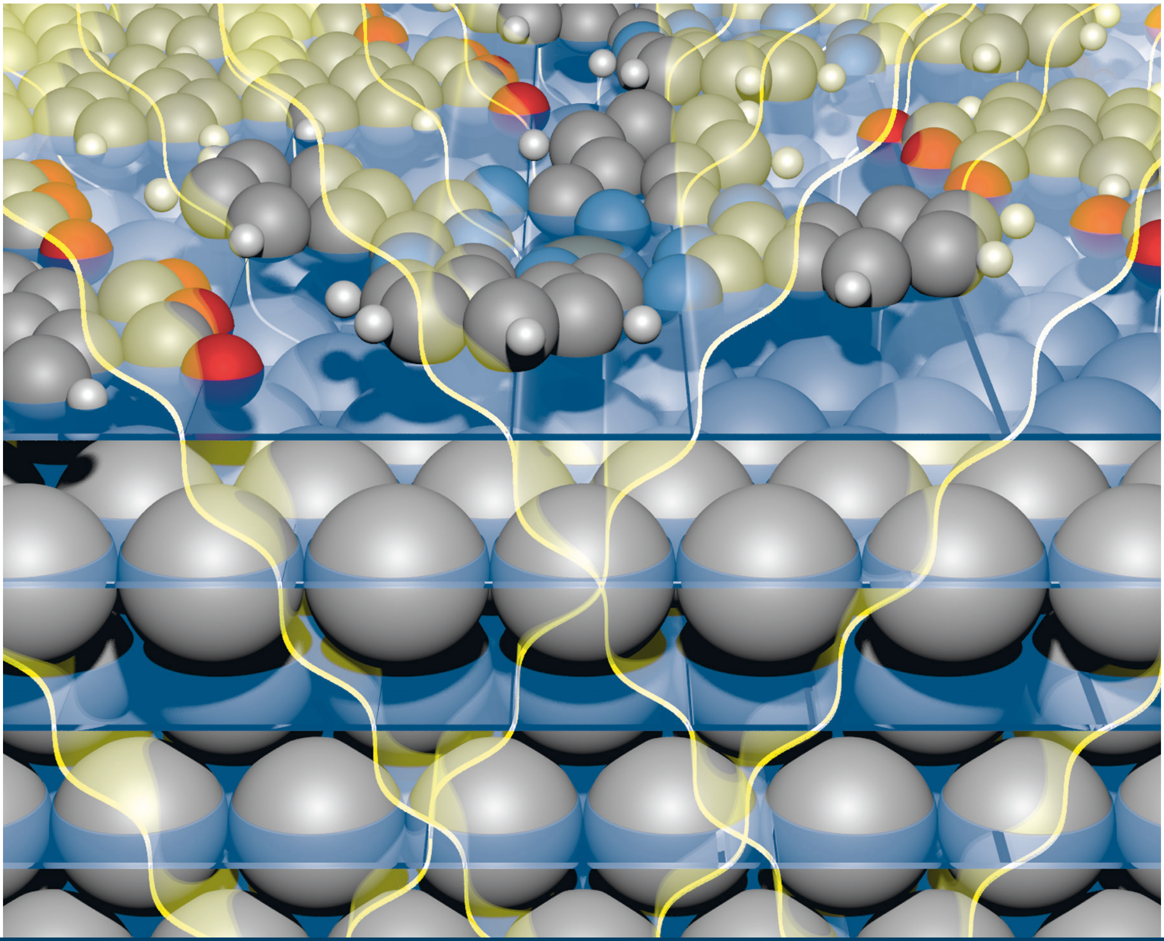

Geometric and Electronic Properties of Heteromolecular Organic Monolayers on Noble Metal Substrates Studied by Photoemission Spectroscopy and X-ray Standing Waves

Gerben van Straaten

Schlüsseltechnologien / Key Technologies
Band / Volume 235
ISBN 978-3-95806-539-0

Mitglied der Helmholtz-Gemeinschaft

JÜLICH
Forschungszentrum

Schriften des Forschungszentrums Jülich
Reihe Schlüsseltechnologien / Key Technologies Band / Volume 235

Forschungszentrum Jülich GmbH
Peter Grünberg Institut (PGI)
Quantum Nanoscience (PGI-3)

Geometric and Electronic Properties of Heteromolecular Organic Monolayers on Noble Metal Substrates Studied by Photoemission Spectroscopy and X-ray Standing Waves

Gerben van Straaten

Schriften des Forschungszentrums Jülich
Reihe Schlüsseltechnologien / Key Technologies Band / Volume 235

ISSN 1866-1807 ISBN 978-3-95806-539-0

Bibliografische Information der Deutschen Nationalbibliothek.
Die Deutsche Nationalbibliothek verzeichnet diese Publikation in der
Deutschen Nationalbibliografie; detaillierte Bibliografische Daten
sind im Internet über http://dnb.d-nb.de abrufbar.

Herausgeber und Vertrieb: Forschungszentrum Jülich GmbH
Zentralbibliothek, Verlag
52425 Jülich
Tel.: +49 2461 61-5368
Fax: +49 2461 61-6103
zb-publikation@fz-juelich.de
www.fz-juelich.de/zb

Umschlaggestaltung: Grafische Medien, Forschungszentrum Jülich GmbH

Druck: Grafische Medien, Forschungszentrum Jülich GmbH

Schriften des Forschungszentrums Jülich
Reihe Schlüsseltechnologien / Key Technologies, Band / Volume 235

D 82 (Diss. RWTH Aachen University, 2020)

ISSN 1866-1807
ISBN 978-3-95806-539-0

Abstract

The primary focus of this study was to analyze molecule-substrate and molecule-molecule interactions in heteromolecular monolayers on metallic substrates using a number of high precision experimental techniques capable of measuring the electronic and geometric properties of surfaces and ultrathin films. Therefore the first part of this works compares the geometric and electronic properties of two prototypical heteromolecular monolayer systems: CuPc+PTCDA/Ag(111) and SnPc+PTCDA/Ag(111). For one of these experimental techniques, the XSW technique, several issues were recognized that were caused by effects so far not recognized in the literature. As such, the second part of this thesis describes improved ways of analyzing NIXSW data, considering non-dipolar effects and the attenuation of the measured signal by inelastic scattering.

To elaborate, in the first section, we present a systematic study of the geometric and electronic properties of hetero-organic monolayers consisting of SnPc and PTCDA adsorbed on the Ag(111) surface and we compare these properties with those of monolayers containing CuPc and PTCDA. The geometric structures of these layers has been studied with LEED, STM and the NIXSW technique, while their electronic structure has been analyzed using ARPES data that has been analyzed using the photoemission tomography technique.

By comparing the two different systems, we gain insight into the influence of the phthalocyanine central metal atom on substrate-mediated interactions in phthalocyanine-PTCDA heteromolecular monolayers. It is observed that, in particular, the PTCDA anhydride groups are very sensitive to the central metal atom of the neighboring phthalocyanines. In addition to that, considerable differences in the phthalocyanine molecules are observed as well. First of all, in both systems charge transfer takes place from the phthalocyanine fLUMO to the PTCDA fLUMO. While this transfer is complete in the case of CuPc, leading to a complete depopulation of the fLUMO, the fLUMO of SnPc is pinned to the Fermi edge instead, causing it to be partially filled. Furthermore we observe that the adsorption height of SnPc is strongly altered after mixing with PTCDA, whereas no change in adsorption height can be observed for CuPc. We show that all these differences can be traced back to differences in the interaction between the phthalocyanine central metal atom

and the substrate.

Based on experience obtained during these measurements, it was realized that several assumptions underpinning the NIXSW method are not valid under realistic experimental conditions and in the second section of this work we reevaluate the theory of the NIXSW method. In particular, the correction factors that are used to account for non-dipolar effects in photoelectron-monitored NIXSW measurements are affected by small yet necessary deviations from perfect normal incidence. We have shown that neglecting these effects can lead to significant deviations and therefor new equations for the calculation of these correction factors are derived and the magnitude of the deviation caused by neglecting to account for the experimental geometry is analyzed for a variety of systems.

Finally, a second effect that is neglected in photoelectron-monitored NIXSW measurements is the limited mean-free path of the emitted photoelectrons. We show that under grazing emission conditions, the obtained parameters can deviate significantly from the true structural parameters and that these deviations are angle-dependent. As a result of this, angle-resolved NIXSW measurements taken close to grazing conditions contain additional information about the shape of the atomic distribution function at the substrate. Two methods for analyzing angle-resolved NIXSW data are presented, one best suited for recovering the layer spacing in multilayer systems, and one method suited for obtaining information about the shape of the distribution function of poorly ordered adsorbate layers.

Zusammenfassung

Das Hauptziel der vorliegenden Arbeit war die Untersuchung von Molekül-Substrat und Molekül-Molekül Wechselwirkungen in heteromolekularen Monolagen auf Metalloberflächen. Angewandt wurden hochauflösende experimentelle Techniken, die die elektronischen und geometrischen Eigenschaften von Oberflächen und ultradünnen Schichten bestimmen können. Dazu vergleicht der erste Teil dieser Arbeit die geometrischen und elektronischen Eigenschaften von zwei prototypischen heteromolekularen Monolagensystemen: CuPc+PTCDA/Ag(111) und SnPc+PTCDA/Ag(111). Für eine dieser experimentellen Techniken, die XSW Technik, wurden verschiedene Inkonsistenzen gefunden, verursacht durch bisher in der Literatur nicht beschriebene Effekte. Deshalb wurden im zweiten Teil dieser Arbeit Verbesserungen für die Analyse von NIXSW-Daten beschrieben, die nichtdipolare Effekte und die inelastische Streuung des Photoemissionssignals berücksichtigen.

Im ersten Teil dieser Arbeit wird eine systematische Untersuchung der elektronischen und geometrischen Eigenschaften hetero-organischer Monolagen präsentiert, bestehend aus adsorbierten SnPc und PTCDA Molekülen auf einer Ag(111)-Oberfläche. Diese Eigenschaften wurden mit Monolagen verglichen, die aus CuPc (statt SnPc) und PTCDA bestehen. Die geometrische Struktur dieser Schichten wurde mittels LEED, STM und NIXSW bestimmt, während die elektronischen Eigenschaften aus ARPES Daten ermittelt wurden, welche mittels Photoemissionstomographie ausgewertet wurden. Durch den Vergleich dieser zwei Systeme wird der Einfluss des Phtalocyanine-Zentralatoms auf die durch das Substrat vermittelte Molekül-Molekül Wechselwirkung in PTCDA-Phtalocyanine heteromolekularer Monolagen bestimmt. Es wurde festgestellt, dass die Anhydridgruppen der PTCDA Moleküle sehr empfindlich sind gegenüber den Zentralatomen der angrenzenden Phtalocyanine Molekle. Außerdem wurde eine signifikante Änderung der geometrischen und elektronischen Struktur des Phtalocyanines beobachtet. Zunächst findet in beiden Systemen ein Ladungstransfer vom Phtalocyanine fLUMO zu dem PTCDA fLUMO statt. Im Fall von CuPC ist der Ladungstransfer vollständig und das fLUMO ist unbesetzt. Im Gegensatz dazu kommt es im Fall von SnPc zum Ferminiveau-Pinning, weshalb das fLUMO von SnPc teilweise gefüllt ist. Des Weiteren wurde beobachtet, dass der Metall-SnPc Bindungsabstand sich durch Mischung mit PTCDA stark ändert, während hingegen die Beigabe von CuPc zu PTCDA nicht zu einer messbaren Änderung von des Metall-CuPc Bindungsabstandes führt. Wir weisen nach, dass diese Unterschiede gemeinsam durch unterschiedliche Wechselwirkungen zwischen dem Substrat und dem Zentralatom von die Phthalocyaninemolekülen zu erklären sind.

Die während dieser Untersuchungen gesammelten Erfahrungen zeigen, dass verschiedene Annahmen hinter der NIXSW-Technik für realistische experimentelle Bedingungen nicht zu rechtfertigen sind. Insbesondere die Korrekturfaktoren, die benötigt werden, um nichtdipolare Effekte in Photoemissions-basierten NIXSW Messungen zu kompensieren, wurden durch kleine jedoch notwendige Abweichungen vom perfekten senkrechten Einfall des Röntgenstrahls beeinflusst. Deshalb wurden neue Gleichungen für diese nichtdipolaren Korrekturfaktoren abgeleitet und die Größe des Fehlers, der durch die Vernachlässigung dieser Effekte entsteht, für verschiedene Systeme analysiert.

Ein zweiter, bisher unberücksichtigter Effekt in NIXSW Messungen ist die begrenzte mittlere freie Weglänge der emittierten Photoelektronen. In dieser Arbeit wird gezeigt, dass unter streifenden Emissionsbedingungen die erhalten geometrische Parameter starke Abweichungen von den realen Werten zeigen können, und dass diese Abweichungen winkelabhängig sind. Deshalb enthalten winkelaufgelöste NIXSW Messungen unter streifenden Emissionsbedingungen zusätzliche Information ber die Form der Verteilungsfunktion der Atome in der Nähe der Substratoberfläche. Zwei Methoden für die Analyse von winkelaufgelösten NIXSW-Daten werden präsentiert, wovon die erste prädestiniert ist, den Ebenenabstand in Multilagensystemen zu bewerten und die zweite am besten genutzt werden kann, um Information über die Form der Verteilungsfunktion von (vertikal) nicht perfekt geordneten Monolagen zu erhalten.

List of Acronyms

A_2B phase heteromolecular phase containing 2 PTCDA and 1 MePc molecule.

A_2B_2 phase heteromolecular phase containing 2 PTCDA and 2 MePc molecules.

AB phase heteromolecular phase containing 1 PTCDA and 1 MePc molecule.

AB_2 phase heteromolecular phase containing 1 PTCDA and 2 MePc molecules.

ARPES angle-resolved photoelectron spectroscopy.

CBE constant binding energy.

CuPc copper-II-phtalocyanine.

DFT density functional theory.

fLUMO former lowest unoccupied molecular orbital.

HOMO highest occupied molecular orbital.

IAC independent atomic center.

LEED low energy electron diffraction.

LEEM low energy electron microscopy.

LT-STM low temperature scanning tunneling microscopy.

LUMO lowest unoccupied molecular orbital.

MePc metal-phtalocyanine.

NIXSW normal-incidence x-ray standing wave.

NTCDA naphthalene-1,4,5,8-tetracarboxylicdianhydride.

PDOS projected density of states.

PES photoelectron spectroscopy.

PFP perfluoropentacene.

PTCDA perylene-3,4,9,10-tetracarboxylicdianhydride.

PW plane-wave.

SnPc tin-II-phtalocyanine.

SPA-LEED spot profile analysis – low energy electron diffraction.

STM scanning tunneling microscopy.

STS scanning tunneling spectroscopy.

TNCQ tetracyanoquinodimethane.

TTF tetrathiafulvalene.

UPS ultraviolet photoelectron spectroscopy.

XPS x-ray photoelectron spectroscopy.

XSW x-ray standing wave.

Contents

Chapter 1

Introduction

Inorganic-organic interfaces play a central role in organic semiconductor devices such as Organic Field-Effect Transistors (OFETs)[1–6], Organic Photovoltaics (OPVs)[7–12] and Organic Light Emitting Diodes (OLEDS)[13–18], which show promise as low-cost alternatives to devices based on silicon or germanium[19]. In these devices, the contact between an electrode and the organic molecules making up the active layer affects the charge extraction or injection barriers, as well as the location of the valence- and conduction bands relative to the Fermi level[20], which in turn strongly affects device characteristics such as the on/off ratio, energy conversion efficiency or luminosity. In addition to these electronic effects, the growth behavior of the active layer can also depend strongly on the behavior of the first few layers of molecules deposited on the inorganic substrate[21], which is of great importance due to the strong relation between the microstructure of the active layer and its microelectronic properties[5,7,10,22].

These interfaces are usually buried and therefore hard to study directly. In addition to that, in real devices the growth conditions of both the organic and inorganic part are often poorly controlled, making real devices unsuited for fundamental studies of the behavior of organic semiconductor molecules on inorganic surfaces. Instead, researchers have focused on a variety of model systems deposited on well-defined surfaces under tightly controlled conditions. Typically, these systems are produced by depositing molecules onto single-crystal substrates under ultrahigh vacuum conditions. Deposition of a monolayer (or less) directly exposes the interface, whereas the use of well-defined surfaces and tightly controlled growth conditions allowed for the formation of highly regular and well-defined structures.

Examples of popular model systems are planar, aromatic hydrocarbons such as perylene-3,4,9,10-tetracarboxylicdianhydride (PTCDA)[23–38], naphthalene-1,4,5,8-tetracarboxylicdianhydride (NTCDA)[39–44] or phthalocyanines[45–59] deposited on noble metal surfaces. These systems are of particular interest because aromatic hydrocarbons are the most common type of molecules used in organic electronic devices. In addition to that, on noble metal surfaces, they usually adsorb with the π-system parallel to the surface and since the interaction between the molecules and the metal surface is of a strength comparable to the lateral interaction between the molecules, these systems display a wide variety of phase and growth behaviors.

While these studies have contributed significantly to the understanding of the growth of organic thin films of a single type of molecule on metal surfaces, many organic electronic devices employ a mixture of two or more components to form what is known as a bulk heterojunction. The formation of mixed monolayers of PTCDA and copper-II-phtalocyanine (CuPc) was already reported as early as 2003[60], but only recently has the attention for such mixed systems started to increase. Recent work performed by our group[61–65], as well as the group of Dr. E. Ortega[66–70] has revealed a particular surprising behavior in binary heteromolecular monolayers consisting of donor and acceptor molecules. On the one hand, there is a transfer of charge from the donor molecule to the acceptor molecule, which appears to weaken the bond between the substrate and the donor molecule while simultaneously strengthening the bond between the substrate and the acceptor molecule. However, at the same time, upon measuring the substrate-adsorbate bond length, in all cases studied so far it has been observed that the acceptor molecule is further away from the substrate in the mixed phases than in its homomolecular phase, implying a weakening of the substrate-molecule bond upon mixing. This presents a clear paradox, since there are two measures of molecule-substrate bond strength that change in conflicting ways upon formation of a mixed phase. Stadtmüller *et al.*[64] showed that this paradox can be resolved by assuming that the donor molecule used in their studies (CuPc) pushes electron density from its adsorption site towards the acceptor adsorption site, which both leads to a transfer of charge into the PTCDA molecule and a lifting of the molecule due to Pauli repulsion, and they successfully applied this model to explain both CuPc+PTCDA mixed systems and mixed systems consisting of CuPc and NTCDA. However, while this model is successful in explaining the behavior of this particular system, it is not yet clear how it can be generalized to systems containing other donor molecules. In order to develop this model into a more general theory that can be used to analyze the behavior of heteromolecular monolayer systems, a critical comparison of multiple systems with different donor molecules is necessary.

One particular problem in studying substrate-mediated interactions in heteromolecular systems is that a change of the properties of one of the molecules often leads to a change in the packing of the mixed layers. For example, the lateral structures of CuPc+PTCDA mixed monolayers differ significantly from the later structures found in CuPc+NTCDA mixed monolayers. This means that it is generally speaking difficult to disentangle changes in the molecular interactions caused by varying the properties of the molecules from changes in the interactions caused by changing the adsorption sites or relative packing of the molecules. After a short overview of the used experimental techniques in chapter 2, a way will be presented to overcome this limitation. In chapter 3, measurements of the lateral and vertical geometry, as well as the electronic structure of mixed monolayers consisting of tin-II-phtalocyanine (SnPc) and PTCDA are presented. These results are compared to the geometric and electronic properties of PTCDA + CuPc mixed monolayers. It will be shown that changing the central metal atom of the donor molecule, i.e. going from CuPc to SnPc, only has a small effect on the direct intermolecular interactions and as a result of this it is possible to produce PTCDA + CuPc mixed systems that display the same lateral ordering as known from the PTCDA + CuPc system. By comparing systems with the same lateral structure it is then shown that the donor central metal atom noticeably affects the substrate-mediated interactions and that the PTCDA anhydride groups are particularly sensitive to the central metal atom of the neighboring phthalocyanine molecules. Further more, it is shown that the effect of the formation of mixed structures on SnPc differs considerably from the effect on CuPc. On the one hand, in the case of CuPc, the substrate-molecule bond length is largely unaffected by the presence or absence of PTCDA molecules in the layer and charge transfer from CuPc to PTCDA is complete. On the other hand, for SnPc it is found that charge transfer is incomplete whereas the substrate-molecule bond length changes considerably upon mixing with PTCDA. Finally, in this chapter, it is shown how these changes can be rationalized in the context of the electron density redistribution model.

As noted above, in order to fully understand molecular adsorbate systems in general, and substrate mediated interactions in particular, the substrate-molecule bond length must be measured with the highest possible precision. The most accurate and generally applicable technique for this purpose is the normal-incidence x-ray standing wave (NIXSW) technique. It allows for a direct determination of the substrate-adsorbate molecule distance without the need of a prior model and it is unaffected by lateral disorder or a lack of correlation between the adsorbate lateral structure and the structure of the substrate. As such, all possible sources of distortions must be accounted for. In chapter 4 it will be shown that distortions caused by deviations from perfect normal incidence can, contrary to what has been assumed so far, cause the measured data to deviate considerably from the actual physical parameters of the system. The origins of these distortions are identified as stemming from a change in the polarization direction of the incoming and outgoing beam that occurs under realistic measurement conditions but has so far been neglected in deriving the necessary correction parameters to account for non-dipolar effects in NIXSW measurements. In order to account for this, the aforementioned correction parameters are rederived taking this change of polarization direction into account and the difference between accounting and neglecting the change of the beam's polarization direction is quantified for a variety of systems.

In the 5th chapter, further improvements of the NIXSW technique are discussed. In this chapter it is shown that the photoemission signals that are typically used to record NIXSW data can be affected significantly by the limited mean-free path of electrons in solids. As a result of this, for measurements performed under conditions close to grazing emission, the obtained NIXSW data points can become strongly angle-dependent, especially for multilayer systems. This presents an additional degree of freedom which can be exploited to obtain information about the distribution of atoms at the surface. A general mathematical framework for dealing with such an angle-dependence is presented and from it, two different strategies are derived for analyzing angle-resolved NIXSW data, one of which can be applied to directly obtain the adsorption positions in the case of well-ordered multilayer systems, and another strategy that can be used to obtain information about the shape of the atomic distribution function in case of significant disorder.

Finally, in chapter 6 all findings are summarized.

Chapter 2

Experimental techniques

In this work, a number of different experimental techniques are employed to study the geometric as well as electronic properties of organic adsorbates on noble metal surfaces, and in addition to that, the state of the art of one particular technique, the NIXSW technique, is pushed forward. As such, in this chapter, a brief review of the basic principles of the employed techniques will be given, which will serve both as a sufficient background to understand the experimental results and as a starting point for the discussion of the presented advances in the NIXSW technique. Since all these methods are well-established and routinely used, this chapter does not aim to provide a full review, but rather it focuses on the specific aspects necessary to understand the further chapters.

2.1 Low-energy electron diffraction

Due to its experimental simplicity and its ability to solve complex surface structures, low energy electron diffraction (LEED) is one of the most popular experimental techniques for studying the lateral structure of crystalline surfaces[71]. It takes advantage of the fact that electrons with a kinetic energy in the range of 20 eV to 500 eV have a de Broglie wavelength (λ_{dB}) that ranges from 0.6 Å to 2.7 Å and an inelastic mean free path lower than 10 Å. This has two beneficial effects. First of all, since the wavelength of these electrons is comparable to interatomic distances, they can be used for scattering experiments with atomic resolutions. In addition to that, because of their low mean-free path, such experiments are very sensitive to the first few atomic layers of the surface being studied[71]. Taken together, this means that LEED is very sensitive to the crystalline structure of the top few atomic layers of a solid.

The simplest way to treat electron scattering is via the so-called kinematic diffraction theory[65,71,72]. It is assumed that any scattered electrons picked up by the detector have only been scattered once. Similar to other diffraction techniques such as x-ray diffraction, the distribution of diffraction maxima then corresponds to the reciprocal lattice of the probed solid. However, due to the very low penetration depth of low energy electrons, along the direction pointing into the bulk only a very small part of the lattice is probed. This means that along this direction the scattered electron waves do not add up to sharp spots. Instead, they are strongly broaden, forming so-called Ewald rods, along which the intensity varies smoothly. A further simplification, called the geometric scattering theory, is then to only focus on the location of these Ewald rods. Since the probed structure is still periodic in the plane of the surface, the positions of the Ewald rods in reciprocal space corresponds to the 2-dimensional reciprocal lattice in the plane of the surface. If there are multiple 2-dimensional reciprocal lattices present, which for example occurs when an adsorbate adopts a structure different from that of the substrate or when the top layer of the substrate undergoes reconstruction, then the Ewald rods of both lattices will be visible, although some rods might coincide.

Information about the arrangement of atoms along the direction pointing into the bulk can be obtained from the variation of scattering intensities along the Ewald rods, which can be measured via LEED-IV measurements[73–75]. During these measurements, the Ewald sphere is scanned through the Ewald rods by varying the energy of incoming electrons and the intensity of the diffraction spots is recorded. Unfortunately, at this point the kinematic diffraction theory breaks down. The strong interaction of low-energy electrons with matter leads to a high probability for electrons to be scattered multiple times before reaching the detector, meaning that the use of dynamic diffraction theory becomes necessary. As it turns out, multiple scattering does not affect the expected position of the Ewald rods in the plane of the surface, explaining the usefulness of kinematic scattering theory for determining the 2-dimensional reciprocal lattice. However, it strongly affects the intensity distribution along the Ewald rods. Unfortunately, due to the complex nature of the multiple scattering process, it is neither possible to calculate the 3-dimensional distribution of atoms in the sample directly from the intensity variation along the Ewald rods, nor is it possible to use the simple and computationally cheap kinematic scattering theory to calculate them for an expected structure. In order to obtain structure information from intensity variation measurements (also referred to as LEED-IV), one has to assume a model for the distribution of atoms at the surface, calculate the expected intensity variation for the visible spots in the LEED images using dynamic diffraction theory, compare these intensity variations to the measured intensity variations and adjust the model until a satisfactory level of similarity between the measured and simulated IV curves is obtained.

The systems studied in this work however, all show very large unit cells with many atoms per unit cell. As such, application of LEED-IV for these systems is at present impossible, since the computational effort that would be necessary to determine the full 3-dimensional structure of these systems is practically unattainable at this point. As such, we will restrict ourselves to analyzing the obtained LEED data using geometric scattering theory for the analysis of the lateral structure (i.e. parallel to the surface). We take advantage of the fact that the positions of the Ewald rods $\vec{a}_i^*$ in reciprocal space can be related directly to the lattice parameters $\vec{a}_i$ of the real-space structure via the equation $\vec{a}_i\vec{a}_j^* = 2\pi\delta_{ij}$. Thus, if the positions of the Ewald rods can be determined then the unit cell of the adsorbate layer can be determined directly. In the case of crystalline adsorbate layers on crystalline surfaces, it is useful to describe the adsorbate structure in relation to the substrate structure. The superstructure matrix **S**, which is a 2×2 matrix defined as:

$$\begin{pmatrix} \vec{A} \\ \vec{B} \end{pmatrix} = \mathbf{S} \begin{pmatrix} \vec{a} \\ \vec{b} \end{pmatrix}, \tag{2.1}$$

relates the lattice vectors $\vec{A}$ and $\vec{B}$ of the adsorbate layer to the lattice vectors $\vec{a}$ and $\vec{b}$ of the substrate[76]. However, since most substrates belong to a non-trivial symmetry group, a surface will typically be covered by a multitude of symmetry-equivalent adsorbate crystals, each having its own orientation and each of these crystals has its own superstructure matrix. In particular, if the underlying substrate has a 3-fold rotation symmetry, as well as a mirror symmetry, then there are a total of 6 different ways of orienting the adsorbate layer that are, because of the symmetry of the substrate, completely equivalent. Thus, unless a LEED variant capable of measuring only a single domain, such as μ-LEED[77] is used, the observed LEED pattern will contain approximately equal contributions of all these crystallites. In such a case, it is typical to determine and report the superstructure matrix **S** for only one orientation in conjunction with the substrate, which together is sufficient to reconstruct the lattice vectors of all domains present on the surface. Since the choice as to which of the matrices is reported is made largely arbitrarily, this does leave some ambiguity that should be taken into account when comparing structures based on the superstructure matrix.

Superstructure matrices are typically determined by simulating the expected locations of diffraction spots in a LEED image for a trail superstructure, taking into account the presence of differently oriented but otherwise equivalent domains. In this study, the program Spotplotter[78] developed by Patrick Bayersdorfer has been used. After the expected diffraction spot locations have been calculated they are overlaid on the experimentally obtained LEED image. Then, the trial superstructure is adjusted manually and the diffraction spots are recalculated. This procedure is repeated until a satisfactory coincidence between the calculated and experimentally obtained spot locations is obtained.

One advantage of using superstructure matrices is that it allows quick identification of the epitaxial relationship between an adsorbate layer and the underlying substrate. This epitaxial relationship can generally be described as disordered, commensurate, point-on-line or incommensurate[79]:

- A disordered adsorbate layer does not have a regular long-range structure, although the adsorbates themselves may adsorb in well-defined adsorption sites. As a disordered adsorbate layer has no periodic structure, no superstructure matrix can be defined for these systems.
- An incommensurate structure also shows no relation to the underlying substrate but unlike disordered structures, incommensurate structures are well-ordered[80]. This occurs when the interaction between the substrate and the adsorbate layer is much weaker than the interaction between the adsorbates in the layer itself. In such a situation, which occurs among others for near-monolayer coverage of CuPc on Au(111)[47] the lattice points of the real-space lattice of the adsorbate structure do not coincide with the real-space lattice points of the substrate and as a result of this, all entries in the superstructure matrix of this layer are irrational.
- In a commensurate structure, the interaction between the adsorbates and the surface is strong enough so that adsorbates adsorb in well-defined adsorption sites. As a result of this, lattice sites of the real-space adsorbate lattice will coincide with lattice sites of the real-space substrate lattice and this results in a superstructure matrix that contains only integer numbers. Examples of this kind of coincidence are PTCDA on Ag(111)[24] and a low-temperature phase occurring for submonolayer coverage of CuPc on Ag(111)[81]. A similar situation, also commonly referred to as commensurate occurs when a fraction of the lattice spots of the adsorbate layer coincide with lattice spots of the substrate (e.g. every other lattice spot of the adsorbate layer coincides with a lattice spot of the substrate), in which case all matrix elements are rational. In that case, one can always define an expanded unit cell that does correspond to a truly commensurate structure as defined here. Note that in practice, only small integer ratios are considered since large integer ratios are experimentally indistinguishable from irrational numbers.
- Finally, a point-on-line structure is very similar to an incommensurate in the sense that there is no coincidence between the lattice spots of the real-space adsorbate and substrate lattice. However, unlike with the incommensurate structures, there is a relation between the substrate and adsorbate layer because the lattice spots of the adsorbate layer coincide with lines connecting the lattice spots of the substrate layer[79]. In such a case, which occurs for example for PTCDA on Au(111)

and Au(100)[23], either the terms along one row or one column in the superstructure matrix add up to an integer.

2.1.1 SPA-LEED

Conventional LEED systems project the backscattered electrons onto a plate detector such as a fluorescent screen. Such systems have the advantage that the entire image can be obtained at once, but they require fairly high electron fluxes to ensure a sufficiently high contrast. In contrast to these conventional LEED setups, a spot profile analysis – low energy electron diffraction (SPA-LEED) system, like the one schematically depicted in fig. 2.1a uses a single, high-resolution electron multiplier, typically a channeltron, installed at a fixed angle with respect to the electron gun[82]. Octupole plates are used to deflect both the electrons that have been emitted by the electron gun, and those that have been backscattered. By scanning the voltage applied to these octupole plates, the electrons scattered back into the SPA-LEED can be scanned over the channeltron and in that way a 2-dimensional image similar to those obtained by a plate detector can be constructed, with the caveat that inhomogeneities in the octupole field lead to distortions of the diffraction patterns at large deflections of the electron beam.

The operating principle of a SPA-LEED is further illustrated in the modified Ewald construction in fig. 2.1b. The angle between the momentum vectors describing the electrons impinging on the sample (solid lines) and those that are diffracted back into the direction of the channeltron (dashed lines) is fixed by the placement of the channeltron relative to the electron gun. By scanning the octupole plate voltage, the momentum vector of the impinging electrons is rotated relative to the Ewald rods of the surface and at a fixed electron kinetic energy it thus traces out a part of a circle. By additionally varying the voltage across the plates in the direction perpendicular to the one depicted (i.e. in the direction normal to the page), this arc is extended to part of a sphere and 2-dimensional scattering patterns can be recorded.

One of the most important advantages of a channeltron detector is its large dynamic detection range. This means that high contrast scans can be obtained using an electron flux that is much lower than the fluxes typically used for LEED devices equipped with a plate detector. Since measurements can be done with a low electron flux, it becomes possible to make high resolution scans of materials that are sensitive to radiation damage, such as monolayers of organic adsorbates.

A second important advantage is the increased lateral resolution of a SPA-LEED compared to a conventional LEED. The lateral resolution $\frac{k}{\Delta k}$ of a diffraction experiment is determined by the ratio of the aperture in front of the detector to the distance between the sample and the detector. A typical SPA-LEED has both a smaller aperture (0.1 mm vs. 0.5 mm) and a larger

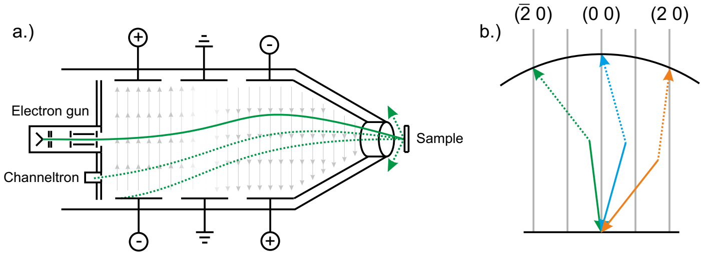

Figure 2.1: a.) Schematic cross-section of a SPA-LEED instrument in operation, depicting the beam generated by the electron gun (green, solid line) being deflected by the field applied between the octupole plates before impinging on the sample. These incoming electrons are then diffracted under various angles, with one of the diffracted beams reaching the channeltron. b.) Modified Ewald construction for SPA-LEED instruments. The angle between the momentum vectors of the impinging electrons (solid line) and the electrons reaching the channeltron (dashed line) is fixed by the relative placement and orientation of the electron gun and channeltron (typical angles are between 4° and 7°, value exaggerated here for clarity). By varying the voltage applied to the octupole plates, the angle that the impinging beam makes with the surface (and thus with the Ewald rods depicted as gray lines) is varied and in this way the scattering vector is scanned along the depicted arc, which becomes a section of a sphere if deflections in 2 dimensions are included.

working distance (300 mm vs. 75 mm) than a typical LEED equipped with a plate detector, resulting in a lateral resolution that is approximately 20 times greater[83]. This enhanced lateral resolution results in an increased transfer width and as a result of this, in many cases, the instrumental broadening of the Ewald rods becomes significantly smaller than the broadening caused by defects in the measured structure. Spot profile analysis can then be used to obtain information about the concentration and kind of defects present[84] and it is because of this possibility that a LEED equipped with a channeltron is called a SPA-LEED. However, a second benefit of such a high resolution is that it allows for the identification of small changes in spot positions and to distinguish spots that would otherwise overlap in an image taken with a conventional LEED. This makes a SPA-LEED exceptionally well-suited for the study of systems with large unit cells, which includes organic adsorbate layers since the size of their unit cells must be at least the size of a single molecule.

2.2 Photoelectron spectroscopy

Photoelectron spectroscopy (PES) relies on the removal of electrons from, among others, crystalline solids or molecules using monochromatized UV or x-ray photons in a process known as the photoelectric effect. The so-called photoelectrons created this way are subsequently analyzed and their kinetic energy and momenta can be used to obtain information about the electronic and chemical properties of the studied species.

In a photoemission experiment, the target, for example a molecule, is in an initial state described by the wave-function Ψ_i. After interaction with a photon with energy $\hbar\omega$, an electron is ejected and the combined state of the ejected photoelectron and the now ionized target is described by the wave-function Ψ_f. Furthermore it is assumed that the outgoing electron has a high enough velocity that interactions with the hole left on the target can be neglected. The transition probability w is then given by Fermi's golden rule[85]:

$$w \propto \frac{2\pi}{\hbar}\left|\left\langle \Psi_f \,\middle|\, \hat{\mathbf{\Delta}} \,\middle|\, \Psi_i \right\rangle\right|^2 \delta(E_f - E_i - \hbar\omega). \tag{2.2}$$

Here E_i and E_f are the energy of the intitial and final state respectively and the Dirac delta function, δ, has been used to ensure energy conservation. $\hat{\mathbf{\Delta}}$ is the photoemission operator, which has the following form:

$$\hat{\mathbf{\Delta}} = \frac{e}{2mc}(\mathbf{A}\hat{\mathbf{p}} + \hat{\mathbf{p}}\mathbf{A}) + \frac{e^2}{2mc^2}\mathbf{A}\mathbf{A}. \tag{2.3}$$

In this equation, the photon is described by the vector potential $\mathbf{A}$, which interacts with the momentum operator $\hat{\mathbf{p}}$ of the electron system. Usually, photoemission spectroscopy is done with photon fluxes at which two-photon transitions, corresponding to the term $\frac{e^2}{2mc^2}\mathbf{A}\mathbf{A}$, can be neglected. Further more, $\hat{\mathbf{p}} = i\hbar\vec{\nabla}$ and if the Coulomb Gauge is used, then $\vec{\nabla}\mathbf{A} = 0$, so the term containing $\hat{\mathbf{p}}\mathbf{A}$ can be neglected as well. This then leads to the following, simplified expression for $\hat{\mathbf{\Delta}}$:

$$\hat{\mathbf{\Delta}} = \frac{e}{mc}\mathbf{A}\hat{\mathbf{p}}. \tag{2.4}$$

Finally, if photons are used with a sufficiently low energy, the wavelength of those photons is much larger than the size of the orbitals involved in photoemission. In that case, $\mathbf{A}$ is effectively constant over the volume contributing to photoemission and can be replaced by a constant vector potential $\mathbf{A_0}$. This is commonly referred to as the dipole approximation.

In the simplest approximation, the initial and final state wave functions can be split into a part depending only on the photoelectron that is emitted and a part that depends on the $N-1$ electrons that were not emitted in the following way:

$$\Psi_i = \phi_i \psi_i^{N-1}, \tag{2.5}$$
$$\Psi_f = \phi_f \psi_i^{N-1}. \tag{2.6}$$

Equation 2.2 can then be rewritten into:

$$w \propto \left|\langle \phi_f \,|\, \mathbf{A_0}\hat{\mathbf{p}} \,|\, \phi_i \rangle\right|^2 \left|\left\langle \psi_f^{N-1} \,\middle|\, \psi_i^{N-1} \right\rangle\right|^2 \delta\Big(E_{kin} + E_f^{N-1} - E_i^N - \hbar\omega\Big), \tag{2.7}$$

with E_{kin} the kinetic energy of the emitted photoelectron, E_f^{N-1} the energy of the ionized target that stays behind and E_i^N the energy of the target prior to photoemission. Since photoemission is only possible if the argument of δ in equation eq. 2.7 evaluates to 0, one can write the following relation between the kinetic energy of the photoelectron and the energy of the photon used to excite the target:

$$E_{kin} = \hbar\omega - (E_f^{N-1} - E_i^N). \tag{2.8}$$

In the so-called frozen orbital approximation it is assumed that the effect of the $N-1$ electron system relaxing on photoemission can be neglected. In other words, during photoemission $\psi_i^{N-1} = \psi_f^{N-1}$ and any relaxations take place on time scales that are much longer than the time needed for the photoelectron to leave the target. In that case, one can write $E_i^N = E_i^{N-1} + (E_b + \Phi)$ with E_b the binding energy of the one-electron orbital from which the photoelectron originated and Φ the work function, which cannot be neglected if the target is a solid itself or if it is in close proximity to a solid. The binding energy of the emitted photoelectron, which in the frozen approximation is exactly equal to the binding energy of the orbital it originated from, is then equal to:

$$E_b = \hbar\omega - E_{kin} - \Phi. \tag{2.9}$$

However, both organic thin films and metal substrates tend to be highly polarizable. As a result of this, holes created by photoemission of an electron from an organic adsorbate are screened[83,86]. This means that relaxation of ψ_f^{N-1} of an organic adsorbate is usually rapid compared to the time needed for the photoelectron to leave the system. As a result of this, the relation between the kinetic energy of the photoelectron and the binding energy of the orbital from which it originated given in eq. 2.9 needs to be adjusted with an extra term depending on the screening abilities of the surrounding material.

This is known as a final state effect. These correction terms are usually not known, but they can be expected to be relatively small compared to the typical energy-level separation found in organic molecules and as such they are unlikely to change the relative ordering of the observed photoemission signals. Hence, in this work, only uncorrected binding energies obtained directly from PES measurements are reported.

2.2.1 Angle-resolved photoelectron spectroscopy

In conventional ultraviolet photoelectron spectroscopy (UPS) measurements, the intensity of photoemission is recorded either for a single take-off angle of the photoelectrons relative to the surface, or integrated over a wide range of angles. More information can be obtained by recording the angle dependence of photoemission as well as the energy dependence and this is done in angle-resolved photoelectron spectroscopy (ARPES). In particular, the distribution of momenta of the photoemitted electrons can be related to the distribution of momenta of the filled levels in the target, which can then be related to a wide range of other electronic, geometric and spin properties. The simplest and most straight-forward approximation that can be used to relate the measured distribution of photoelectrons to properties of the system being studied is the plane-wave (PW) approximation[87]. In this approximation, the outgoing electron is approximated as a plane wave, which allows us to write:

$$I \propto w \propto \left| \left\langle e^{i\vec{k}\cdot\vec{r}} \middle| \hat{\mathbf{\Delta}} \middle| \Psi_i \right\rangle \right|^2 = \left| \hat{\mathbf{A}}\hat{\mathbf{k}} \right|^2 \cdot \left| \tilde{\Psi}_i \right|^2 . \tag{2.10}$$

The result of this is that the measured distribution of momenta of the photoelectrons can be related directly to the square of the Fourier Transformed wave function $\tilde{\Psi}_i$. Although the PW approximation is commonly used to interpret angle-resolved photoemission spectra from planar, aromatic adsorbates, it is obviously based on an unphysical assumption since the outgoing photoelectrons are not well-described by plane waves. However, the same general result can be derived from the physically more sound independent atomic center (IAC) approximation[88]. In the IAC approximation, each of the atomic orbitals ξ_{nlm} contributing to a molecular orbital ψ is considered as a separate orbital contributing to photoemission. Further more, the outgoing electron is described as a spherical wave and multiple scattering is neglected. This means that the IAC approximation breaks down for molecules containing heavy atoms, although measurements on CuPc indicate that the presence of a single first-row transition metal atom does not have a significant effect[65]. The photoelectron wave function for an electron with momentum $\vec{k}$ at the detector position $\vec{R}$ which has been emitted from molecular orbital ψ then has the following form:

$$A^{\psi}\left(R,\vec{k}\right) = c_{exp} \sum_{\alpha\, n\, l\, m} C^{\psi}_{\alpha,nlm} e^{i\vec{k}\vec{R}_{\alpha}} N_{\alpha,nlm}\left(\vec{k}\right). \tag{2.11}$$

In this expression $c_{exp} = \frac{e^{ikR}}{R}$ is a prefactor that describes the damping and oscillations of the electron wave far away from the target molecule. It depends on the distance between the molecule and the analyzer, but contains no angular component. $C^{\psi}_{\alpha,nlm}$ is the contribution of atomic orbital ξ_{nlm} with principle quantum numbers n, l and m associated with atom α to the molecular orbital ψ. The factor $e^{i\vec{k}\vec{R}_{\alpha}}$ accounts for the differences in path length to the detector caused by the fact that not all atomic orbitals contributing to photoemission are localized on the same atom. Finally, the factor $N_{\alpha,nlm}\left(\vec{k}\right)$ represents the actual amplitude for optical excitation for the atomic orbital α with principle quantum numbers n, l and m. If all of the orbitals contributing to the molecular orbital are of the same type, $N_{\alpha,nlm}\left(\vec{k}\right)$ can be factored out of the sum and it becomes a prefactor N_{ξ}, yielding the following expression:

$$A^{\psi}\left(R,\vec{k}\right) = c_{exp} N_{\xi}\left(R,\vec{k}\right) \sum_{\alpha} C^{\psi}_{\alpha} e^{i\vec{k}\vec{R}_{\alpha}}. \tag{2.12}$$

This is for example the case if the orbital is a π orbital of an aromatic hydrocarbon, which purely consists of C $2p_z$ atomic orbitals. In general, N_{ξ} shows only weak angular dependence. In addition to that, it does not vary strongly with energy over the energetic width of most molecular orbitals.

For the above case, a further simplification can be made[89]. First, consider the Fourier transform of the molecular orbital from which photoemission occurs:

$$\psi = \sum_{\alpha\, n\, l\, m} C_{\alpha,nlm} \xi_{\alpha,nlm}, \tag{2.13}$$

$$\mathcal{F}(\psi) = \mathcal{F}\left(\sum_{\alpha\, n\, l\, m} C_{\alpha,nlm} \xi_{\alpha,nlm}\right), \tag{2.14}$$

$$= \mathcal{F}(\xi_{nlm}) \sum_{\alpha\, n\, l\, m} C^{\psi}_{\alpha,nlm} e^{i\vec{k}\vec{R}_{\alpha}}, \tag{2.15}$$

in which $\xi_{\alpha,nlm}$ refers to an atomic orbital centered on atom α and ξ_{nlm} refers to an atomic orbital centered on the origin of the used coordinate system. From eqs. 2.12 and 2.15 it then follows that:

$$A^{\psi}\left(R,\vec{k}\right) = \frac{c_{exp}N_{\phi}}{\mathcal{F}(\xi_{nlm})}F(\psi). \tag{2.16}$$

In the special case where ξ is a p_Z orbital, $\frac{N_{\phi}}{\mathcal{F}\left(\xi_{\alpha,nlm}\right)}$ becomes independent of emission direction if the polarization direction of the photon involved in photoemission is exactly parallel to the emission direction. However, even for experimental geometries for which this does not hold, the angular dependence of this term is weak, and thus we recover the essential result of the PW approximation. This means that, to a good approximation, the intensity is proportional to the square of the Fourier transformed molecular orbital $F(\psi)$ times a polarization function P:

$$I^{\psi} \propto \left|A^{\psi}\right|^2 \propto |P|^2 \cdot |\mathcal{F}(\psi)|^2. \tag{2.17}$$

Measurements on among others PTCDA [32,90] and Pentacene [89], which obey the restrictions outlined above, reveal that the PW approximation does indeed successfully describe the emission from the π-orbitals of planar π-conjugated molecules. Further more, ARPES measurements on CuPc [65] reveal that even in cases in which the π-orbital is made up of p_z orbitals from both carbon and nitrogen atoms, the PW approximation can still be used successfully. Since all molecules used in this work are expected to obey these restrictions as well, all angle-resolved data reported here has been interpreted using a tool that is based on the PW approximation, namely photoemission tomography.

2.2.2 Photoemission Tomography

The angular distribution of emitted photoelectrons as measured by ARPES can be used to qualitatively and quantitatively study the orbitals contributing to a certain UPS peak [32,89–93]. As eq. 2.17 shows, the angular distribution of electrons emitted from a certain orbital is proportional to the Fourier transform of that orbital. Since it is not possible to invert a squared Fourier transform, this means that one cannot directly obtain the orbital from the measured ARPES intensities. Instead, one normally starts by calculating the spatial distribution of the orbitals of a molecule using density functional theory (DFT) calculations. Although in many cases, adsorption of a molecule on a metal surface causes significant shifts in the energy of the orbitals, the spatial distribution of the orbitals of organic adsorbates are largely unperturbed and can be calculated more accurately than the energies [89]. Subsequently the Fourier transform of these orbitals can be used for fitting.

In principle, this would already yield the $|\mathcal{F}(\psi)|$ term in equation eq. 2.17. However, ARPES maps are typically measured in constant kinetic energy mode instead of constant momentum mode. This means that one slice of the measured ARPES map corresponds to a hemisphere in $|\mathcal{F}(\psi)|$, with a radius equal to $k = \sqrt{\frac{2m}{\hbar^2}E_{kin}}$. In addition to that, adsorbates on a surface may occur in a multitude of rotational domains. So, in order to generate theoretical maps that can be compared with experimentally obtained ARPES maps, one has to first take a cut through the Fourier transformed orbital at a given binding energy, rotate this cut according to the molecular orientation of each contributing molecular orbital in each equivalent domain and sum up all rotated cuts. At this point a qualitative, visual inspection can be made to compare the experimental maps with the theoretical maps, which for simple cases allows for the direct identification of UPS peaks.

If, however, a UPS peak contains contributions from multiple, chemically inequivalent molecules, one has to apply a technique known as tomographic deconvolution[91]. For each energy, a linear combination of the theoretical maps and the experimentally obtained background map is calculated according to the following formula:

$$I^T(k_x, k_y, E_b) = \sum_i a_i(E_b)\Xi_i(k_x, k_y) + b(E_b)I^M_{sub}(k_x, k_y, E_b) + c(E_b). \tag{2.18}$$

In this formula Ξ_i is a combined theoretical momentum map made by summing over the individual, rotated copies of orbital ψ_i. a_i then represents the contribution of orbital ψ_i to the ARPES intensity at binding energy E_b. I^M_{sub} is the experimentally obtained ARPES map of the background and b is the contribution of the background at binding energy E_b. Finally, c is a binding-energy dependent but momentum-independent offset.

For each value of E_b, optimal values of the parameters a, b, and c are found by fitting, which is done on a discrete, equidistant grid in (k_x, k_y, E_b)-space. On this grid, the following function is minimized:

$$\chi^2(E_b) = \sum_{k_x,k_y} w(k_x, k_y)\big(I^M(k_x, k_y, E_b) - I^T(k_x, k_y, E_b)\big)^2. \tag{2.19}$$

The weighting factor $w_k(k_x, k_y)$ is taken to be equal to the inverse of the variance at the point (k_x, k_y). Since electron intensity measurements is a form of particle counting and therefore obeys Poisson statistics, the variance is equal to the expectation value, which is also equal to the count. From this it follows that χ^2

$$\chi^2(E_b) = \sum_{k_x,k_y} \frac{\big(I^M(k_x, k_y, E_b) - I^T(k_x, k_y, E_b)\big)^2}{I^M(k_x, k_y, E_b)}. \tag{2.20}$$

The coefficients a_i are obtained by minimizing χ^2 and can then be interpreted as the projected density of states (PDOS) of orbital ψ_i at a given binding energy. In this way, it is possible to deconvolute a UPS peak containing contributions from multiple molecules into peaks associated with individual molecules.

2.3 The normal-incidence X-ray standing wave technique

The adsorption height of a molecule is a direct probe of the strength of its interaction with the surface and therefore a valuable quantity for assessing the interaction between adsorbates and the surface they reside on. In particular, by comparing the adsorption height with the adsorption height that would be expected in the case of pure Van der Waals interactions it is possible to gain information about if the molecule is physisorbed on the surface, or if there is a chemical interaction between the surface and the molecule, i.e. chemisorption. NIXSW measurements allow for the direct measurement of the adsorption height not only of molecules but also of chemically distinct atoms within these molecules. As a result it has been used extensively to study the adsorption height and structure of large organic adsorbates on the surfaces of crystals[25,45,46,50,51,62,64,66,94–101]. Although the theory of the NIXSW method will be explored more in-depth in two further chapters of this work, we will nevertheless give a short overview here on which those chapters will build forth.

NIXSW measurements rely on the creation of a standing-wave field at the surface of the crystal. When a perfect single crystal is illuminated with a wave-field with photon energies close to the Bragg condition of a Bragg reflection, a second, backreflected wave field is created. Since both wave-fields are coherent, they can interfere. The result of this is the formation of a standing wave field that extends into and out of the crystal. The following is a highly summarized review of dynamical scattering theory, for more information we refer to the appropriate chapters in Als-Nielsen 2011 [85] or Vartanyants and Zegenhagen 2013 [102].

The intensity of the standing wave field thus generated is given by the following equation:

$$I = \left| E_0 e^{-2\pi i \vec{k}_0 \vec{r}} + E_H e^{-2\pi i \vec{k}_H \vec{r}} \right|^2 = |E_0|^2 \left| 1 + \frac{E_H}{E_0} e^{-2\pi i \vec{H} \vec{r}} \right|^2 . \tag{2.21}$$

In this equation, E_0 is the complex amplitude of the incoming wave, E_h the complex amplitude of the reflected wave, $\vec{k}_0$ the wave vector of the incoming wave, $\vec{k}_H$ the wave-vector of the reflected wave and $\vec{H}$ the reciprocal lattice vector of the Bragg reflection used to generate the standing wave field. Finally, $|E_0|^2$ corresponds to the intensity of the incoming beam.

The ratio of complex amplitudes of the incoming and reflected wave-fields can be expressed in the following way:

$$\frac{E_H}{E_0} = \sqrt{R}E^{i\nu} = -\sqrt{\left(\frac{F_H}{F_{\bar{H}}}\right)}\left(\eta \pm \sqrt{\eta^2 - 1}\right). \tag{2.22}$$

Here, ν is the phase of the standing wave field, R is the reflectivity of the sample and F_H and $F_{\bar{H}}$ represent the structure factors along the reflection direction $\vec{H}$ and the direction directly opposite to $\vec{\bar{H}}$. For centrosymmetric crystals, $F_H = F_{\bar{H}}$, meaning that the reflectivity of the sample R and the phase of the standing-wave field ν depend solely on the parameter η, which parametrizes the difference between the actual photon energy and the Bragg energy. It is given by:

$$\eta = \frac{-2b\frac{\Delta E}{E_{Bragg}}\sin^2(\theta_{Bragg}) + (1-b)\Gamma F_0}{|P|\,\Gamma\sqrt{|b|F_H F_{\bar{H}}}}, \tag{2.23}$$

$$\Gamma = \frac{\frac{e^2}{4\pi\epsilon_0 mc^2}\lambda^2_{Bragg}}{\pi V_{UC}}, \tag{2.24}$$

where ΔE is the difference between the actual photon energy and the Bragg energy at a certain Bragg angle θ_{Bragg} and λ_{Bragg} is the associated wavelength. V_{UC} is the volume of the crystal unit cell and P is the polarization factor, which depends on the polarization of the incoming wave-field. Finally, b is a surface asymetry parameter that plays a role when the angle between the surface and the incoming beam is not the same as the angle between the surface and the outgoing beam. Note that F_0 and F_H are complex numbers, which means that η is a complex parameter as well.

Figure 2.2a shows the reflectivity $R = \left|\frac{E_H}{E_0}\right|^2$ as a function of η', the real part of η, which depends linearly on ΔE. If absorption is neglected, all structure factors are real and the reflectivity curve shows a typical 'Mesa' shape, becoming equal to one between $\eta' = 1$ and $\eta' = -1$. However, as shown in fig. 2.2b within this range, the phase shifts from $\nu = \pi$ to $\nu = 0$. This means that at $\eta' = 1$, the minima of the standing wave field are located at the Bragg planes, whereas for $\eta' = -1$, the maxima coincide with the Bragg planes. The effect of this is that for an absorbing solid, the absorption by atoms lying on the Bragg planes will be minimal for $\eta' = 1$ and maximal for $\eta = -1$. This then results in a clearly asymmetric shape of the reflectivity curve in the presence of adsorption of the x-rays by the crystal's atoms, as depicted in fig. 2.2

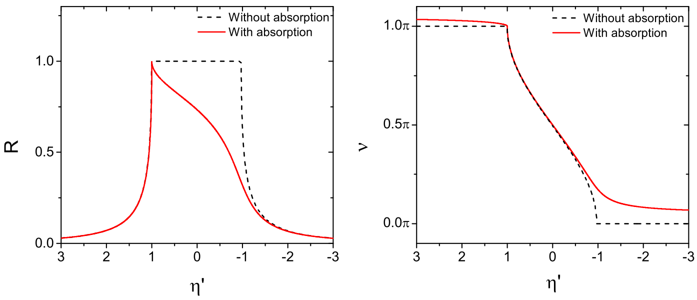

Figure 2.2: a.) plot of the reflectivity R and b.) plot of the standing wave field phase ν for a perfect single crystal as a function of the real part η' of the parameter η defined in eq. 2.23

Equations 2.21 and 2.22 can be combined to an equation that allows one to calculate the intensity of the standing wave field at position z relative to the nearest Bragg plane:

$$\frac{I_{SW}(E,z)}{I_0} = 1 + R(E) + 2\sqrt{R(E)}\cos\left(\nu(E) - 2\pi\frac{z}{d_{hkl}}\right), \tag{2.25}$$

with d_{hkl} the distance between two consecutive Bragg planes. Probing of the actual adsorption height can then be done by recording secondary emission processes that are directly proportional to the intensity of the standing wave field. Common probes include photoelectron emission, x-ray fluorescence or Auger electrons. In this work, for all NIXSW measurements, photoelectrons have been used as a probe and the relative intensity has been recorded as a function of the energy E of the impinging x-ray beam.

For a given reflectivity $R(E)$ and phase $\nu(E)$ these relative intensity profiles, also called yield curves, are unique for a given value of z. Thus, the adsorption height of a single atom or a set of atoms that all have exactly equal adsorption heights can be obtained by fitting eq. 2.25 to experimental yield curves. However surfaces are generally decorated with species adsorbed at different heights. Especially in the case of large adsorbates, bending or buckling of the adsorbates can lead to a range of different adsorptions heights for atoms that are indistinguishable using common probes. But even for atomic adsorbates, the presence of thermal and static disorder, defects, multiple adsorption sites or atoms adsorbed in overlayers can lead to a collection of different adsorption heights for indistinguishable atoms.

In order to account for the variance in adsorption heights, an emitter density function $\rho(z)$ can be introduced. Inclusion of this distribution function into eq. 2.25 then leads to the following equation:

$$\frac{I_{SW}}{I_0} = 1 + R(E) + 2\sqrt{R(E)} \int_0^{d_{hkl}} \rho(z) \cos\left(\nu(E) - 2\pi \frac{z}{d_hkl}\right) \mathrm{d}z. \quad (2.26)$$

This equation can be simplified significantly by introducing two new parameters, the coherent fraction (F^H) and the coherent position (P^H).

$$\frac{I_{SW}}{I_0} = 1 + R(E) + 2\sqrt{R(E)} F^H \cos\big(\nu(E) - 2\pi P^H\big). \quad (2.27)$$

P^H reflects the averaged adsorption height, modulo the Bragg spacing: $P^H = \frac{D^H \mod d_{hkl}}{d_{hkl}}$ with D^H the average distance above the nearest Bragg plane. This means that the adsorption height as obtained from XSW is in principle ambiguous, since a species adsorbed at a distance D^H above the surface does not yield a curve that differs from that of an equivalent species adsorbed at a height of $D^H + d_{hkl}$. For most systems this ambiguity can be resolved by requiring that the distance between the top Bragg plane and the adsorbate is physically reasonable. F^H is a measure of the degree of order of the layer. It is equal to one if and only if all atoms adsorb at exactly the same height. Any deviation from such a δ-function like shape reduces the coherent fraction, with a completely disordered layer resulting in a coherent fraction of 0, again with the caveat that all this is modulo the Bragg spacing so that 2 adsorbates separated by exactly an integer number of Bragg spacings will still show a coherent fraction of 1.

The effect of disorder and multiple adsorption sites can be understood in terms of a Fourier analysis. The coherent fraction and position can be interpreted as the amplitude and phase of one Fourier component of the Fourier transform of $f(z)$. This means that if a multitude of species is present on the surface, each with a different coherent position and coherent fraction, the average values of these parameters are equal to:

$$F^H e^{2\pi i P^H} = \sum_{k=1}^{N} n_k F_k^H e^{2\pi i P_k^H}, \quad (2.28)$$

with n_k the fraction of atoms having a coherent fraction F_k^H and coherent position P_k^H. A simple example is illustrated in the so-called Argand diagram depicted in fig. 2.3. In an Argand diagram, the coherent fraction and position of a species are indicated as vectors in polar coordinates, with the coherent fraction being the length and the coherent position being the angle. The coherent fraction and position resulting from a number of species, 2 in this example, can be calculated by scaling the vectors associated with those

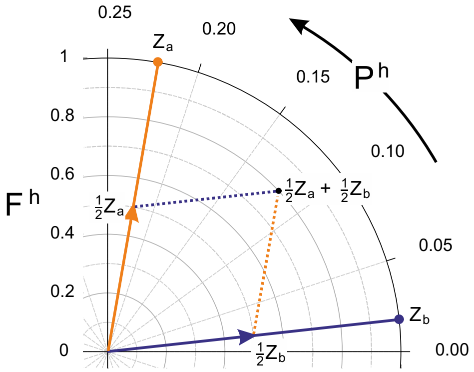

Figure 2.3: Argand diagram showing how signals from two different adsorption sites add up to give a combined coherent fraction and position. In this example, adsorption sites a and b are populated equally and they have coherent fractions and positions indicated by the Argand vectors Z_a and Z_b. The measured signal, which is a superposition of signals stemming from the two adsorption sites, then corresponds to an Argand vector equal to $^1\!/_2 Z_a + {}^1\!/_2 Z_b$.

species by their respective fractions and then summing these vectors. One peculiar result of this is that if two species are present with high coherent fractions but coherent positions that are nearly opposite in the Argand diagram, they will sum to a net vector with a very low coherent fraction. This means that although disordered layers yield a coherent fraction close to 0, a coherent fraction close to 0 does not guarantee that the layer is disordered.

2.4 Scanning Tunneling Microscopy and Spectroscopy

First demonstrated by Binnig *et al.* in 1982 [103], scanning tunneling microscopy (STM) is perhaps the most common and versatile microscopy method capable of attaining molecular-scale resolution. Its working principle is schematically depicted in figure fig. 2.4. It relies on quantum tunneling between a tip and a conductive substrate. The laws of quantum mechanics prevent electron wave-functions from ending abruptly at the edge of the sample or tip. Instead, they decay exponentially into the vacuum between the two objects. The consequence of this is that if the distance between the tip and the sample is small enough, there will be a significant overlap between the substrate and tip wave functions. In such a situation, application of a bias voltage between the sample and tip will allow electrons to tunnel through the vacuum gap, and a tunneling current is established. This tunneling current is proportional to the magnitude of the substrate wave function at the apex of the tip, and hence a measurement of the tunneling current as a function of the tip position allows one to create a map of the magnitude of the substrate wave function.

In an STM experiment, the tip is then scanned laterally over the surface and the tunneling current I is recorded as a function of the tip position (x, y). In constant-current mode, piezoelectric drives driven by a feedback loop controls the height z of the tip above the surface in order to keep I constant and the resulting map of the height as function of the lateral tip position can be interpreted as a topological map of the substrate wave-function. It is important to recognize that this is not a genuine topographic map since it combines topographic contrast with electronic contrast. In the simplest possible approximation, the Tersoff-Haman picture[104], the tip is approximated as being perfectly spherical with a curvature R and its wave-function consists only of perfectly symmetrical s-wave functions. At 0 K and extremely low sample bias U, the tunneling current can then be written as:

$$I \propto U \cdot n_t(E_F) \cdot n_s(E_F) \cdot e^{-2\kappa s}. \tag{2.29}$$

In this equation, $n_t(E_F)$ represents the tip density of states and $n_s(E_F)$ represents the density of states of the substrate, both at the Fremi edge, while s is the distance between the tip apex and the substrate and κ quantifies how rapidly the substrate wave function decays into the vacuum. We can now immediately see how it is possible to achieve molecular resolution with STM despite the fact that most tips are not atomically sharp. Since the substrate wave function decays exponentially, tunneling will only take place through the part of the tip that is closest to the substrate and the true size of the tip is unimportant as long as the tip is sufficiently sharp.

For finite bias voltages, not only the electrons right at the Fermi edge will contribute to the tunneling current, but also those coming from deeper lying levels. In this case, one has to integrate over all voltages dU in the gap between the Fermi level and U to obtain the following equation for the tunneling current:

$$I(U) \propto \int_{E_f}^{e} U n_t(E - eU) \cdot n_s(E) \cdot T(z, E, eU) \, dE.. \tag{2.30}$$

Here, $T(z, E, eU)$ is a transmission function that quantifies the probability that an electron will tunnel between the sample and the tip. For small bias voltages, the transmission function, as well as the tip density of states, are approximately constant. Hence, to a good approximation, the tunneling

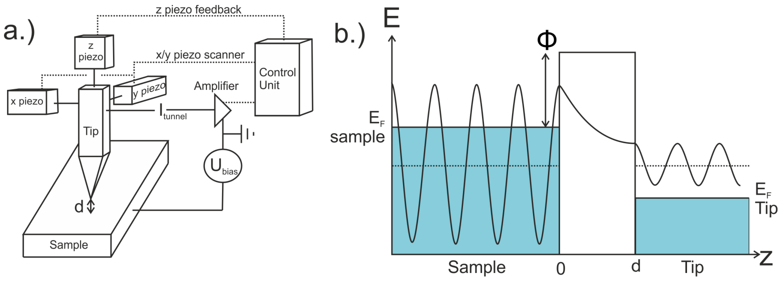

Figure 2.4: a.) Schematic representation of an STM experiment. b.) Potential diagram illustrating the wave function of an electron initially in a state in the sample below the Fermi edge of the sample impinging on the vacuum barrier with height Φ between the sample and the tip. This state decays exponentially into the vacuum barrier but it retains a significant amplitude at the apex of the tip, allowing the electron to couple to an empty state in the tip.

contrast stems from all the states in the substrate between E_F and U. From this it follows that in constant current mode, an STM measurement traces out a surface of constant integrated density of states. While scanning, the height of the tip z can change both because of the presence of a protrusion on the surface or because of a local increase in the density of states between the applied bias and the Fermi level. Therefor the contrast in a constant current image is not only of topological nature but it also contains information about the electronic structure.

More information about the local electronic structure at a point above the surface can be obtained using the Scanning Tunneling Spectroscopy (STS) technique. From eq. 2.30, the differential conductance dI/dU can be calculated. Assuming that both the transmission function and the tip density of states are independent of the applied bias, for the differential conductance we obtain:

$$\frac{dI}{dU} \propto n_t(E_F) \cdot n_s(E_F + eU) \cdot T(z, E_F + eU, eU). \tag{2.31}$$

From this equation it then follows that the differential conductance dI/dU is linearly dependent on the density of states of the substrate $n_s(E_F + eU)$ at an energy eU relative to the Fermi level. Hence, by recording the differential conductance as the applied bias is scanned, a spectrum can be obtained of the local DOS as a function of energy. In the case of organic molecules, the local DOS at a given position above a molecule will be dominated by the molecular orbitals belonging to that molecule, making STS a valuable tool for determining the exact energetic position of individual molecular orbitals and for probing the distribution of these orbitals throughout the molecule.

Chapter 3

Substrate-mediated interactions in mixed organic monolayers of PTCDA and metal phthalocyanines on Ag(111)

The data and results presented in this chapter have been published in G. van Straaten, et al., Journal of Physical Chemistry C 122 (15) (2018) 8491-8504[105]; The coauthors of this paper have supported the data collection at the Diamond synchrotron, and contributed to the discussion of the results. Some of the LEED images presented in fig. 3.1 have been acquired by B. Stadtmüller, see the corresponding caption.

3.1 Introduction

As has been highlighted in chapter 1, in many organic semiconductor devices, the interfaces between active layers and contacts have profound effects on the performance of the organic-based device. Among others, it can affect the carrier injection and extraction barriers[106–108] as well as the growth behavior of the active layer during fabrication[35,109]. In order to gain a better understanding of the interaction between metal surfaces and the organic semiconductor molecules, monolayer films of prototype organic semiconductor molecules such as aromatic anhydrides[24,25,28,32–37,40–42,90,98,110–115] and metal phthalocyanines[47,50,56,57,81,114–122] have been studied extensively. This revealed the chemical, geometric and electronic properties of many different systems, and contributed significantly to the understanding of metal-organic semiconductor contacts.

However, in many devices the active layer consists of a blend of multiple molecules[123,124]. The result of this is that at the interface, mixed phases containing multiple molecules may form. Recently it has been shown that in monolayers consisting of two organic molecules, the properties of these molecules can differ significantly from those in the homomolecular phase[61–64,66–70]. In particular, it has been found that in many of these systems, there is a significant redistribution of electron density from the donor to the acceptor molecules. Both acceptor's and donor's former lowest unoccupied molecular orbitals (fLUMOs) are initially partially filled, but formation of the mixed film fills up the acceptor's fLUMO completely while depleting that of donor. In conjunction with this charge rearrangement, an alignment of the molecular adsorptions heights has been found. Taken together, these observations indicate a significant substrate-mediated interaction between the donor and acceptor molecules in these mixed layers. Surprisingly, this interaction appears to be in contradiction to a fundamental rule in chemistry. Normally, one would expect that a filling of the acceptor's former lowest unoccupied molecular orbital (fLUMO) leads to a strengthening of the acceptor-substrate bond and thus to a shortening of the corresponding bond length while the donor-substrate bond length increases. However, measurements of the adsorption heights of the molecules in various donor-acceptor blends has revealed the opposite trend[61,62,66,70].

Attempts have been made to gain experimental insight in these substrate mediated interactions by varying the electronic character of the donor and acceptor molecules[64,68]. This is typically done by replacing either the donor or the acceptor molecules by a similar species, which unfortunately in many cases also leads to a change in the lateral structure of the layer. This often represents a problem, since variations in the lateral structure of molecular monolayers can also lead to changed adsorption sites of the adsorbed molecules, which may affect the geometric and electronic properties of the layer[43]. It is a challenge to disentangle the effects caused by changes in the geometric structure (by different shapes of the molecules) from those originating from substrate-mediated intramolecular interactions (merely caused by different electronic properties of the molecules).

In this chapter, we have attempted to overcome this challenge by taking advantage of the fact that the electronic properties of metal-phtalocyanine (MePc) molecules can be tailored by changing the central metal atom[55,117,120] *without* substantially changing the (lateral) geometric structure of these molecules. We were able to produce monolayer systems consisting of SnPc mixed with PTCDA on Ag(111), the lateral geometric structures of which are identical to the corresponding mixed layers of CuPc and PTCDA studied earlier[64]. These two systems are therefore ideal for studying the influence of the MePc's central metal atom on molecule-molecule and molecule-substrate interaction.

In the following subsections, we first compare the lateral structures of the mixed phases of PTCDA and SnPc with those of PTCDA and CuPc, elucidated from high-resolution SPA-LEED and STM measurements. Then, in the second and third section, we present measurements on the vertical adsorption structure, as obtained from normal-incidence x-ray standing wave (NIXSW), and the electronic structure, from ultraviolet photoelectron spectroscopy (UPS) and angle-resolved photoelectron spectroscopy (ARPES). The latter are analyzed using the photoemission (orbital) tomography approach, which is able to reveal the density of states (DOS) of the individual molecular orbitals, in particular of the fLUMO. We conclude with a discussion on the nature of the substrate-mediated intermolecular interactions, based on a comparison of the two heteromolecular systems. Specifically, we address how the difference in the interaction between PTCDA with CuPc or SnPc can be understood in terms of the electronic and geometric properties of these two MePc molecules.

3.2 Lateral ordering

The lateral structure and growth behavior of mixed monolayers consisting of copper-II-phtalocyanine (CuPc) and perylene-3,4,9,10-tetracarboxylicdianhydride (PTCDA) on Ag(111) has been studied extensively with SPA-LEED, STM and low energy electron microscopy (LEEM)[63,64,125]. Here, we will shortly summarize the primary findings since they act as a starting point for our analysis of the PTCDA + tin-II-phtalocyanine (SnPc)/Ag(111) system. Both systems exhibit a rich phase diagram in which at least three well-defined thermodynamically stable mixed phases can be identified. The phases formed by sequential deposition of these two molecules are determined by the deposited amounts of metal-phtalocyanine (MePc) and PTCDA. For CuPc it was found that (in thermodynamic equilibrium) at most two well-ordered phases can exist at the same time, in equilibrium with a 2D gas phase consisting mostly of CuPc. By carefully tuning the coverages of the two constituent molecules it is possible to create layers in which only one well-ordered phase is found[125].

Figure 3.1a-c shows the result of SPA-LEED measurements on the three well-ordered PTCDA + CuPc phases, in order of by their decreasing PTCDA:CuPc ratio. From left to right we show the SPA-LEED images recorded for the phases with PTCDA:MePc ratios of 2:1 (A_2B), 1:1 (AB), and 1:2 (AB_2). The behaviour of the A_2B phase (fig. 3.1a) is the simplest of these three phases. Immediately upon deposition it forms a commensurate structure with the superstructure matrix $\begin{pmatrix} 8 & -2 \\ 3 & 7 \end{pmatrix}$. The AB phase (fig. 3.1b) initially forms a metastable phase, which upon heating converts to the depicted commensurate structure, with a unit cell that can be described

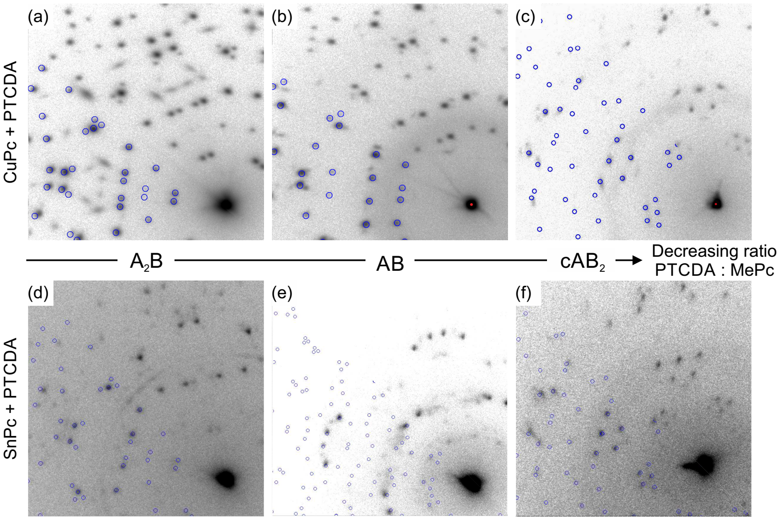

Figure 3.1: SPA-LEED images of ordered phases of PTCDA + CuPc (top) and PTCDA + SnPc (bottom), arranged from left to right with decreasing PTCDA:MePc ratio. All images were taken at an electron energy of 27 eV. Blue circles superimposed in the lower left half of the images mark the positions of the LEED spots calculated on the basis of the respective superstructure unit cell. For the CuPc + PTCDA A_2B phase some additional LEED spots are visible, stemming from excessive PTCDA molecules forming a minority phase (PTCDA HB structure). LEED images presented on the top row have been recorded by B. Stadtmüller[63].

by the superstructure matrix $\begin{pmatrix} 6 & -1 \\ 4 & 7 \end{pmatrix}$.

The structure of the AB_2 phase (fig. 3.1c) is more complex. When the CuPc coverage is close to the lower limit of the range of stability of this phase, a commensurate structure forms, with the superstructure matrix $\begin{pmatrix} 8 & 0 \\ 2 & 9 \end{pmatrix}$. We refer to this specific phase as the cAB_2 phase in the following; its LEED pattern is depicted in fig. 3.1c. However, for higher CuPc coverage, the structure changes and becomes incommensurate. The surface area per unit cell gradually decreases with increasing CuPc coverage and the smallest unit cell reported so far can be described by the superstructure matrix $\begin{pmatrix} 7.63 & 0.32 \\ 1.75 & 9.31 \end{pmatrix}$. Annealing causes desorption of CuPc molecules and allows the layer to gradually expand back towards the cAB_2 phase.

In the PTCDA + SnPc system we also find an A_2B, AB and AB_2 phase (fig. 3.1d, e and f, respectively). For two of them, namely the A_2B and the cAB_2 phases, the LEED patterns for PTCDA + CuPc and PTCDA + SnPc are identical, as can be seen from comparing fig. 3.1a with d and c with f. Thus, within the very high accuracy of the SPA-LEED method, the unit cells are identical. Since both CuPc and SnPc (laterally) have the same shape and size, it can be assumed that their arrangement in the unit cell is identical as well, so that the lateral structures of the respective structures are actually identical. This assumption is supported by the fact that the formation behavior of both phases is very similar. In both cases, the A_2B phase forms immediately upon deposition of PTCDA on a MePc-precovered surface, without the occurrence of any intermediate phase. Furthermore, these phases are unaffected by annealing.

Although the cAB_2 phases for the CuPc and SnPc systems are identical, for other structures found in this regime we find some distinct qualitative differences. As described above, the PTCDA + CuPc AB_2 phase is compressible and a variety of structures exist, depending on the precise coverage of the constituent molecules. For the PTCDA + SnPc system we found only the least dense cAB_2 structure, and one denser, incommensurate AB_2 structure (which we will refer to as the iAB_2 structure). No smooth transition exists between the two structure and hence we will in the following consider them as two separate phases. At room temperature, only the commensurate phase is formed, independent of the SnPc coverage and the excess SnPc molecules form a disordered 2D gas phase that surrounds the ordered islands. Upon heating this layer is converted into the denser iAB_2 phase. This represents a remarkable difference to the PTCDA + CuPc system, where heating leads to a relaxation of the AB_2 structure towards less dense structures due to CuPc desorption.

To gain insight into the local arrangement of the molecules in the unit cell, we have performed low temperature scanning tunneling microscopy (LT-STM) measurements on the PTCDA + SnPc iAB_2 phase which was formed by annealing of the corresponding cAB_2 phase. A comparison between the STM image shown in fig. 3.2a with the ball-and-stick model proposed for the PTCDA + CuPc cAB_2 phase (fig. 3.2b, reproduced from ref. 63) reveals a high degree of similarity. In both the STM image of the iAB_2 phase and the structural model of the cAB_2 phase, the major structural motifs are bimolecular stripes oriented approximately (but not precisely) along the $(\bar{1}01)$ direction of the substrate. However, upon closer inspection one finds a significant difference between the structural model of the cAB_2 phase and the STM images of the iAB_2 phase. In the iAB_2 phase, we find two differently oriented PTCDA species and two SnPc species. In fig. 3.2a, these orientations have been indicated for some molecules, with pink dotted lines for PTCDA and yellow dotted lines for SnPc. While the orientation of the molecules in one bimolecular stripe is always the same, the orientation of

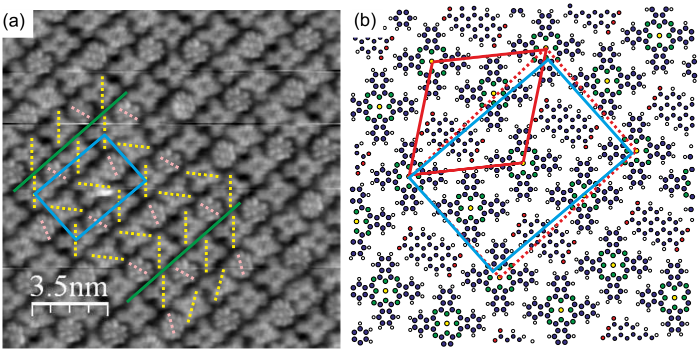

Figure 3.2: (a) STM image of the PTCDA + SnPc iAB$_2$ phase ($U_{bias} = -0.5\,\mathrm{V}$, $I = 0.05\,\mathrm{nA}$). The orientations of the SnPc and PTCDA molecules are indicated by yellow and pink dashed lines respectively. The blue lines indicate the unit cell found in this STM image and the two green lines indicate structural defects. (b) Ball-and-stick model of the cAB$_2$ phase, based on pair potential calculations (see ref 63). The reduced unit cell is indicated in red, a corresponding rectangular cell as a dashed red line. For reference, the unit cell found in (a) for the iAB$_2$ phase is shown in blue. The small mismatch between the iAB$_2$ (blue line) and the cAB$_2$ unit cell (dashed red line) is caused by a slight compression of the organic layer.

the molecules in neighboring rows typically differs. Within the accuracy of these STM measurements they are mirror images of each other. This means that the actual structure of the iAB$_2$ phase is given by the unit cell depicted in blue in fig. 3.2a and b. Comparing this unit cell with the primitive cell of the cAB$_2$ phase (solid red line in fig. 3.2b) illustrates that these unit cells are very similar. Expanding the iAB$_2$ cell to a rectangular cell (dotted red line in fig. 3.2b) almost results in the cAB$_2$ unit cell, the remaining difference is due to a small compression/expansion of the organic layer reflecting the slightly different coverages.

In addition to this well-ordered structure, in fig. 3.2a we also observe two structural defects in the otherwise well-ordered structure, formed by neighboring rows with identical orientations of molecules, which are shifted relative to each other by about half the width of an SnPc molecule. The locations of these line defects have been indicated in fig. 3.2a with green lines. On the other hand, we do not observe any defects within the rows. Furthermore, large-area STM images indicate a degree of ordering of these structural defects, but no trace of such an ordering can be found in the SPA-LEED images taken at room temperature, which instead indicate a high degree of both intra- and inter-chain order. We therefore assign the occurrence of these line defects to the formation of stress in the organic layer upon cooling, which then leads to a loss of long-range order similar to what has been observed for mixed monolayers of pentacene and F_{16}CuPC[126]. From these observations we conclude that the interaction between the molecules in neighboring rows is much weaker than the interaction between molecules within the same row. A similar situation has been observed for FePc molecules on Au(110)[127], where it was also observed that the FePc molecules form compact islands consisting of molecular rows with a high degree of intra-chain order and a lesser degree of inter-chain ordering. There, the authors showed that the weak interaction between the substrate and the molecules allowed molecule-molecule interactions to drive the formation of molecular chains and that the poor degree of inter-chain order was due to weak interactions between molecules on neighboring chains. We assume that a similar mechanism drives the formation of chains in the PTCDA + SnPc iAB_2 structure.

Finally, in both the PTCDA + CuPc and the PTCDA + SnPc system we find a phase with equal numbers of PTCDA and MePc, i.e., the AB phase (see fig. 3.1b and e). However, unlike the aforementioned phases, here significant difference between the PTCDA + CuPc and PTCDA + SnPc systems are observed. In the PTCDA + CuPc system, the unit cell of this phase contains one PTCDA and one CuPc molecule and its superstructure matrix is $\begin{pmatrix} 6 & -1 \\ 4 & 7 \end{pmatrix}$, see above. The superstructure matrix for the AB phase found for the PTCDA + SnPc system is $\begin{pmatrix} 10 & 1 \\ -3 & 9 \end{pmatrix}$. With $674\,\text{Å}^2$ this cell is more than twice as large as the PTCDA + CuPc AB unit cell ($333\,\text{Å}^2$). It is therefore most likely that this phase contains two PTCDA and two SnPc molecules per unit cell. Although both phases are commensurate with the underlying substrate, it is not possible to transform one into the other by a simple unit cell expansion. This indicates that the PTCDA + SnPc AB phase is not simply formed by a Sn-up/Sn-down superstructure as it was found for the SnPc/Ag(111) system[50]. Due to the fact that preparing samples containing only well-ordered PTCDA + SnPc AB domains turned out to be extremely challenging, no further attempt has been made at characterizing this phase.

3.3 Molecule-substrate interaction

Since both PTCDA + CuPc and PTCDA + SnPc exhibit structurally identical A_2B and cAB_2 phases, as shown in the preceding section, these two systems are ideal for studying the differences in the molecule-substrate interactions caused by replacing the central metal atom of the MePc molecules.

3.3.1 Vertical Structure

Changes in the molecule-substrate interaction can be probed using the normal-incidence x-ray standing wave (NIXSW) technique. This technique can measure the distance between the adsorbed molecules or atoms and the substrate surface with chemical resolution, i.e., separately for all chemical species that can be distinguished in PE spectra. Thus, it gives access to the effective bond length for the substrate-molecule bond, which is a geometric fingerprint of the interaction strength between the molecule and the substrate[64].

We have recorded NIXSW data sets for the A_2B and cAB_2 phases of both PTCDA + MePc heteromolecular systems. Here we present NIXSW data for PTCDA + SnPc and compare them to previously published PTCDA + CuPc results[61,62,64]. Figure 3.3 shows representative x-ray photoelectron spectroscopy (XPS) data and the fit models used for extracting the partial yield curves from the C 1s, N 1s and O 1s core level data. For the Sn 3d spectra no attempt at resolving chemically shifted components was made but the integrated peak area was used instead in the NIXSW analysis. The molecular models shown in the inset of fig. 3.4 depict all species that we have been able to analyze separately, using the same color code as for

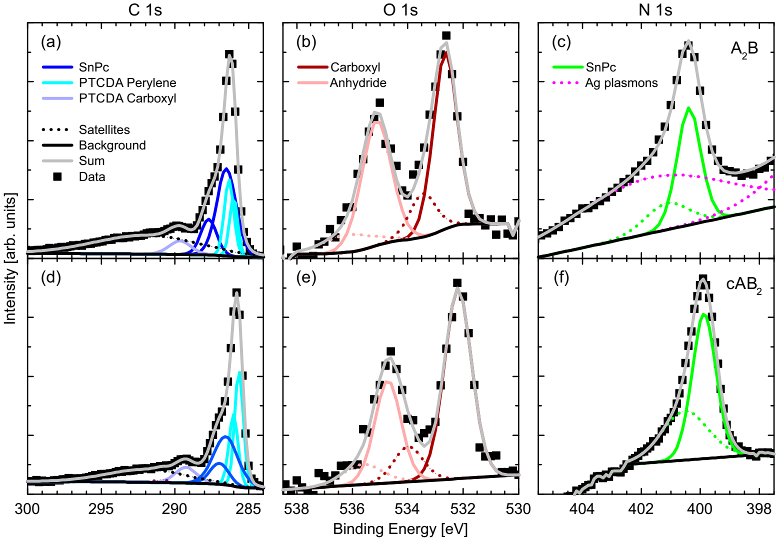

Figure 3.3: XPS data (taken 6 eV above Bragg energy) and fit models used to analyze the partial yields for all distinguishable species of the PTCDA + SnPc A_2B and cAB_2 phases. (a)-(c): A_2B phase, (d)-(f): cAB_2 phase.

Table 3.1: Coherent fractions F^H, coherent positions P^H and adsorption heights z obtained from the NIXSW analysis. Results for the A_2B phase are listed in the left part of the table, those for the cAB_2 in the right.

PTCDA	A_2B			cAB_2		
	F^H	P^H	z[Å]	F^H	P^H	z [Å]
$C_{pery.}$	1.03(2)	0.252(2)	2.95(1)	1.08(5)	0.271(7)	3.00(2)
$C_{carb.}$	0.9(1)	0.26(2)	2.97(5)	0.9(1)	0.248(8)	2.95(2)
$O_{anhy.}$	0.84(4)	0.210(6)	2.86(1)	0.9(1)	0.20(1)	2.83(2)
$O_{carb.}$	0.72(6)	0.16(1)	2.74(2)	0.86(9)	0.16(1)	2.74(2)
SnPc	A_2B			cAB_2		
	F^H	P^H	z[Å]	F^H	P^H	z [Å]
C	0.83(3)	0.27(1)	3.00(2)	0.84(8)	0.269(9)	2.99(2)
N	0.91(6)	0.235(7)	2.91(2)	0.95(5)	0.23(1)	2.90(2)
Sn	0.65(2)	0.901(5)	2.12(1)	0.68(2)	0.929(5)	2.19(1)

fig. 3.3. Figure 3.4a and b shows the result of the NIXSW analysis for the A_2B and cAB_2 phases of PTCDA + SnPc, respectively, in an Argand diagram. The results of all individual measurements are displayed as data points representing the corresponding Argand vector. The average of the measurement points for each individual species is shown as a cross, which also depicts the error bars on the average coherent fraction and position. Additionally, the averaged results of the NIXSW analysis are summarized in table 3.1.

These results are further illustrated in a structural model (fig. 3.5) comparing the adsorption heights of PTCDA + SnPc (from fig. 3.4) with results obtained for PTCDA + CuPc obtained earlier[61,62,64]. Additionally, the adsorption heights of the homomolecular adsorbate systems are depicted in gray. The first and most striking observation is that in both heteromolecular phases, compared to the homomolecular phase, the entire SnPc molecule moves closer to the Ag surface by as much as 0.2 Å, and the central Sn atom even by 0.3 Å. The adsorption height of the MePc backbone after mixing with PTCDA is approximately the same for both CuPc and SnPc, in spite of the much larger Sn atom being present in the latter molecule. The PTCDA molecular core, however, moves away from the Ag surface by approximately 0.1 Å in both heteromolecular phases, similar to what was observed in the PTCDA + CuPc system. Hence, as observed before for the PTCDA + CuPc heteromolecular phases, there is an alignment of the adsorption heights of the donor and acceptor molecules.

In addition to the distinct adjustments of the adsorption heights of the molecular backbones of both molecules upon forming heteromolecular structures, there is also a significant change in the PTCDA intramolecular

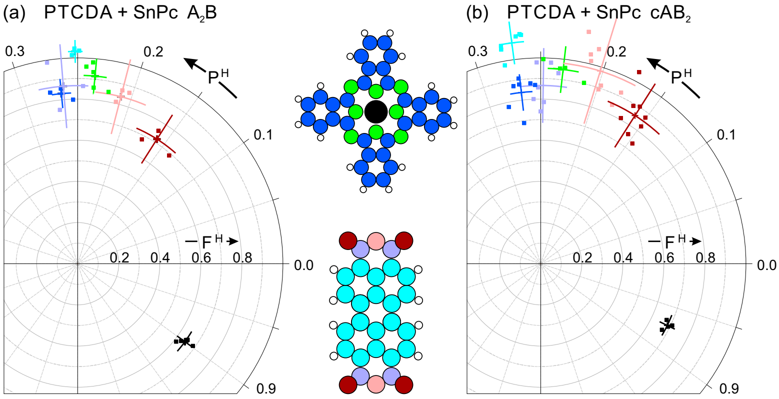

Figure 3.4: Argand diagrams illustrating the fitting results for all individual NIXSW scans for (a) the A_2B and (b) the cAB_2 phase. Squares indicate individual data points while the crosses indicate the average coherent position P^H and coherent fraction F^H, as well as the estimated error bars. Colors of the data points correspond to the atomic species indicated in the two atomic models.

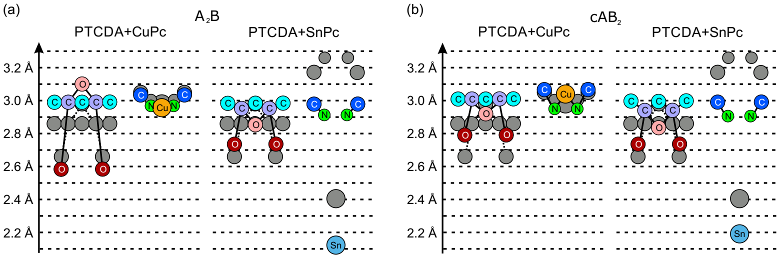

Figure 3.5: Illustration of adsorption heights for (a) the A_2B and (b) the cAB_2 phases of SnPc + PTCDA (right panels) and CuPc + PTCDA (left panels). Colored circles indicate the adsorption heights for the heteromolecular layers, gray circles those of the corresponding homomolecular phases, that are the PTCDA/Ag(111) HB phase and the monolayer phases of CuPc and SnPc/Ag(111).

structure. In the homomolecular phase, PTCDA adopts a saddle-like configuration, with the anhydride oxygen sticking out above the molecular plane and the carboxyl oxygens lying below it. In the PTCDA + CuPc A_2B phase, this general shape is retained. However, in the PTCDA + CuPc AB_2 phase, as well as in both PTCDA + SnPc heteromolecular phases, the PTCDA anhydride oxygen atoms lie below the molecular plane and the anhydride group adopts an M-like shape. Such a saddle-like vs. M-like distortion of the PTCDA molecule has been reported earlier for PTCDA adsorbed on Ag(100) and Ag(110)[98].

3.3.2 Charge transfer

Up to now we have discussed the geometric fingerprint of the substrate-molecule interaction strength. Now we switch to its electronic fingerprint, the charge transfer between molecules and surfaces, which also reflects the strength of molecule-substrate bonding. It has been shown that photoemission peaks can shift significantly in energy upon the formation of mixed layers, owing to molecular orbitals hybridizing with substrate electronic states[62,64,67–69]. In the specific case of PTCDA + CuPc this leads to changes in the charge transfer between the molecules and the surface. In their respective homomolecular phases both PTCDA and CuPc have a partially filled fLUMO. In their heteromolecular structures, however, the PTCDA fLUMO is found to be completely filled while the CuPc fLUMO is depopulated.

In fig. 3.6 we compare UPS data for the PTCDA + CuPc and the PTCDA + SnPc systems. Clear differences can be seen in the energetic positions of the peak closest to the Fermi level. We have shown previously that in the PTCDA + CuPc systems this peak is purely due to the PTCDA fLUMO and that no contribution stemming from any CuPc state can be indentified in this region[62,64]. The question arises whether or not this holds for the PTCDA + SnPc systems as well. In order to answer this question we employed the photoemission tomography technique[32,89–91].

Beside the ARPES data on heteromolecular films we measured two reference systems: The clean Ag(111) surface (see fig. 3.8d and discussion below), and a SnPc monolayer film on Ag(111). For the latter, fig. 3.7a shows a symmetrized constant binding energy (CBE) map generated for a binding energy of 0.2 eV (corresponding to the maximum of the spectral intensity of the fLUMO peak). Figure 3.7b displays the corresponding calculated map for the SnPc fLUMO, under consideration of the molecular orientation and domain formation for the SnPc monolayer structure on Ag(111). In this simple case, a comparison of these measured and calculated CBE maps allows us to directly distinguish between molecule and substrate related features.

We now turn to a discussion of the CBE maps recorded for the heteromolecular PTCDA + SnPc A_2B and cAB_2 phases, for which a simple comparison of measurement and calculation is not sufficient, but a full deconvolution is required to disentangle all contributions to the spectral intensity. The relevant molecular contributions to the measured CBE map (fig. 3.8a) stem from the PTCDA and SnPc fLUMOs. For the A_2B phase, the corresponding theoretical maps are depicted in fig. 3.8b and c, respectively. The maps are calculated under consideration of the correct orientation of the molecules within the A_2B unit cell, and the occurrence of six rotational

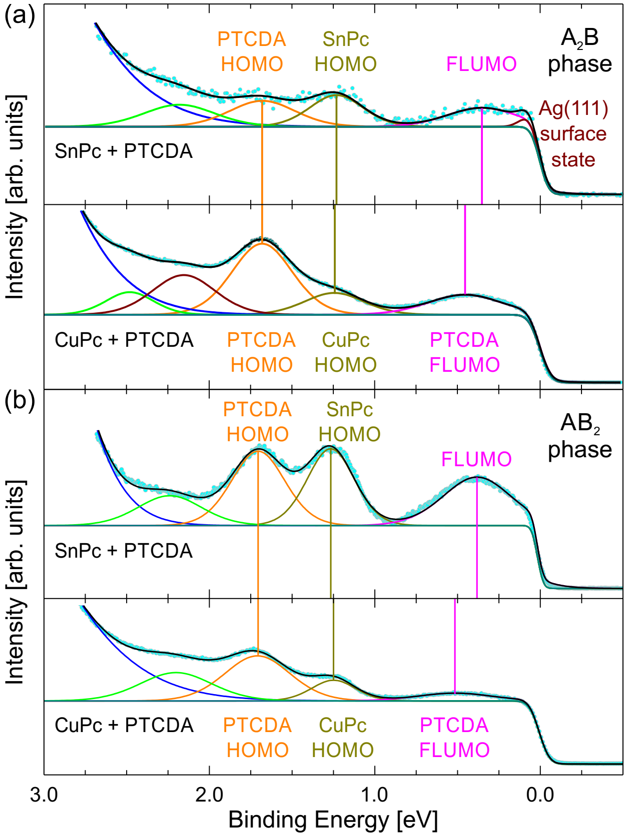

Figure 3.6: Comparison of UP spectra for PTCDA + CuPc and PTCDA + SnPc for (a) the A_2B and (b) the cAB_2 phase. Measured data points and best fits of the contributions from the relevant orbitals are shown. The peak assignment is based on the photoemission tomography analysis of the PTCDA + CuPc A_2B phase reported in[64]. Note that in the case of the PTCDA + SnPc A_2B phase, the spectrum was measured on a surface with a total adsorbate coverage below 1 ML and thus there is some residual intensity visible stemming from an Ag(111) surface state present on the uncovered parts of the surface.

and mirror domains caused by the p3m1-symmetry of the Ag(111) surface. Furthermore, we had to consider the contributions from the Ag surface. For the latter, as in earlier investigations[62,64], we included a measured CBE map of a clean Ag(111) surface (see fig. 3.8d). However, a careful fitting of the

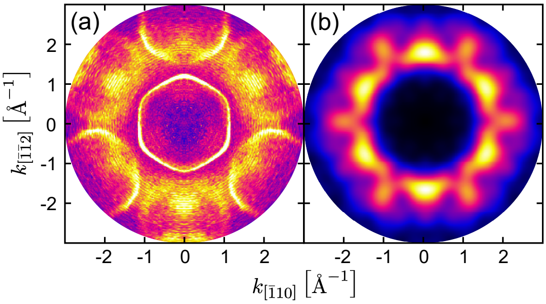

Figure 3.7: (a) CBE map of a SnPc monolayer film on Ag(111), recorded at a binding energy of 0.2 eV, which corresponds to the maximum of the fLUMO peak. (b) Calculated CBE map for the fLUMO of the same SnPc structure. The in-plane orientation of the molecules was considered as well as the formation of six equivalent domains due to the substrate symmetry.

experimental data (fig. 3.8a) with all of the mentioned contributions (fig. 3.8b, c, d and f) did not yield completely satisfying results, but revealed that the intensity of a 3-fold symmetric lobe-like structure was underestimated by the fit (in fig. 3.8a one of these maxima is marked with a white circle and labeled “A”). Due to its three-fold symmetry this feature cannot stem from the molecular film but must originate from the Ag substrate. In addition to that, it is not visible in the maps recorded for the clean surface (fig. 3.8d), but the experimental maps for SnPc homomolecular phase (see fig. 3.7a) exhibits very similar features. We therefore assign feature A to a state belonging to the substrate that becomes partially filled upon the interaction between the substrate and the adsorbed molecules, and we will refer to this state as “state A” in the following. We used the CBE map depicted in fig. 3.8e, which is based on the experimental map of the SnPc/Ag(111) system (fig. 3.7a), for considering this (relatively small) effect.

In ref. 62 it was noted that not all PTCDA molecules are incorporated into the PTCDA + CuPc systems, but some of them form parasitic islands of the homomolecular herringbone (HB) structure. We expect the same to be true for the PTCDA molecules in the PTCDA + SnPc A_2B phase, although we were unable to resolve this parasitic structure in LEED measurements. Therefore we also include a theoretical CBE map corresponding to PTCDA fLUMO’s in the HB structure in our analysis (see fig. 3.8f)

The result of the photoemission tomography fitting to the fLUMO region of the PTCDA + SnPc A_2B phase is depicted in fig. 3.9a. The data represents the PDOS of all relevant contributions to the experimental data. We find that, as expected, the dominant contributions to the density of states stem from PTCDA molecules in the A_2B phase, and also from the SnPc 2D gas-

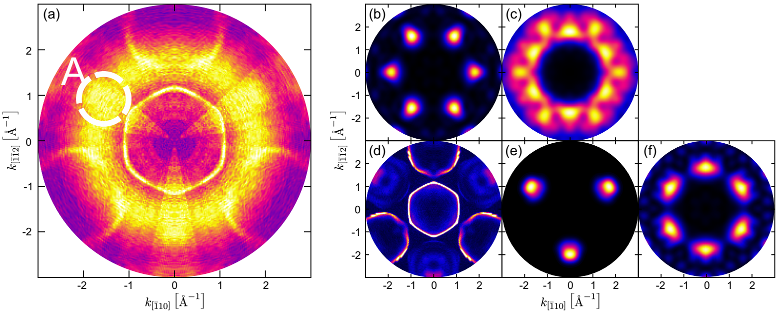

Figure 3.8: (a) CBE map of the PTCDA + SnPc A_2B phase, recorded at a binding energy of 0.4 eV. (b) and (c) Calculated CBE maps for the fLUMO of PTCDA and SnPc molecules, under consideration of the orientations of these molecules in the A_2B phase and of all symmetry equivalent domains. (d) CBE map of the bare Ag(111) surface, recorded at a binding energy of 0.4 eV. (e) CBE map for state A, for details see text. (f) Calculated CBE map for the fLUMO of PTCDA in the (homomolecular) herringbone structure (under consideration of all molecular orientations). This phase was found as minority phase on some parts of the sample surface.

phase molecules. Note that the binding energy of the PTCDA fLUMO in the A_2B phase is significantly higher (the peak maximum is observed at 0.4 eV) than for the homomolecular PTCDA contribution (0.2 - 0.3 eV[24,62]). This value is very close to that found for the PTCDA + CuPc A_2B phase (0.44 eV). However, in contrast to the PTCDA + CuPc system, we also observe a small but significant intensity from the SnPc fLUMO in the A_2B phase, located very close to the Fermi level. We can conclude that, compared to homomolecular SnPc/Ag(111), the SnPc fLUMO has been shifted towards the Fermi level, indicating that some charge transfer from SnPc (via the substrate) to PTCDA has taken place, but in contrast to the PTCDA + CuPc system the depopulation of the SnPc fLUMO is not complete.

For the cAB_2 phase, we performed the same analysis. Both experimental and theoretical CBE maps for the SnPc and PTCDA molecules in this heteromolecular phase turned out to be very similar to the ones of the A_2B phase discussed above. The only substantial difference in our analysis is that we did not consider any contribution of a PTCDA HB structure. Instead, based on the stoichiometry of this heteromolecular phase and the deposited amount of both molecular species, we considered the existence of parasitic SnPc molecules in a 2D gas phase in the area around the heteromolecular islands. From LEED measurements it is known that at room temperature these gas-phase SnPc molecules show no rotational order, since all intramolecular scattering features are completely isotropic[50]. As such the

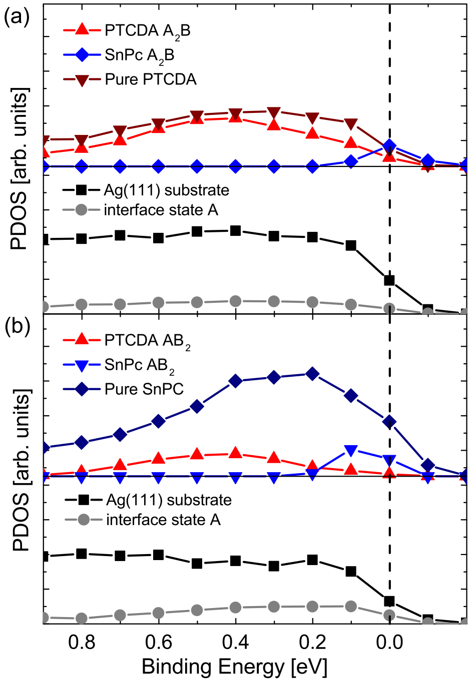

Figure 3.9: PDOS obtained by the photoemission tomography technique for (a) the A_2B and (b) the AB_2 phase of the PTCDA + SnPc system. Contributions of homomolecular phases (PTCDA herringbone in (a), SnPc 2D gas-phase in (b)) were considered, as well as contributions from the Ag(111) substrate and the state A.

corresponding CBE map consists only ring-like features. The PDOS of each contribution obtained from this analysis are depicted in fig. 3.9b. As for the A_2B phase, we observe an incomplete charge transfer from the SnPc fLUMO to the PTCDA fLUMO, resulting in a downshifted PTCDA fLUMO and a SnPc fLUMO that is pinned to the Fermi level.

The observation of a non-zero molecular density of states at the Fermi level is confirmed by comparing radial intensity profiles from CBE maps recorded for 0.0 eV and 0.4 eV, i.e., directly at the Fermi level and at the maximum of the fLUMO peak. The corresponding maps for the A_2B phase are shown in fig. 3.10a and fig. 3.8a, respectively, the radial intensity profiles in fig. 3.10b. Additionally, the corresponding profiles extracted from the relevant theoretical CBE maps (that are the maps displayed in fig. 3.8b, c and f) are shown. Note that the direction of the linescans (that is the $(\bar{1}01)$

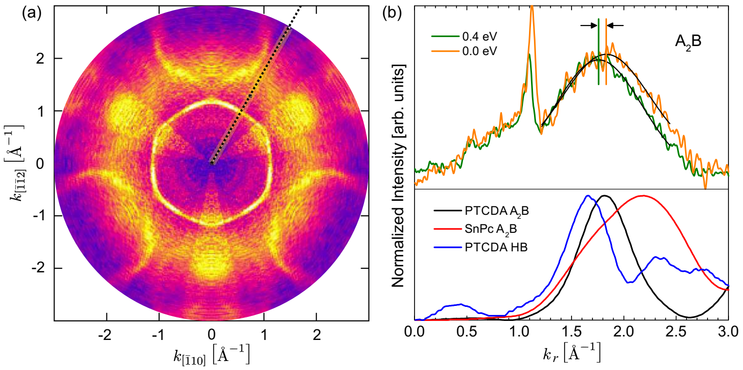

Figure 3.10: (a) CBE map of the PTCDA + SnPc A_2B phase, recorded at the Fermi energy (zero binding energy). The black line indicates the direction for extracting the radial intensity profiles shown in b. (b) Normalized radial intensity profiles extracted from the experimental PTCDA + SnPc A_2B maps at zero binding energy (panel a) and at 0.4 eV (fig. 3.8a), and from the relevant theoretical maps (fig. 3.8b, c and f). The experimental profiles are normalized to their values at $k_r = 1.7\,\text{Å}^{-1}$, that is the radial momentum at which the theoretical map for PTCDA in the mixed phases shows a maximum.

direction of the substrate lattice) is marked by a black line in fig. 3.10a. The theoretical profiles displayed in fig. 3.10b indicate that the relevant region for judging the filling of the SnPc fLUMO in the heteromolecular phases is the region $k_r > 2.0\,\text{Å}$, since this orbital is clearly the strongest in this high-momentum region. The experimental profile extracted from the map recorded at the Fermi energy (binding energy of 0.0 eV) shows an increased intensity in this $k_r > 2.0\text{Å}$ regime compared to the profile from the 0.4 eV map, as indicated by the Gaussian fit profiles. Hence, this analysis supports the conclusion that the fLUMO of SnPc molecules within the heteromolecular phases are not completely depleted.

Further evidence for a non-zero DOS at the Fermi energy can be found in scanning tunneling spectroscopy (STS) measurements on the PTCDA + SnPc iAB_2 phase, as can be seen in fig. 3.11. The spectrum measured on the PTCDA molecule displays a strong resonance centered at a bias of 0.4 eV, matching the maximum found for the PTCDA fLUMO in fig. 3.9. Likewise, for the spectra measured on SnPc molecules, we observe a peak around the Fermi energy that can be assigned to the partially filled SnPc fLUMO. Finally we note that there is a weak resonance visible at the Fermi energy in the spectrum taken on the PTCDA molecule. We suspect that this signal could be caused by SnPc fLUMO charge density extending towards

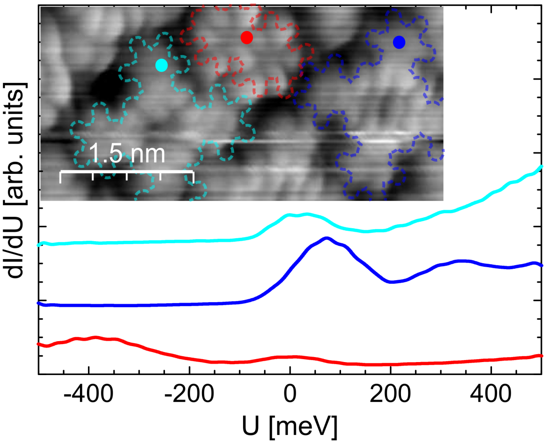

Figure 3.11: Scanning tunneling dI/dV spectra ($\nu \approx 780\,\mathrm{Hz}$, $5\,\mathrm{mV}$) recorded with a modified tip and at different positions in the unit cell of the PTCDA + SnPc iAB_2 phase. The data is low-pass filtered. Colored dots in the STM image shown as inset indicates the locations where the spectra were recorded. As a reference we have added approximate outlines of the SnPc (blue, cyan) and PTCDA (red) molecules on which the spectra have been measured

the tip even when it is situated over the PTCDA molecule.

3.4 The nature of substrate-mediated intermolecular interactions

So far, we have identified several similarities and differences between the PTCDA + SnPc and PTCDA + CuPc/Ag(111): Similarities are (i) that both systems exhibit two commensurate phases (A_2B and cAB_2) the unit cells of which do not depend on the type of MePc molecule used (i.e., SnPc and CuPc containing structures are laterally identical). (ii) In all phases we observe an increase in the adsorption heights of the PTCDA perylene core, as compared to the homomolecular system. (iii) Regarding the electronic structure, we observe significant charge reorganizations in all systems upon formation of the heteromolecular layer, in particular regarding the occupation of the fLUMO levels of both types of molecules.

The most significantly differences are: (i) The PTCDA molecule is bent due to the interaction of the oxygen atoms with the substrate, which for the PTCDA + CuPc A_2B phase results in a saddle-like shape (anhydride oxygen above the perylene plane), for all other phases in an M-like shape (anhydride oxygen below the perylene plane). The change in the adsorption height also differs for the two MePc structures. It is only slightly reduced for CuPc ($<$ 0.05 Å), but significantly for SnPc (approx. 0.2 Å). (ii) Electronically, the most relevant difference is that in CuPc the fLUMO is completely depopulated in all heteromolecular phases, whereas in SnPc fLUMO remains partially occupied.

We propose that these differences between CuPc- and SnPc-containing structures originate from by the different (vertical) geometric structures of the Pc molecules. While the central metal atom of CuPc is embedded in the central cavity of the Pc molecule, resulting in a planar molecule, the Sn atom of SnPc protrudes from the molecular plane, forcing the molecule in a distorted, "inverted umbrella-like" shape. Before discussing the consequences for the interaction between PTCDA and MePc molecules, we shortly summarize the charge transfer mechanisms found for the PTCDA + CuPc system: Previously we have explained the observation of charge rearrangement from CuPc to PTCDA and the alignment of the adsorption height of the molecules by a substrate mediated charge transfer effect [62,64].

Generally speaking, the interaction between a molecule and a metal surface involves both charge donation from the surface to the molecule (as well as backdonation from the molecule into the surface) and Pauli repulsion between the electrons of the substrate and the adsorbate. DFT calculations show that in the case of the adsorption of CuPc molecules on Ag(111) the charge donation effect results in accumulation of charge in the molecule's π-system, and that some back-donation of charge into the substrate takes place via the central metal atom. Furthermore, Pauli repulsion causes a lateral displacement of the substrate charge density underneath the CuPc molecules [52,64]. Taken together, this leads to a net charge transfer from the substrate into the molecules (dominantly into the π-system), and towards regions underneath the periphery of the molecules and in between neighboring molecules.

On the other hand, when a single, isolated PTCDA molecule is adsorbed on Ag(111), donation of charge from the substrate into the molecule prevails over the Pauli pushback, leading to an even bigger net transfer of charge from the substrate to the molecule. Most of this charge is accepted by the PTCDA fLUMO but some of it is backdonated via the anhydride groups. The net result is a depletion of charge in the region between the molecules as well as around the anhydride groups, and an accumulation of charge underneath the perylene core [128].

DFT calculations on the PTCDA + CuPc A_2B phase show that in this heteromolecular system, these reorganization processes interact in a synergistic way. Significant parts of the substrate electron density are redistributed from the CuPc adsorption sites to the PTCDA adsorption sites, strengthening the PTCDA-substrate interaction and pushing the PTCDA molecule upwards while the interaction between CuPc and the substrate is weakened[62].

If we now compare these scenarios with the charge density rearrangement found when SnPc is adsorbed on Ag(111) with the central metal atom pointing towards the surface (i.e. the configuration found in all mixed phases presented here), we see a similar effect as observed for CuPc[51,53]. Again, there is a considerable redistribution of the substrate electron density toward the regions between the molecules, as well as a partially filling of the fLUMO and an accumulation of charge underneath the central metal atom[50]. However, there is a qualitative difference between SnPc and CuPc. Despite its larger van der Waals radius, the central metal atom of SnPc is found much closer to the surface than that of CuPc, indicating a stronger interaction between Sn and the surface compared to Cu. From this starting point we now discuss the origin of the differences observed between the PTCDA + SnPc and the PTCDA + CuPc systems.

The most obvious difference is that in the heteromolecular PTCDA + SnPc system the adsorption height of the SnPc molecule differs significantly from that in the homomolecular phase, in contrast to PTCDA + CuPc, where only a marginal difference has been found. We propose that this is the result of a stronger interaction of the SnPc central metal atom with the substrate. In the homomolecular SnPc phase, there is a significant Pauli repulsion between the central metal atom and the substrate, which causes a redistribution of substrate electron density away from the central metal atom. This then leads to an enhancement of the substrate electron density just beyond the edges of the SnPc molecule. If the neighboring molecule is also a SnPc molecule, this effect contributes to the intermolecular repulsion that has been reported for this kind of molecules in homomolecular phases (see, e.g., ref. 50). However, when SnPc is mixed with PTCDA, the enhanced electron density is instead driven into the regions underneath neighboring PTCDA molecules that take up most of the extra electron density. As a result, the local electron density underneath the SnPc molecules is reduced, leading to a reduced Pauli repulsion and allowing the phthalocyanine ligand to come closer to the Ag surface. This also pushes the Sn atom towards the Ag surface, explaining the smaller adsorption heights observed experimentally. In contrast, for the CuPc molecules this does occur since their adsorption height is limited by the distance between the aromatic core of the molecule and the substrate, not by the distance of the central metal atom to the substrate. This conclusion is also supported by the observation that the Sn atom is closest to the surface in the PTCDA-rich A_2B phase, since here we have one MePc molecule per two PTCDA molecules and thus the depletion of electron density at the MePc adsorption sites is stronger than in the AB_2 phase, where there are two MePcs per PTCDA molecule. In the latter phase, the charge donated by the two MePc molecules cannot be completely accepted by the PTCDA molecules, and hence the Pauli repulsion between the molecule and the substrate remains stronger and the adsorption heights larger than in the A_2B phase.

Note that this charge rearrangement is compatible with the differences in the fLUMO positions of SnPc and CuPc after mixing with PTCDA. Upon mixing MePc with PTCDA, and provided that the energetic alignment of the fLUMOs of both species allows it, the PTCDA molecule takes up the excess electron density generated by the pushback effect and thus these electrons are no longer available for donation into the CuPc fLUMO. In the case of SnPc, the enhanced Pauli pushback means that there are more substrate electrons available for donation. This can be seen as if after the PTCDA fLUMO and anhydride groups have accepted as much charge as they can, there are still electrons available for donation into the SnPc fLUMO, leading to a partially filled fLUMO that is pinned to the Fermi level.

A second important finding from the NIXSW experiments was the different bending of the PTCDA molecule in the individual phases. Only in the PTCDA + CuPc A_2B phase, the PTCDA anhydride groups are found in a saddle-like configuration, with the anhydride oxygen sticking out above the plane of the perylene. In all other phases (PTCDA + CuPc AB_2 and both PTCDA + SnPc phases), the PTCDA anhydride groups are found in an M-like configuration, with the anhydride oxygen below the perylene plane. In an earlier work[61], this was attributed to the fact that the PTCDA + CuPc A_2B phase is commensurate while the AB_2 phase is incommensurate. But since both PTCDA + SnPc phases are commensurate, this explanation must be revisited.

It was also discussed in an earlier work[98] that PTCDA adopts a saddle-like shape in homomolecular layers on Ag(111), but not on Ag(110) and Ag(100), where it instead adsorbs in an M-like configuration. Apparently, Ag(111) is not reactive enough to form a localized bond with the less reactive anhydride oxygens, and local bonding takes place only through the more reactive carboxyl oxygens. However, Ag(110) and Ag(100) are reactive enough to form localized bonds with all the oxygen species in the PTCDA molecules. As noted above, the central metal atom of SnPc interacts more strongly with the substrate than the central metal atom of CuPc, which leads to a stronger Pauli pushback effect. The result of this is a higher surface electron density in the vicinity of the PTCDA molecule, and consequently a locally increased reactivity of the surface. This enables a stronger rehybridization of PTCDA with the substrate. Similarly, when comparing the PTCDA + CuPc A_2B phase to the AB_2 phase, the increased CuPc to PTCDA ratio of the AB_2 phase implies that the extra electron density available per PTCDA molecule goes up, making the surface locally more reactive and explaining the switch from the anhydride-up to the anhydride-down configuration.

3.5 Summary

Taking advantage of the fact that two of the heteromolecular phases of PTCDA + SnPc/Ag(111) and PTCDA + CuPc/Ag(111) have identical lateral structures, we have analyzed the influence of the MePc central metal atom on the properties of these mixed layers. In particular, we have shown that the fact that the Sn central metal atom of SnPc displays a stronger pushback effect than the Cu atom of CuPc leads to three significant differences: Firstly, the adsorption height of SnPc is much more strongly affected by forming mixed structures with PTCDA than that of CuPc: While the CuPc adsorption height hardly changes, that of SnPc reduces by approximately 0.2 Å with respect to its homomolecular monolayer phase. Secondly, while in both systems the PTCDA fLUMO becomes almost completely filled upon mixing, in the PTCDA + CuPc mixed system the CuPc fLUMO is completely depleted of charge, whereas in the PTCDA + SnPc system the SnPc fLUMO remains partially filled. And thirdly, we have shown that the vertical structure of the PTCDA anhydride group is sensitive to both the PTCDA:MePc ratio and to the chemical nature of the MePc molecules. In the PTCDA + CuPc A_2B phase it adopts a saddle-like configuration, whereas in the AB_2 phase it adopts an M-like configuration, as it does in all PTCDA + SnPc phases.

We have shown that these differences can be explained in context with the substrate mediated charge transfer model. Upon mixing PTCDA with MePc molecules, substrate electron density is transferred from the MePc adsorption sites to the PTCDA adsorption sites. In the case of PTCDA + CuPc this leads to the depletion of the CuPc fLUMO and the filling of the PTCDA fLUMO. In the cAB_2 phase, the formation of local bonds between the substrate and the PTCDA anhydride oxygens occurs additionally. A second effect was found for the case of PTCDA + SnPc: The SnPc adsorption height is primarily determined by the interaction between the Sn central metal atom and the substrate, not by the aromatic molecular core and the surface (as it is the case for CuPc). As charge is transferred away from the SnPc adsorption sites, the pushback effect between the Sn central atom and the surface is reduced, allowing the Sn atom to come closer to the substrate, which in turn reduces the adsorption height of the entire molecule. The charge depleted from the position underneath the central atom is partly back-donated into the SnPc fLUMO (which in turn becomes partially filled), and partly contributes to the bond formation between the substrate and the PTCDA anhydride oxygens, as observed in the case of the A_2B phase.

In conclusion, the model of substrate mediated charge transfer, as proposed for the PTCDA + CuPc systems in refs. 62 and 64, is fully confirmed and can comprehensively explain all effects observed for the PTCDA + SnPc systems as well. We propose that this model is of general validity for the formation of comparable acceptor-donor blends.

3.6 Sample preparation

All measurements were performed under UHV conditions with a base pressure below 5×10^{-10} mbar. Clean Ag(111) surfaces were prepared by sputtering the surface with 500 eV Ar^+ ions under 45° and −45° off-normal incidence for at least 15 minutes each, followed by annealing at temperatures above 750 K for at least 20 minutes. This procedure was repeated until the surface was of sufficient quality and cleanliness. Surfaces prepared for use in SPA-LEED experiments were checked by measuring the mean terrace size, as obtained from a peak width analysis in SPA-LEED, those for NIXSW and ARPES were checked by XPS for contaminations.

Subsequently, organic molecules were deposited by organic molecular beam epitaxy from dedicated, home-built Knudsen cell evaporators. Deposition rates were monitored by recording the ion current signal of typical fragments of the evaporated molecules using a mass spectrometer. The absolute deposition rate was calibrated against the mass spectrometer signals recorded for well-known homomolecular phases.

In all experiments, first a desired amount of SnPc was deposited, forming a disordered 2D gas phase. Subsequently, PTCDA was deposited while the formation of mixed phases was monitored using a LEED or SPA-LEED. The formation of a mixed phase was deemed complete when sharp and intense spots were visible belonging to the mixed phase, and no more ring-like scattering intensity associated with the SnPc gas-phase was visible. Typical deposition rates were 0.05 to 0.1 ML/min, and when monitoring the deposition using SPA-LEED, diffraction patterns were recorded at a rate of one image per minute. All experiments were performed at room temperature.

Chapter 4

Non-dipolar effects in photoelectron-based normal incidence x-ray standing wave experiments

The data and results presented in this chapter have been published in G. van Straaten, et al., Journal of Electron Spectroscopy and Related Phenomena 222 (2018) 106-116[129]; The coauthors of this paper have supported the data collection at the Diamond synchrotron and contributed to the discussion of the results. The mathematical derivations presented in this chapter were verified independently and implemented in the software package Torricelli[130] by M. Franke and F. C. Bocquet. Finally, some of the data presented in fig. 4.5 were measured by F. Bocquet, see the corresponding caption for details.

4.1 Introduction

As the previous chapter has shown, valuable information about molecule-substrate and molecule-molecule interactions in adsorbate monolayers can be obtained from measurements of the distance between the substrate and (parts of) the molecule. There are very few established experimental techniques that are able to yield vertical atomic structure with sub-Ångström resolution. The most prominent ones are quantitative low energy electron diffraction (LEED-IV)[73–75], surface x-ray diffraction (SXRD)[131–137], photoelectron diffraction (PhD)[59,138–140], and (normal incidence) x-ray standing waves ((NI)XSW)[27,47,61,102,141–148]. The first (LEED-IV) is able to deliver the full three-dimensional structure of well ordered systems, but it is mathematically relatively expensive since the full dynamical diffraction theory has to be employed, limiting it to systems with relatively small unit cells. The second, SXRD, has similar capabilities at lower costs (kinematic diffraction theory is sufficient), but cannot be applied to systems containing light elements only due to low scattering cross sections. Furthermore, both are indirect methods which – owing to the phase problem of basically all scattering techniques – rely on the refinement of a structural model. The third, PhD, can give insight in bonding distances between specific atoms and therefore contribute very valuable information to a structure determination. The information is inherently local to the probed atomic species, but sometimes the resulting spectra are difficult to interpret, since multiple non-equivalent species may contribute to the same spectrum. The fourth, XSW, is possibly the most precise and generally applicable technique of the four. It was originally developed in order to solve the phase problem in x-ray diffraction measurements and to measure the position of both native atoms[149] and dopants[150–152] within perfect crystals, and it is still commonly applied for this purpose[153,154]. However, soon after its initial development, it was realized that the standing wave field used in an XSW experiment also extents outside of the generating crystal, allowing it to be applied to the study of surfaces and adsorbate layers as well[155,156] and it is this property of the XSW measurement that was employed in the previous chapter to gain information about the bonding between CuPc, SnPc, PTCDA and the Ag(111) surface and how lateral interactions affect this bond.

The primary property that make the XSW technique so versatile are that it is (just like PhD) chemically sensitive, since characteristic photoelectron or fluorescence emission lines are used. In practice, even contributions of the same atomic species in different chemical environments can be distinguished, a feature that became more and more powerful owing to the improving energy resolution offered by modern electron analyzers and high-resolution synchrotron beamlines. Furthermore, each XSW measurement provides two structural parameters for the studied species relative to a set of Bragg planes h, namely the coherent fraction and position. These can be understood as the amplitude and phase of the h-th Fourier expansion coefficient of the spatial distribution of the considered atomic species. Hence, this method does not suffer from the phase problem that plagues diffraction techniques like LEED-IV or SXRD. This means that for adsorbate systems commensurate with the substrate, if XSW measurements can be performed for a sufficient number of different Bragg diffraction, it is not only possible to obtain the exact adsorption site of a species by triangulation[94,144,145], but even to obtain a full 3-dimensional reconstruction of all atomic positions in terms of the Fourier expansion of the atomic distributions (so-called XSW-imaging)[154,157–160]. Furthermore, XSW is generally applicable to systems exhibiting vertical order only, while lateral order is not required. This implies, that adsorbate systems with (very) large unit cells or with incommensurate registry to the substrate can be investigated as well as systems lacking any lateral order of the adsorbates[25,48,54,56–58,81]], provided that the adsorbates show sufficient vertical order. The substrate, however, must be of high crystalline order since it is needed to generate the standing wave field, see below.

Although performing XSW experiments in normal incidence geometry (NIXSW)[1] puts strong constraints on the primary photon energy and hence on the species that can be probed, there are several important reasons to prefer this geometry. Beside the fact that the Darwin width of a Bragg reflection is maximal in this geometry, which allows for a higher resolution of the technique itself, for metal crystal substrates it is often the only option, since these crystals have a rather high mosaicity. This leads to a significant broadening of the Bragg peaks, the dominance of which (with respect to the intrinsic peak width) can be avoided by using the normal incidence geometry.

As a consequence of these features, XSW (and in particular NIXSW) have been developed into a frequently used tool for the investigation of interaction phenomena across hybrid interfaces, e.g., for atomic or molecular adsorbate layers on semiconductor or metallic substrates. The vertical distances obtained represent a "geometric fingerprint" of the vertical bonding strength[62]; by comparing these distances with the distances expected for the cases of purely covalent bonding and pure van der Waals interactions, information on the nature of the adsorbate-substrate interaction can be obtained. Furthermore, the method also yields very important benchmark data for quantum chemical calculations. The high precision and accuracy of NIXSW is essential in this context, and has been utilized for the investigation of a large number of substrate / adsorbate systems.

However, in order to attain the aforementioned high accuracy, the data analysis has to account for non-dipolar effects occurring in the photoemission process[161–165]. These corrections are necessary since (NI)XSW experiments have to be performed in a regime of relatively high photon energies, which results in relatively high kinetic energies for the photoelectrons. Under these conditions, the dipole approximation is not a good approximation any more and experimentally obtained yield curves deviate noticeably from those predicted under the dipole approximation. While the NIXSW community agrees on the necessity of correcting for these effects, it is common practice to perform the data analysis under certain simplifying assumptions. A prominent assumption – to our knowledge applied in all studies published so far – is an exact normal incidence geometry, that is, a Bragg angle of $\theta = 90°$, which simplifies the correction significantly, as discussed below. However, in the standard geometry for NIXSW experiments, as it is realized at the NIXSW beamlines used most frequently in the last decades (that are the I09 beamline of the Diamond Light Source, Oxfordshire, UK and the former

---

[1] Normal incidence refers to the lattice planes used for generating the x-ray standing wave field, *not* to the sample surface.

beamline ID32 at the European Synchrotron Radiation Facility, Grenoble, France) this condition is not precisely fulfilled as the sample is tilted by several degrees.

In this chapter, we demonstrate a correct way of analyzing NIXSW data recorded under these off-normal conditions, and discuss the consequences of neglecting the sample tilt. We find that the effect depends on the investigated system (in particular on the specific values adopted by one of the main parameters, the coherent position, see below), and that neglecting the sample tilt can falsify the results by as much as 5%, i.e., by typically up to about 0.15 Å in the adsorption height obtained. Considering that XSW is a high-precision and high-accuracy technique, and since it is being used for benchmarking DFT results, this systematic error is of significant relevance.

The chapter is organized as follows: We at first briefly review the mathematical formalism for analyzing NIXSW data, including the most general form of correcting for non-dipolar effects. We then derive the equations for non-dipolar corrections for both geometries, perfect normal incidence and the more realistic case of a slightly off-normal geometry. This demonstrates, that the correct geometry can be considered in the data analysis rather easily by using modified expressions for the non-dipolar correction parameters. Finally, we discuss the consequences of the simplified data analysis using selected exemplary experiments on the one hand, and simulated data for all possible scenarios on the other.

4.2 Non-dipolar effects in x-ray standing wave measurements

In an XSW experiment, an x-ray interference field is created by an incident x-ray beam and a Bragg-diffracted beam, i.e., the geometry of the experiment is chosen such that the Bragg condition of a certain reflection is fulfilled[142–144,161]. In practice, the photon energy is scanned through the Bragg condition, and both intensity of the reflected beam and relative phase of both beams change during this scan: While the reflected intensity shows an asymmetric peak of finite width known as the Darwin-Prins profile[166], the phase difference of incident and diffracted beam, which corresponds to the phase of the standing wave relative to the Bragg planes, changes by π during this scan. This means that the positions of the maxima and minima of the interference field shift by half the lattice spacing of the generating Bragg lattice planes, and thus they are scanned over the positions of any atomic species located within the standing wave field. As a consequence, the photon absorption of the atomic species changes in a characteristic way during scanning, depending on the position of the atoms relative to the Bragg planes. The absorption for the individual species in turn can be monitored by recording a corresponding photoelectron emission (or fluorescence) signal.

However, the photoemission yield reflects the intensity of the standing wave field at the position of the emitter only if the cross section for photoemission in the direction towards the detector is equal for both the incidence and the diffracted x-ray beams. In general, this only applies if the dipole approximation can be used to describe the photoemission process quantitatively, which is usually the case for small photon energies, and (consequently) small photoelectron kinetic energies. XSW measurements, however, have to be performed using x-rays with energies clearly above 2 keV since a Bragg condition has to be fulfilled. At such high energies, non-dipolar effects significantly distort the angular photoemission cross sections (see below and the work of Krässig *et al.*[162]), and the importance of correcting for this effect in x-ray photoemission (XPS)-based NIXSW measurements has been pointed out and verified by many authors[39,44,45,163–165,167].

A method capable of correcting for these non-dipolar effects has been developed by Vartanyants and Zegenhagen[102,163] and is frequently used. Although the mathematical formalism developed by these authors can be applied to arbitrary geometries, the actual correction equations used in practice have been derived under the simplifying assumption of perfect normal incidence. However, perfect normal incidence cannot be achieved in real experiments since the beam paths of incident and Bragg diffracted beam have to be separated in order to measure the intensity of the diffracted beam, the so-called reflectivity. Typically, the Bragg angle used is $\theta \approx 87^\circ$ rather than 90°. In the case of σ-polarization (polarization vectors perpendicular to the diffraction plane formed by incident and diffracted beam) this tilt can be neglected. But in case of π-polarization (polarization vector lies in the diffraction plane), which is most frequently used in real NIXSW measurements due to experimental constraints (horizontally polarized Synchrotron light, sample manipulator with vertically oriented main rotation axis), a deviation of only a few degrees from normal incidence already leads to a significant change in the values of the non-dipolar correction factors that should be used for the data analysis, as we will show in the following.

4.2.1 The origin of non-dipolar effects

In this section we briefly review non-dipolar effects as they are usually considered in NIXSW data analyses at present. We widely follow the mathematical treatment introduced by Vartanyants and Zegenhagen in ref. 102.

Let us consider an x-ray beam with wavelength λ falling on the surface of a single crystal (with lattice spacing d_h) under (or close to) the Bragg condition $\lambda = 2d_h \sin(\theta)$, and being diffracted under the Bragg angle θ. The resulting interference field formed by the incident and diffracted beam can be considered as a sum of the electric fields of the incident ($\vec{E}_0$) and a particular diffracted beam ($\vec{E}_h$). Hence, for the magnitude and phase of the interference field as a function of the spatial position $\vec{r}$ we write

$$\vec{E} = \vec{e}_0 E_0 e^{-i\vec{k}_0\cdot\vec{r}} + \vec{e}_h E_h e^{-i\vec{k}_h\cdot\vec{r}}, \tag{4.1}$$

where $\vec{e}_0$ and $\vec{e}_h$ are unit vectors representing the polarization directions, $\vec{k}_0$ and $\vec{k}_h$ are the propagation vectors of both waves, and E_0 and E_h are the complex amplitudes of the two beams, respectively (see fig. 4.1). Note that in this expression we have included the time-dependence of the complex phase in the complex amplitudes E_0 and E_h.

When this electric field interacts with an electron in a core level $|i\rangle$ of an atom a, it creates an emitted photoelectron wave $|f\rangle$ with an intensity given by:

$$I \propto |M_{fi}|^2 = \left| \langle f|\vec{E}\cdot\hat{p}|i\rangle \right|^2 . \tag{4.2}$$

$\hat{p}$ is the quantum mechanical momentum operator and M_{fi} the matrix element characterizing the photoemission process. Inserting eq. 4.1 allows us to write the matrix element as

$$M_{fi} = E_0 \langle f|e^{-i\vec{k}_0\cdot\vec{r}}(\vec{e}_0\cdot\hat{p})|i\rangle + E_h \langle f|e^{-i\vec{k}_h\cdot\vec{r}}(\vec{e}_h\cdot\hat{p})|i\rangle . \tag{4.3}$$

For a photoemission process from a core level state centered at the position $\vec{r}_a$ of atom a we can split this equation into parts corresponding to the position of the atom itself (the dipolar part) and to the position of the electron $\vec{r}_e^{\,a}$ relative to the atom (the non-dipolar part), i.e., with $\vec{r} = \vec{r}_a + \vec{r}_e^{\,a}$ we find

$$\langle f|e^{-i\vec{k}_i\cdot\vec{r}}(\vec{e}_i\cdot\hat{p})|i\rangle = e^{-i\vec{k}_i\cdot\vec{r}_a} \langle f|e^{-i\vec{k}_i\cdot\vec{r}_e^{\,a}}(\vec{e}_0\cdot\hat{p})|i\rangle , \tag{4.4}$$

and therefore

$$M_{fi} = E_0 e^{-i\vec{k}_0\cdot\vec{r}_a}\left[M_0 + \frac{E_h}{E_0} e^{-i\vec{h}\cdot\vec{r}_a} M_h\right], \tag{4.5}$$

where $\vec{h} = \vec{k}_h - \vec{k}_0$ is the scattering vector. The two new transition matrix elements M_0 and M_h describe the distortion of the angular photoemission pattern due to non-dipolar contributions stemming from the incident and diffracted beams, respectively. They are given by

$$\begin{aligned} M_0 &= \langle f|e^{-i\vec{k}_0\cdot\vec{r}_e^{\,a}}(\vec{e}_0\cdot\hat{p})|i\rangle \quad \text{and} \\ M_h &= \langle f|e^{-i\vec{k}_h\cdot\vec{r}_e^{\,a}}(\vec{e}_h\cdot\hat{p})|i\rangle . \end{aligned} \tag{4.6}$$

By introducing the phase ν of the standing wave field according to $\frac{E_h}{E_0} = \left|\frac{E_h}{E_0}\right| e^{i\nu}$, and the reflectivity $R = \left|\frac{E_h}{E_0}\right|^2$ we thus obtain for the photoemission

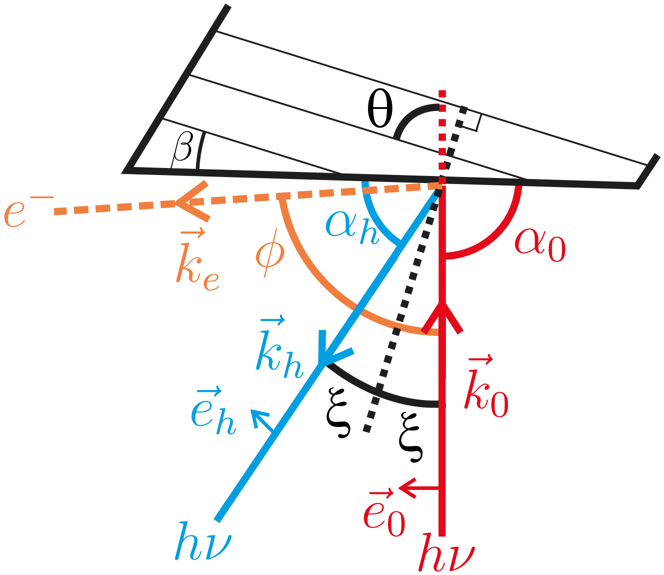

Figure 4.1: Schematic overview of the commonly used NIXSW geometry for π-polarized x-rays. The directions of incident ($\vec{k}_0$) and diffracted ($\vec{k}_h$) x-ray beams are represented by red and blue arrows, respectively, and $\vec{e}_0$ and $\vec{e}_h$ indicate the polarizations of the beams. The angle $2\xi = 180 - 2\theta$ indicates the deviation from normal incidence diffraction geometry, whereby θ is the Bragg angle, i.e., the angle of incident (and diffracted) beam to lattice planes. The angles between incident and diffracted beam to the surface are indicated as α_0 and α_h, respectively, β represents the angle between the surface and the lattice planes. The direction under which the photoelectrons are detected is indicated by a dashed orange arrow ($\vec{k}_e$). The electron emission angle ϕ is defined relative to the incident x-ray beam.

intensity

$$\begin{aligned} I &\propto |M_{fi}|^2 \\ &= |E_0|^2 \left[|M_0|^2 + |M_h|^2 R + 2\sqrt{R}\,\mathrm{Re}\left\{ M_0^* M_h e^{i(\nu - \vec{h}\cdot\vec{r}_a)} \right\} \right]. \end{aligned} \tag{4.7}$$

where M_0^* is the complex conjugate of M_0. Now we introduce the angular emission parameters S_{00}, S_{hh} and S_{0h}

$$S_{00} = |M_0|^2, \quad S_{hh} = |M_h|^2, \quad \text{and} \quad S_{0h} = M_0^* M_h, \tag{4.8}$$

as well as the non-dipolar parameters S_R and S_I, the latter commonly being separated into its absolute value $|S_I|$ and phase ψ:

$$S_R = \frac{S_{hh}}{S_{00}} \qquad \text{and} \qquad S_I = \frac{S_{0h}}{S_{00}} = |S_I| e^{i\psi}. \tag{4.9}$$

Using these parameters, the emitted photoelectron intensity I and photoelectron yield Y can be written as

$$\begin{aligned} I &\propto |E_0|^2 \left[S_{00} + S_{hh} R + \sqrt{R}\,\mathrm{Re}\Big\{ S_{0h} e^{i(\nu - \vec{h}\cdot\vec{r}_a)} \Big\} \right], \\ Y &= \frac{I}{I_0} = 1 + S_R R + 2|S_I|\sqrt{R}\cos\Big(\nu - 2\pi P_a^h + \psi\Big), \end{aligned} \tag{4.10}$$

where $I_0 \propto |E_0|^2 S_{00}$ is the photoelectron intensity at an off-Bragg excitation energy (that is an energy where the relative intensity of the diffracted beam R is negligible) and $2\pi P_a^h = \vec{h} \cdot \vec{r}_a$ refers to the vertical position of the atom a relative to the scattering planes.

According to eq. 4.6, M_0 and M_h, and therefore also S_{00}, S_{hh} and S_{0h} depend on the momentum of the emitted electron, and thus on the angle ϕ between the incident beam and the emitted electron. S_{00} and S_{hh} reflect the angular dependence of the photoelectron wave excited by the incident and diffracted beam respectively, whereas S_{0h} quantifies the interference between these two photoelectron waves. S_R, $|S_I|$ and ψ then parameterize the effect of the distortion of the angular emission patterns by non-dipolar effects on the measured yield curves.

So far we have only considered systems in which the product $\vec{h} \cdot \vec{r}_a$ is the same for all atoms that contribute to the measured yield curves. Physically speaking, this corresponds to a situation in which all atoms are at equivalent positions with respect to the nearest Bragg plane. However, in realistic systems there will always be some atoms at different positions, at least because of disorder, but also often because the same chemical species occupies multiple adsorption sites, because of surface reconstructions, or, in the case of molecules, because of tilting or bending of the molecules. In such cases, the total yield curve will contain contributions from all these atoms. These effects can be described by introducing a distribution function $\rho(\vec{r})$ for the atomic species in question, and rewriting eq. 4.10 as

$$Y = 1 + S_R R + \sqrt{R}\,\mathrm{Re}\Big\{ S_{0h} e^{i\nu} \int d\vec{r} \rho(\vec{r}) e^{-i\vec{h}\cdot\vec{r}} \Big\}. \tag{4.11}$$

Introducing the so-called coherent fraction F^h and coherent position P^h defined by

$$F^h e^{2\pi i P^h} = \int d\vec{r} \rho(\vec{r}) e^{-i\vec{h}\cdot\vec{r}}, \tag{4.12}$$

leads to the well known equation for the XSW yield

$$Y = 1 + S_R R + 2|S_I|\sqrt{R}F^h \cos\Big(\nu - 2\pi P^h + \psi\Big). \tag{4.13}$$

The coherent fraction can be understood as an order parameter since it can have values between 0 and 1 depending on the distribution function $\rho(\vec{r})$. For instance, a distribution close to a delta function (i.e., when all atoms of the considered species are at equal positions relative to the Bragg planes) will give a coherent fraction close to unity, making eq. 4.13 identical with eq. 4.10. Note that this also occurs when the atomic species are separated by integer multiples of the spacing d_h of the Bragg planes. If on the other hand the distribution function is very broad (corresponding to vertical disorder of the atomic species relative to the lattice planes), or if it consists of multiple peaks separated by a distance that is not close to an integer multiple of d_h (e.g., corresponding to multiple site adsorption), the coherent fraction will be significantly smaller and can even fall to zero. For systems with a high coherent fraction, the effective coherent position can be interpreted as the average vertical position of the atoms considered, given in units of d_h, and – owing to the mentioned d_h modulo-uncertainty – also taking values between 0 and 1. For low coherent fractions it can only be interpreted as a weighted mean of the distribution function.

One way to approximate the final state of a photoemission experiment is to write it as a sum of spherical waves. Assuming an s-initial state and typical excitation energies used in NIXSW experiments, the emitted photoelectron can be approximated very well as just a combination of p- and d-waves. The general form of the matrix elements in eq. 4.6 then becomes:

$$\begin{aligned} M &= M_{p\leftarrow s} + M_{d\leftarrow s} \\ &= \langle p|e^{i\vec{k}\cdot\vec{r}_e{}^a}(\vec{e}\cdot\hat{p})|s\rangle + \langle d|e^{i\vec{k}\cdot\vec{r}_e{}^a}(\vec{e}\cdot\hat{p})|s\rangle\,, \end{aligned} \tag{4.14}$$

and thus

$$|M|^2 = |M_{p\leftarrow s}|^2 + 2\,\mathrm{Re}\big\{M^*_{p\leftarrow s}M_{d\leftarrow s}\big\} + |M_{d\leftarrow s}|^2. \tag{4.15}$$

The first term involving only excitations to the p-wave represents the dipolar term, while the second describes the first-order correction to the angular emission patterns, caused by the interference between the p- and d-waves. At typical excitation energies used in NIXSW experiments, the third term involving only excitations to d-waves, is much smaller than the others and will therefore be neglected in the following. From eqs. 4.6 and 4.8 we then derive the angular emission parameters S_{00}, S_{hh} and S_{0h} for this case[163,168]:

$$S_{00} = \frac{3\sigma^D}{4\pi}(\vec{e}_0 \cdot \vec{n}_e)^2 \left(1 + \frac{\gamma'}{3}(\vec{s}_0 \cdot \vec{n}_e)\right), \tag{4.16}$$

$$S_{hh} = \frac{3\sigma^D}{4\pi}(\vec{e}_h \cdot \vec{n}_e)^2 \left(1 + \frac{\gamma'}{3}(\vec{s}_h \cdot \vec{n}_e)\right), \text{ and} \tag{4.17}$$

$$S_{0h} = \frac{3\sigma^D}{4\pi}(\vec{e}_0 \cdot \vec{n}_e)(\vec{e}_h \cdot \vec{n}_e) \left(1 + \frac{\gamma^*(\vec{s}_0 \cdot \vec{n}_e) + \gamma(\vec{s}_h \cdot \vec{n}_e)}{6}\right) \tag{4.18}$$

Here, σ^D is the dipole cross-section of the photoemission process, and $\vec{s}_0$, $\vec{s}_h$ and $\vec{n}_e$ are unit vectors pointing in the propagation direction of the incident beam, diffracted beam and emitted photoelectron wave, respectively. The parameter $\gamma = \gamma'(1 + i\tan(\Delta))'$ and its complex conjugate γ^* contain the non-dipolar parameter γ', which quantifies the contribution of the emitted d-wave to the photoemission intensity. $\Delta = \delta_d - \delta_p$ is the phase difference between the emitted p- and d-waves.[2]

We now introduce the polarization factor P and the non-dipolar distortion factors Q_0 and Q_h for the incident and diffracted beam, respectively,

$$P = \frac{\vec{e}_h \cdot \vec{n}_e}{\vec{e}_0 \cdot \vec{n}_e}, \; Q_0 = \frac{-\gamma'}{3}(\vec{s}_0 \cdot \vec{n}_e), \text{ and } Q_h = \frac{\gamma'}{3}(\vec{s}_h \cdot \vec{n}_e), \tag{4.19}$$

allowing us to write S_R and S_I as

$$S_R = P^2 \frac{1 + Q_h}{1 - Q_0}, \text{ and} \tag{4.20}$$

$$S_I = \frac{P}{1 - Q_0}\left[1 + \frac{Q_h - Q_0}{2} + i\tan(\Delta)\frac{Q_h + Q_0}{2}\right]. \tag{4.21}$$

For perfect normal incidence ($2\theta = 180°$), $\vec{e}_h = \vec{e}_0$ and $\vec{s}_h = -\vec{s}_0$, therefore $P = 1$, and $Q_h = Q_0 \equiv Q$ (see fig. 4.1 and eq. 4.19). Hence, eqs. 4.20 and 4.21 reduce to their well-known form

$$S_R = \frac{1 + Q}{1 - Q} \qquad \text{and} \qquad S_I = \frac{1 + iQ\tan\Delta}{1 - Q}. \tag{4.22}$$

However, as mentioned above, in a typical NIXSW measurement the sample is tilted slightly (i.e., $2\theta = 180° - 2\xi$ with typically $\xi \approx 3°...4°$) since the diffracted beam has to be spatially separated from the incident beam so

---

[2] Note that many authors, especially those discussing non-dipolar effects in conventional XPS measurements, neglect the complex nature of γ and simply refer to γ' as γ instead. Here we have adopted the convention used by Vartanyants and Zegenhagen in ref. 102 which stresses the complex nature of γ. Typically only the real part γ' is provided in the literature, together with the phase shift Δ.

that its intensity, and thus the total reflectivity, can be recorded. In addition, the synchrotron light is π-polarized in a typical NIXSW experiment, since the sample surface plane is usually oriented vertically while the synchrotron light is horizontally polarized. The exact geometry is depicted in fig. 4.1. Hence, eqs. 4.20 and 4.21 have to be used instead of eq. 4.22, with:

$$\begin{aligned} &P = \frac{\sin(\phi - 2\xi)}{\sin(\phi)}, \\ &Q_0 = \frac{\gamma'}{3}\cos(\phi), \text{ and } \; Q_h = \frac{\gamma'}{3}\cos(\phi - 2\xi), \end{aligned} \tag{4.23}$$

where ϕ is the angle between the emitted electron and the incident beam. Note that even in the dipolar case, when $\gamma' = 0$, we find that $S_R = P^2$, $S_I = P$ and $P \neq 1$. Therefore the correction parameters according to eq. 4.22 are not the correct ones also in this case.

Consequences of non-dipolar effects for the photoelectron yield

The principal influence of non-dipolar effects on the (angular dependent) photoelectron yield is shown in the polar diagrams depicted in fig. 4.2a and b for the case of $2\xi = 0°$ and $2\xi \neq 0°$, respectively. Black and red lines represent the photoemission distribution (as a function of the emission direction ϕ) caused by the incident and diffracted beam, as calculated from eq. 4.16 (S_{00}) and eq. 4.17 (S_{hh}), respectively. We have used $\gamma' = 1.06$ in these plots, corresponding to the photoemission from a C 1s state excited with a photon energy of $h\nu = 2.63$ keV (as in the case of NIXSW experiments using the (111) Bragg reflection of the Ag crystal).

We first discuss the situation for perfect normal incidence, see fig. 4.2a. Since the momentum of the incident photons is transferred to the emitted photoelectrons, the angular photoemission pattern is typically distorted in the propagation direction of the photon beam, i.e., the photoemission pattern is bent in the direction of propagation of the photon beam, towards the bulk for the incident, and towards the vacuum for the diffracted beam.Neglecting this effect, which is precisely what is done in the dipole approximation of the photoemission process, causes an under- or overestimation of the contribution to the NIXSW yield of the signal excited by the diffracted beam relative to that of the incident beam. If we, for instance, consider the emission direction indicated by the angle labeled ϕ in fig. 4.2 (this is above the crystal surface), it is obvious that the cross-section for photoemission excited by the diffracted beam (S_{hh}) is significantly higher than that for the incident beam (S_{00}), whereas in the dipole approximation both cross-sections are equal. This effect plays a significant role for the central part of a NIXSW scan (close to the Bragg energy, 'on-Bragg'), since there the intensity of the diffracted beam is strong. On the other hand, far away from the Bragg energy, where the scan usually starts and ends (this 'off-Bragg' photoelectron yield is used

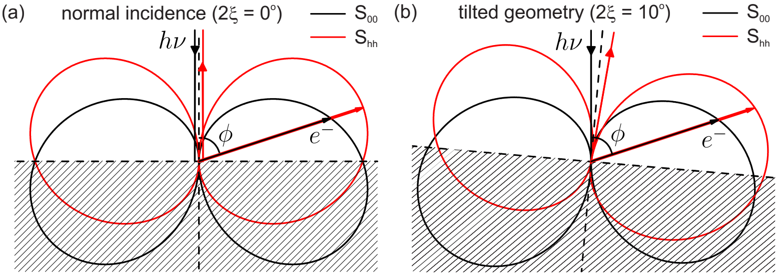

Figure 4.2: Angular distribution of the emitted photoelectrons, i.e., the magnitude of S_{00} and S_{hh}, plotted in a polar diagram as a function of the electron emission angle ϕ. (a) corresponds to the case of perfect normal incidence geometry, (b) to an off-normal geometry with $2\xi = 10°$. In both cases $\gamma' = 1.06$.

to normalize the yield curves), the diffracted intensity tends to zero and non-dipolar effects play no role. The shape of the yield curve is therefore distorted by nondipolar effects, falsifying mainly the coherent fraction, but to some extent also the coherent position that is obtained from fitting. This distortion of the yield curve is exactly what is corrected for by taking S_R and S_I into account, since these parameters scale those terms in the equation for the calculated NIXSW yield curve (second and third terms of eq. 4.13) that involve diffracted-beam induced photoelectrons. Finally, we mention that the two curves in fig. 4.2a cross each other for $\phi = 90°$, indicating that non-dipolar effects vanish for (and only for) electrons emitted perpendicular to the beam.

The effect of tilting the sample by ξ relative to normal incidence, so that the Bragg angle is reduced to $2\theta = 180° - 2\xi$, is depicted in fig. 4.2b. As before, the angular photoemission patterns are distorted in the forward direction of the exciting beams, but additionally the beams (and with them the emission patterns) are tilted in opposite directions in order to furthermore fulfill the Bragg condition. This breaks the left-right symmetry of the photoelectron emission pattern and, in our example depicted in fig. 4.2b, enhances the described non-dipolar effect on the left-hand side whereas on the right-hand side it is reduced. This means that in general, for a proper correction of the non-dipolar effect, the correction parameters have to be smaller (larger) when the sample is turned in a way that its surface normal points towards (away from) the electron analyzer. Note that the points with $S_{00} = S_{hh}$ no longer correspond to $\phi = 90°$, i.e., the common belief that non-dipolar effects vanish for electrons emitted perpendicular to the beam does not hold for a realistic geometry of the experiment.

Quantitatively, this situation is considered by the general equations for S_R and S_I (eqs. 4.20 and 4.21). In fig. 4.3 we plot the values of S_R, $|S_I|$ and ψ (the two latter being absolute value and phase, respectively, of the complex parameter S_I), as a function of ϕ for three different tilt angles $2\xi = -7°$, $0°$ and $7°$. The range chosen for ϕ corresponds to the typical acceptance angle of modern wide-angle electron analyzers, such as the one in use at beamline I09 of the Diamond Light Source (Didcot, UK). These graphs show that neglecting even such a relatively small tilt angle of $2\xi = 7°$ causes an error of up to 0.1 and 0.05 for S_R and $|S_I|$, respectively, at the edges of the angular acceptance range of the analyzer. The effect on the value on ψ is less relevant since it merely represents a small, constant offset.

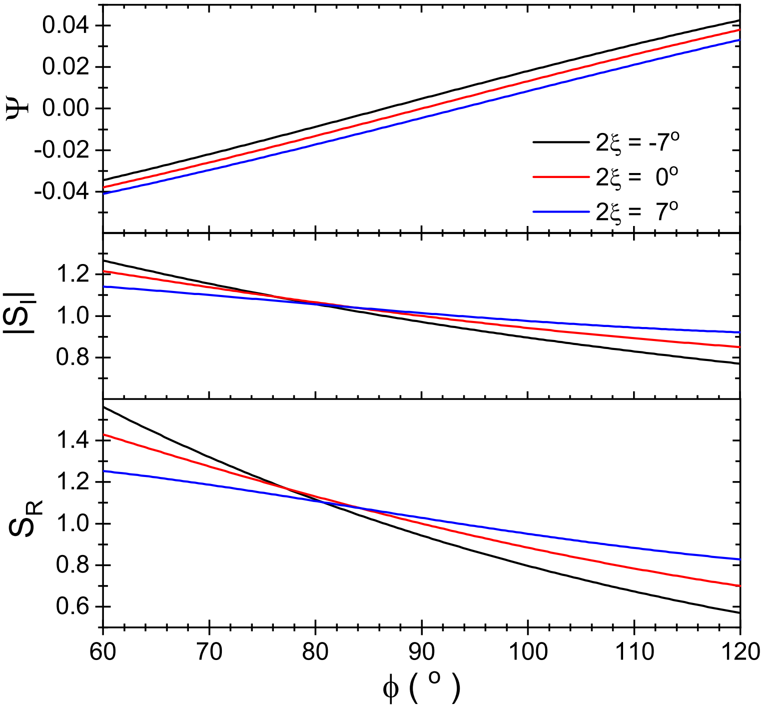

Figure 4.3: Correction factors S_R and S_I (the latter represented by its absolute value $|S_I|$ and phase ψ) for photoemission from a C 1s orbital, plotted versus the electron emission angle ϕ for different tilt angles 2ξ. We have used $h\nu = 2.63$ keV, $\gamma' = 1.06$ and $\Delta = -0.297$.

4.3 Influence of non-normal incidence correction on experimental data

In this section we demonstrate the influence of the off-normal incidence conditions discussed above on XSW data using three examples. We selected the most extreme cases regarding molecular order, namely on the one hand a (with respect to adsorption heights) completely disordered adsorbate system, and on the other hand two systems with all atomic species being very well ordered: The first is a thick incoherent binary film of SnPc and PTCDA molecules on Ag(111) that can be used to experimentally obtain the value of one of the correction factors for non-dipolar effects (S_R). The second and third example, a well ordered PTCDA monolayer on Ag(111) and the H-passivated 6H-SiC(0001) crystal surface, are selected in order to demonstrate the influence of the sample tilt effect in a complete NIXSW data analysis, i.e., on the obtained values for both coherent fraction and position.

4.3.1 Disordered systems

The first experiment was performed on a sample prepared by codeposition of nominally ≈ 15 layers of SnPc and PTCDA onto a (111) oriented Ag crystal at liquid nitrogen temperature. Cooling was applied in order to avoid any during- or post-deposition ordering of the molecules. Furthermore, we recorded the data using the $(11\bar{1})$ rather than the (111) reflection to ensure than, even in the case of a small amount of vertical ordering, the XSW yield curves correspond to a coherent fraction of zero for all atomic species. Introducing $F^h = 0$ in eq. 4.13 leads to

$$Y = 1 + S_R R, \tag{4.24}$$

which demonstrates that the parameter S_R can be obtained from such an experiment. Since we recorded the data for multiple electron emission angles in the range $73° \leq \phi \leq 108°$ with respect to the incident beam, we can also access the ϕ-dependence of the parameter S_R in this experiment.

Furthermore, since eqs. 4.20 and 4.23 show that for a given tilt angle 2ξ the dependence of S_R on ϕ is purely determined by γ', we can determine the ϕ-independent parameter γ' individually for each atomic species, by fitting the measured yield curves with eq. 4.24.

In fact, we applied a three-step fitting procedure to obtain experimental values for γ'. In the first step, the software package Torricelli[130] was used to fit the experimentally obtained intensities of the diffracted beam as a function of photon energy. In this way, the reflectivity R was obtained, as well as the shift of the Bragg energy and the experimental broadening of the reflectivity curve caused by imperfections in the crystal and finite band width of the monochromator. Since the $(11\bar{1})$ planes of a (111)-oriented fcc crystal were used in our experiment, the deviation from perfect normal incidence $\xi \neq 0$ causes the surface asymmetry parameter

$$b = \frac{-\sin(\alpha_0)}{\sin(\alpha_h)}, \tag{4.25}$$

to deviate from -1. α_0 and α_h are the angles between the surface plane and the incident and diffracted beam, respectively, i.e., $\alpha_0 = \theta - \beta = 90° - \xi - \beta$ and $\alpha_h = 90° - \xi + \beta$, where β is the angle between the surface and the diffraction planes. For either perfect normal incidence ($\xi = 0$) or when the used diffraction planes lie parallel to the surface ($\beta = 0$), obviously $b = -1$ is valid. But in the general case b deviates from -1, which changes the Darwin-Prins profile to be used for fitting the reflectivity curve. Note that in our case of a (111) oriented surface and using the $(11\bar{1})$ diffraction planes, $\beta = 180° - \arccos(-1/3)$, with $\arccos(-1/3) = 109.47°$ being the angle of a tetrahedron.

However, in practice, it is difficult to determine the precise values for α_0 and α_h, since most samples have an unknown (although usually small) miscut. There is therefore some uncertainty in the b-parameter. On the other hand, a slightly incorrect value for b, in first approximation, only changes the amplitude of the reflectivity curve, i.e., it can be corrected by a ϕ-independent scaling parameter c. Hence, the second step in our analysis procedure is to fit the experimental yield curves using the equation

$$Y = 1 + \tilde{S}_R \cdot R, \tag{4.26}$$

where R is the reflectivity obtained in the first analysis step and $\tilde{S}_R(\phi) = c \cdot S_R(\phi)$ is the actual fitting parameter. This is performed for all electron emission angles ϕ separately, which results in ϕ-dependent data as it is exemplarily shown in fig. 4.4a.

Subsequently, as the third step of the analysis, we obtain the values for c and γ' from fitting the $\tilde{S}_R(\phi)$ data using (cf. eqs. 4.20 and 4.23)

$$\tilde{S}_R(\phi) = c \cdot \left(\frac{\sin(\phi - 2\xi)}{\sin(\phi)} \right)^2 \frac{1 + \frac{\gamma'}{3} \cos(\phi - 2\xi)}{1 - \frac{\gamma'}{3} \cos(\phi)}. \tag{4.27}$$

This fit is also shown in fig. 4.4a and yields the correction factor c for the uncertainty of the b-parameter, and γ' representing the desired ϕ-independent non-dipolar correction parameter.

We have performed the fitting for a (realistic) sample tilt of $2\xi = 7.0°$ and, for comparison, for $2\xi = 0.0°$, the latter corresponding to the hypothetic perfect normal incidence geometry. Figure 4.4b illustrates the results. The values for γ' obtained for both geometries in eight different measurements covering three different atomic species are shown, as well as theoretical values of γ' calculated according to ref. 169. It can be clearly seen that using the

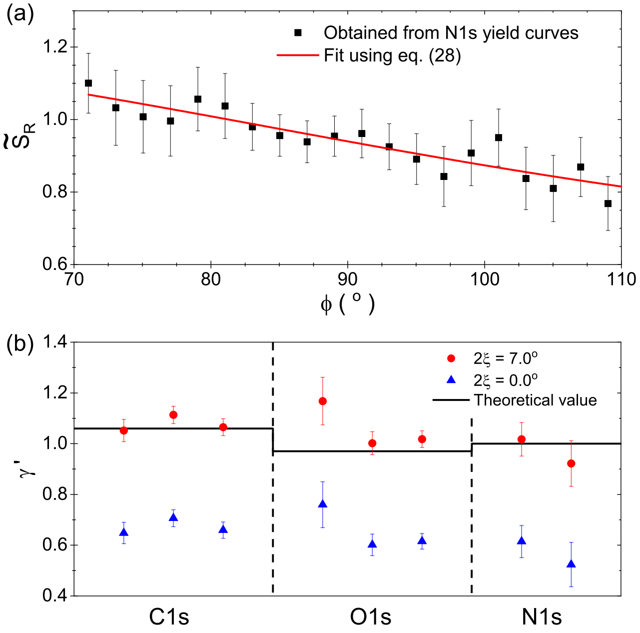

Figure 4.4: Fitting procedure to obtain the non-dipolar parameter γ', and results for the atomic species investigated: (a) S_R values for the N 1s core level as a function of the electron emission angle ϕ. Each data point represents the result of fitting eq. 4.26 to the corresponding yield curve obtained for a thick disordered organic layer on Ag(111) in $(11\bar{1})$ reflection geometry. The black line represents the best fit to the $\tilde{S}_R(\phi)$ data using eq. 4.27, and resulting in $\gamma' = 1.02$ for this case. (b) Values for γ', as obtained by this procedure, for all atomic species investigated in this work, and assuming either perfect normal incidence (blue data points), or an angle between the incident and diffracted beam equal to $2\xi = 7.0°$ (red data points). Black lines represent calculated values according to ref. 169.

approximation for perfect normal incidence when the real geometry is off-normal leads to a systematic underestimation of γ', whereas the off-normal corrected fitting procedure yields γ'-values that lie within two standard deviations of the theoretical value.

4.3.2 Well-ordered systems

In this section we discuss the effect of a tilted sample on the NIXSW fitting results for well-ordered systems using two different well-studied examples. The first is a monolayer of PTCDA on Ag(111), the so-called herringbone structure, representing a model system for the study of interactions between molecules and metal surfaces for the case of weak chemisorption[24,25,34,98,170,171]. The molecules adsorb on the surface in a flat-lying geometry, interacting with the surface primarily via their electronic π system, and are slightly bent due to a local interaction of the oxygen species with the substrate. The adsorption heights of the individual species are therefore well defined, and for the carbon species values between 2.8 Å and 2.9 Å have been obtained. Coherent fractions in the range of $0.5 - 0.7$ have been reported so far[25,170].

The second example is a H-passivated (0001) oriented surface of a 6H-SiC bulk crystal. For this system it is known that, owing to the H-passivation, no significant surface relaxation takes place[172]. Both species therefore lie on bulk positions, corresponding to $P^h = 0.02$ for Si and $P^h = 0.76$ for C. Coherent fractions are expected to be close to unity, but values between $F^h = 0.8$ and 1.23 have been reported in the literature[172,173].

For both systems we have obtained data sets in a geometry close to normal incidence, and fitted the data with and without considering the experimental tilt angle of $2\xi = 7.0°$. For the presentation of the results we make use of the Argand diagram, a polar diagram in which the fitting results are represented by a polar vector $\vec{X}$. Its absolute value and phase angle correspond to the coherent fraction F^h and position P^h, respectively. When comparing the fit results with and without consideration of the sample tilt, it is useful to consider the difference vector of the corresponding two polar vectors, that is,

$$\Delta\vec{X} = \vec{X}_{2\xi=7.0^\circ} - \vec{X}_{2\xi=0.0^\circ}. \tag{4.28}$$

In fig. 4.5 we have plotted these difference vectors in the Argand diagram with their origin at the position of the heads of $\vec{X}_{2\xi=0.0^\circ}$, i.e., the vectors displayed in this diagram represent the corrections that have to be applied to $\vec{X}_{2\xi=0.0^\circ}$ in order to consider a sample tilt of $2\xi = 7.0°$. This correction depends on the electron emission angle ϕ (see color-code). We show only the relevant sections of the Argand diagram for each of the three species, namely C 1s in PTCDA/Ag(111), Si 2s in SiC and C 1s in SiC.

In all three cases the differences between uncorrected and corrected data points increase with decreasing ϕ, that is, with increasing deviation from grazing emission, as expected from fig. 4.2. However, in addition to that, it can also be seen that for C 1s in PTCDA and Si 2s in SiC the difference vectors are generally much longer than for C 1s in SiC, for which the differences are almost negligible. We quantify this difference by plotting the absolute magnitude of the deviation vectors $\left|\Delta\vec{X}\right|$ in fig. 4.6 for the three systems. These plots confirm that the absolute value of the correction increases as ϕ becomes less grazing for PTCDA on Ag(111) and for 6H-SiC

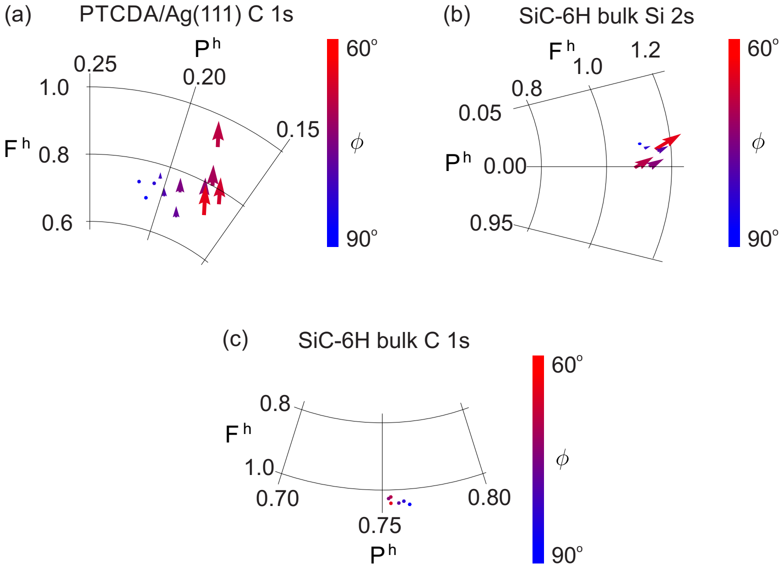

Figure 4.5: Sections of an Argand diagram indicating the effect of the tilt-correction on coherent positions and fractions. The corrections $\Delta\vec{X}$ (see eq. 4.28) are plotted for different measurements of (a) the C 1s emission from 1 ML PTCDA on Ag(111), (b) Si 2s, and (c) C 1s emission from a 6H-SiC(0001) bulk crystal. The lengths of the arrows indicate the magnitude of the correction, the color code the electron emission angle ϕ. Data presented in b and c were measured by F. Bocquet.

bulk Si. On the other hand, we also see that $\left|\Delta\vec{X}\right|$ remains negligible for the 6H-SiC bulk C measurements, indicating that the magnitude of the deviation is strongly system-dependent.

In order to understand this finding, we performed a systematic analysis on simulated yield curves. For the parameters $\gamma' = 1.0$ and $\Delta = -0.30$ (exemplarily selected and corresponding to C 1s photoelectrons as studied for both systems reported in this section), we calculated yield curves for all possible pairs of P^h and F^h using the non-dipolar parameters obtained from the full correction formula (eqs. 4.20, 4.21 and 4.23). We assumed $2\xi = 7°$and $\phi = 70°$, corresponding to an electron emission angle rather close to the edge of the angular acceptance range of the analyzer.[3] Then, we fitted

---

[3] In angular mode the Scienta EW 4000 analyzer at beamline I09 of the Diamond Light Source accepts photoelectrons emitted under $\phi = 62° ... 118°$.

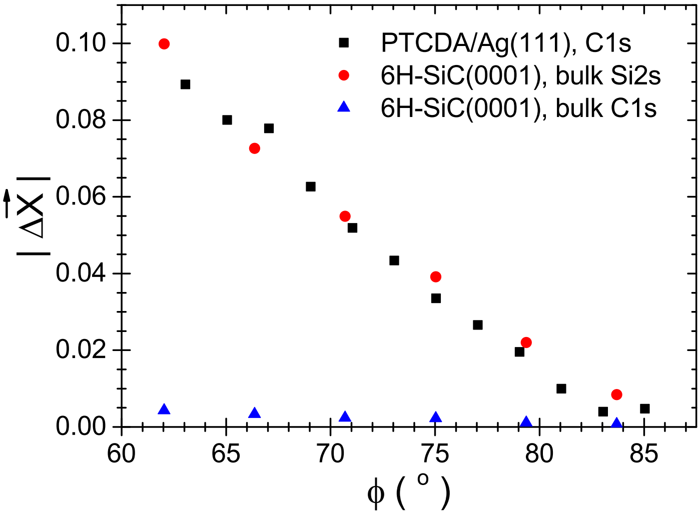

Figure 4.6: Absolute value of $\Delta\vec{X}$ (see eq. 4.28), indicating the magnitude of the tilt-correction effect, as function of the electron emission angle ϕ, for the C 1s emission from 1 ML PTCDA on Ag(111) as well as Si 2s and C 1s emission from a 6H-SiC bulk crystal.

these simulated data curves using the non-dipolar parameters obtained for $2\xi = 0.0°$ (eq. 4.22), yielding values for the coherent fraction and position that differ from the values used for calculating the simulated data. These differences in F^h and P^h quantify the tilted-sample correction for this selected example.

In fig. 4.7 we illustrate both the original values used for calculating the simulated data and the fitted values for which the tilt effect was neglected as green and blue circles, respectively, whereby the circles indicate the positions of the heads of the corresponding polar vectors $\vec{X}$ in the Argand diagram. We have also included red arrows indicating $\Delta\vec{X}$ for selected data points, indicating the effect of applying the tilt-correction. It can clearly be seen that the deviation between simulated and fitted parameters is maximal in the upper half of the Argand diagram, i.e., for $P^h < 0.5$, and for high F^h, whereas for the lower half ($P^h > 0.5$) the deviation is smaller and sometimes almost vanishes.

We conclude that the origin of the system-dependency of the described effect is in fact this P^h- (and to some extent also an F^h-) dependency, explaining why the sample-tilt effect is much bigger for the C species of PTCDA on Ag(111) and for Si in 6H-SiC than for the C species in 6H-SiC. The origin of this asymmetry can be rationalized by noting that the difference

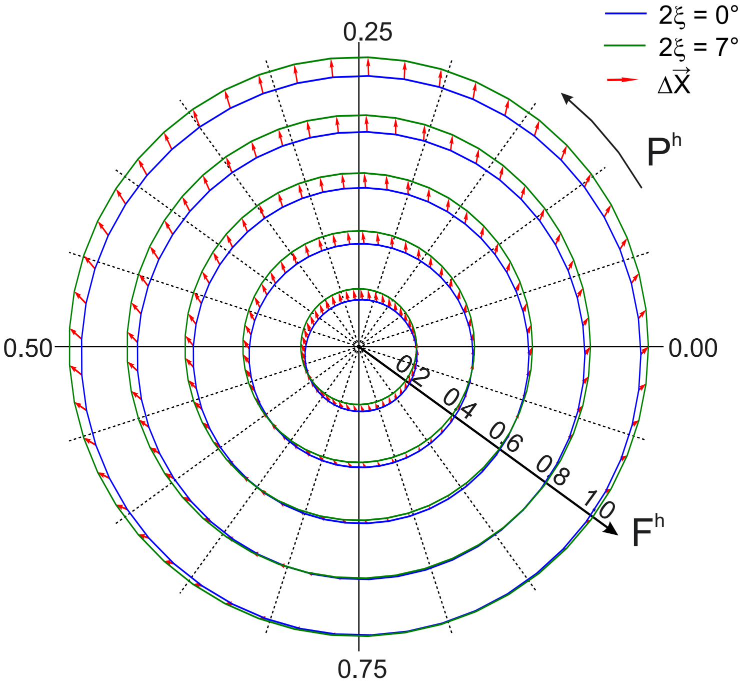

Figure 4.7: Illustration of the tilt-correction effect. The correction vectors ΔX are calculated in the full parameter range of the Argand diagram and plotted as red arrows. The green circles correspond to simulated data with consideration of a $2\xi = 7.0°$ sample tilt (using eqs. 4.20, 4.21 and 4.23), the blue circles to best fits of eq. 4.22 (i.e., with neglected sample tilt, $2\xi = 0.0°$) to the simulated data, for details see text. The calculations were performed for C 1s photoelectrons ($\gamma' = 1.0$ and $\Delta = -0.30$).

between the perfect normal incidence correction and the full correction is mainly due to the polarization factor P defined in eq. 4.23. If we set γ' and Δ to zero, the expression for the yield curves can be written as

$$Y = 1 + P^2 R + 2F^h \sqrt{P^2 R} \cos\Big(\nu - 2\pi P^h\Big). \tag{4.29}$$

This indicates that the polarization factor effectively re-scales the reflectivity R, and hence the effect is maximal in those parts of the Argand diagram where the interference term is in phase with the reflectivity and minimal where it is out of phase. For small values of γ' and Δ, this corresponds to $P^h \approx 0.25$ and $P^h \approx 0.75$, respectively.

4.4 Summary

We have shown that – in agreement with the literature[102,163] – for arbitrary experimental geometries and s-initial states the non-dipolar parameters S_R, $|S_I|$ and ψ can be parameterized in terms of a polarization factor P and two non-dipolar distortion factors Q_0 and Q_h (see eqs. 4.19 to 4.21). Furthermore, we have derived equations for P, Q_0 and Q_h for the specific case of π-polarized x-rays (eq. 4.23) that is usually realized in NIXSW experiments. Using these expressions, we have shown that even in the case of a relatively small deviation from perfect normal incidence (i.e., for a sample tilt of only a few degrees), the values obtained for S_R and $|S_I|$ can deviate significantly from those obtained by assuming a perfect normal incidence geometry, depending on the direction and magnitude of the tilt, and on the angle between the incident beam and the emitted photoelectrons.

Since (NI)XSW is considered to be a highly precise method to determine vertical distances at surfaces and interfaces, such as atomic and molecular adsorption heights and bonding distances, and since these numbers are frequently used as benchmarks for DFT calculations, a correct consideration of non-dipolar corrections is very important. Using selected examples we demonstrate the magnitude of the sample-tilt effect, and identify different cases for which the effect is most significant. The examples are (i) a disordered thick film containing two different molecular species, (ii) two well ordered systems, namely a single molecular adsorbate layer on a metal substrate and an unreconstructed surface of a bulk crystal, and (iii) simulated data covering the entire possible parameter space for the coherent fraction and position (that is, the entire Argand diagram).

From the first example the parameter γ', which is correlated to the parameters Q_0 and Q_h but independent of the electron emission angle ϕ (see eq. 4.19), was determined for C1s, N1s and O1s core level emission. We find that neglecting a crystal tilt of 3.5° leads to an underestimation of the value for γ' by up to 30% compared to the theoretical values reported in the literature[169]. However, when considering the tilt, our experimentally obtained values for γ' agree very well with theoretical values. For the second example, the well-ordered systems PTCDA/Ag(111) and 6H-SiC(0001), we have found significant deviations of the values for the coherent fraction and position caused by neglecting the crystal tilt. However, the results were very diverse and did not reflect any species-specific trends. This made us investigate the entire range of possible coherent fractions and positions using simulated data (example iii): We have calculated some yield curves for all possible parameters (coherent fractions and positions) using the full formalism including sample tilt (eqs. 4.13, 4.20 and 4.21), and fitted them using eqs. 4.13 and 4.22, i.e., with neglected sample tilt. A comparison of the corresponding parameters illustrates the effect of neglecting the sample tilt. We found that the effect is strongest in the upper half of the Argand diagram, that is for $P^h < 0.5$, whereas in the lower it is small, around $P^h \approx 0.75$ even almost negligible.

Furthermore, we found a significant dependency of the nondipolar effects on the emission angle of the photoelectron in all cases. Although this finding might not be very surprising, it does have important consequences on the way XSW data must be recorded to allow a proper data correction, and hence it has strongest impact on past, present and future XSW experiments. The electron analyzers used at modern XSW beamlines have a rather large angular acceptance, ±30° is a typical value. If this large angular range is fully (or to a significant part) used in the XSW experiment, the obtained yield curves are the result of (implicit) integration over this angular range, at least if the data is recorded in the so-called transmission mode that yields the best efficiency. However, this integration makes a proper correction of non-dipolar effects impossible. For a proper correction, electrons detected at each and every different emission angle have to be treated with different correction factors, which is not possible after integration. Using averaged correction factors can *not* be a proper solution, since the detected intensities from various electron emission angles are very different, they may differ up to a factor of 100 or more. Hence, a weighted averaging of the correction factors would be required, but the weighting function is unknown and can hardly be determined since it depends not only on the analyzer, but also on the type of the sample and the precise experimental geometry. The only reasonable way of recording data that can be properly corrected appears to be the use of the analyzer's angular resolved mode with a reasonable resolution for the electron emission angle (that is, a reasonable number of emission angle intervals, so-called 'slices'), and correcting the slices with their individual correction parameters that are valid for the corresponding emission angle. This comes at the cost of some extra effort in the data analysis, but appears to be the only proper way to exclude systematic errors introduced by the use of a tilted sample in NIXSW experiments.

4.5 Sample preparation

All measurements were performed under UHV conditions with a base pressure below 5×10^{-10} mbar. Clean Ag(111) and 6H–SiC(0001) surfaces were prepared by sputtering the surface with 500 eV Ar^+ ions under 45° and −45° off-normal incidence for at least 15 minutes each, followed by annealing at temperatures above 750 K for at least 20 minutes. Surface cleanliness after the sputter procedure was verified by XPS.

For the PTCDA herringbone monolayers and disordered multilayers, organic molecules were deposited by organic molecular beam epitaxy from dedicated, home-built Knudsen cell evaporators. Deposition rates were monitored by recording the ion current signal of typical fragments of the evaporated molecules using a mass spectrometer. The absolute deposition rate was calibrated against the mass spectrometer signals recorded for well-known homomolecular phases. For the disordered multilayers, at least 20 ML of both PTCDA and SnPc was deposited, and the sample was held at liquid nitrogen temperature. Deposition of PTCDA was performed at room temperature.

Chapter 5

Attenuation effects in NIXSW measurements

As has been highlighted in the prior two chapters, the geometric structure of surfaces and interfaces is a critical materials parameter needed for understanding and optimizing electronic devices and the (normal incidence) x-ray standing waves (NI)XSW is possibly the most precise and certainly the most generally applicable method for studying this parameter[27,47,102,141–146]. In favorable situations it can reach a precision of $< 0.02\,\text{Å}$[58,81]. In addition to that, it relies on the detection of photoelectrons, which means that different elements, and even different chemical species of the same element, can be analyzed separately. A second advantage of the XSW technique is that it does not rely on optimization of existing models and is only sensitive to vertical structure parameters. This means that it is unaffected by the phase problem that plagues diffraction techniques and it is even capable of handling systems that display large unit cells, incommensurate adsorbate structures or even a lack of lateral order of the adsorbates[25,48,54,56–58,81].

However, there is one strong limitation to the XSW technique. Each XSW technique provides only two parameters, the coherent fraction F^h and the coherent position P^h, which, respectively, correspond to the magnitude and phase of one Fourier component of the distribution function of the probed atoms. For simple distributions in which (almost) all atoms are found in the same adsorption site then P^h can be interpreted as the position of this adsorption site relative to the nearest Bragg plane, while F^h is a measure of the deviation from perfect order in this system. However, in systems with multiple adsorption sites or more complex atomic distributions, this is not sufficient to obtain an accurate description of the system and more information is required. One way to obtain more information and to reconstruct the atomic distribution function is to combine a multitude of these Fourier components obtained by performing XSW measurements at higher-order Bragg reflexes. This technique is known as XSW Imaging and although it has been successfully applied to a variety of systems, it requires the use of very high primary beam energies in order to match these higher-order Bragg conditions. At such high primary beam energies, the cross-section of photoemission from light elements such as carbon and oxygen is significantly reduced, which means that long measurements times are required. As a result of this, in practice the XSW Imaging technique is only applicable to systems that are stable under prolonged exposure to high-energy x-rays.

In this chapter we will discuss an alternative method to obtain information about the distribution of adsorbate atoms that does not require the use of higher-order reflexes and is just as fast as a single XSW measurement. Due to the short inelastic mean-free path of electrons in condensed matter, signals stemming from deeper-lying adsorption sites can be attenuated significantly compared to signals stemming from adsorption sites closer to the vacuum, an effect that has been noted before but treated as an unwanted distortion of the recorded data[46]. However, due to recent advances in the field of wide acceptance angle electron analyzers, it has become possible to record intensities over a large range of angles simultaneously during an XSW experiment. As we will show here, when data can be recorded over a wide range of angles it is possible to take advantage of attenuation effects in a manner similar to angle-resolved XPS[174,175] to obtain more information about the distribution of atoms contributing to XSW yield curves. We will show how the conventional theory of XSW measurements can be extended straightforwardly to incorporate attenuation effects. In addition to that, we will show two different methods for analyzing angle-resolved XSW data to obtain information about the atomic distribution at surfaces, one method that is mostly applicable to well-ordered multilayer systems and one more general method that is most useful to gain information about disorder in monolayer structures.

5.1 XSW experiments in the presence of multiple adsorption sites

As discussed in chapter 4, the yield curve that is measured in an XSW experiment can be described as

$$Y = \left|1 + \sqrt{R} e^{i\left(\nu - 2\pi \vec{h}\cdot\vec{r}_a\right)}\right|^2. \tag{5.1}$$

Now, imagine that the measured yield curve contains contributions of two atoms, with positions $\vec{r}_a$ and $\vec{r}_b$. In that case, the total yield measured will be the sum of the yield stemming from these two different atoms:

$$\begin{aligned}
Y &= \frac{1}{2}\left|1+\sqrt{R}e^{i\left(\nu-2\pi\vec{h}\cdot\vec{r}_a\right)}\right|^2 + \frac{1}{2}\left|1+\sqrt{R}e^{i\left(\nu-2\pi\vec{h}\cdot\vec{r}_b\right)}\right|^2 && (5.2)\\
&= 1+R+\sqrt{R}\,\mathrm{Re}\left[e^{i\left(\nu-2\pi\vec{h}\cdot\vec{r}_a\right)}\right]+\sqrt{R}\,\mathrm{Re}\left[e^{i\left(\nu-2\pi\vec{h}\cdot\vec{r}_b\right)}\right] && (5.3)\\
&= 1+R+2\sqrt{R}\,\mathrm{Re}\left[\frac{1}{2}e^{i\left(\nu-2\pi\vec{h}\cdot\vec{r}_a\right)}+\frac{1}{2}e^{i\left(\nu-2\pi\vec{h}\cdot\vec{r}_b\right)}\right]. && (5.4)
\end{aligned}$$

By introducing the coherent fraction F^h and coherent position P^h of the distribution of atoms,

$$F^h e^{2\pi i P^h} = \frac{1}{2}e^{-i\left(2\pi\vec{h}\cdot\vec{r}_a\right)}+\frac{1}{2}e^{-i\left(2\pi\vec{h}\cdot\vec{r}_b\right)}, \qquad (5.5)$$

we can finally write the equation for the XSW yield in its well-known form[142,161]:

$$\begin{aligned}
Y &= 1+R+2F^h\sqrt{R}\,\mathrm{Re}\left[e^{i\left(\nu-2\pi P^h\right)}\right] && (5.6)\\
&= 1+R+2F^h\sqrt{R}\cos\left(\nu-2\pi P^h\right). && (5.7)
\end{aligned}$$

This equation stays the same in the presence of many contributing atoms with many different adsorption heights, but in that case it is better to define the coherent position and fraction using a contribution function. For the specific case in which $\vec{h}$ is directed along the surface normal we can write:

$$F^h e^{2\pi i P^h} = \int_{-\infty}^{\infty} dz\, c(z) e^{-2\pi i \frac{z}{d_{hkl}}}, \qquad (5.8)$$

where the z-coordinate points along the surface normal and $c(z)$ quantifies how much of the total intensity contributing to the yield curve is emitted from a depth z. In the absence of any effects that distort the photoemitted intensity the contribution function $c(z)$ is simply equal to the distribution of emitters $\rho(z)$ and in that case eq. 5.8 reduces to its well-known definition that has been used for Fourier analysis of XSW yield curves:

$$F^h e^{2\pi i P^h} = \int_{-\infty}^{\infty} dz\, \rho(z) e^{-2\pi i \frac{z}{d_{hkl}}}. \qquad (5.9)$$

However, in the presence of attenuation effects this is not the case. Consider again the situation for two atoms with different adsorption heights. The signal stemming from atoms a and b will be distorted as the electrons move through the adsorbate layer to reach the vacuum. If the adsorbate layer consists mostly of light elements and if the kinetic energy of the emitted photoelectrons is high (which is often the case since XSW measurements have to be performed with high photon energies to match the Bragg condition for a given crystal), then diffraction effects will only make a very small contribution and the electrons will mainly undergo inelastic scattering. As a result of this, to first order we can approximate the adsorbate layer as a medium with a constant inelastic mean-free path λ_{in}. The signal stemming from a molecule m embedded in this medium will then be given by

$$I_m = I_{0,m} e^{-\frac{z_m}{\lambda_{in}\cos(\phi)}}, \tag{5.10}$$

where $I_{0,m}$ is the intensity that would be measured in the absence of attenuation effects, z_m is the distance from the position of m to the edge of the adsorbate layer and ϕ is the angle between the direction of the outgoing electron and the normal vector of the surface. Assuming that $I_{0,a} = I_{0,b}$, the relative contribution of molecule a to the total yield curve is then given by

$$c_a = \frac{I_a}{I_a + I_b} = \frac{e^{-\frac{z_a}{\lambda_{in}\cos(\phi)}}}{e^{-\frac{z_a}{\lambda_{in}\cos(\phi)}} + e^{-\frac{z_b}{\lambda_{in}\cos(\phi)}}}. \tag{5.11}$$

The consequence of this is that, especially in multilayer systems, the relative contribution from one of the two molecules will be attenuated significantly. For example, in fig. 5.1, we have plotted the relative contributions of two atoms that are separated by a distance of 1.0 Å as a function of the electron take-off angle, for an inelastic mean free path of 30 Å (roughly corresponding to the inelastic mean-free path of electrons with a kinetic energy of 2 keV moving through graphite[176]). It can clearly be seen that due to attenuation, under grazing conditions the signal stemming from the topmost atom is enhanced by a factor of 1.4 relative to the signal stemming from the bottom atom.

Generalizing this to the case of many different atoms described by a distribution function $\rho(z)$, we find for the contribution function $c(z)$ the following expression:

$$c(z) = \frac{\rho(z) e^{-\frac{z}{\lambda_{in}\cos(\phi)}}}{\int_{-\infty}^{\infty} dz'\, \rho(z') e^{-\frac{z'}{\lambda_{in}\cos(\phi)}}}. \tag{5.12}$$

Inserting this into eq. 5.8 then yields:

$$F^h e^{2\pi i P^h} = \frac{\int_{-\infty}^{\infty} dz\, \rho(z) e^{-\frac{z}{\lambda_{in}\cos(\phi)}} e^{-2\pi i \frac{z}{d_{hkl}}}}{\int_{-\infty}^{\infty} dz'\, \rho(z') e^{-\frac{z'}{\lambda_{in}\cos(\phi)}}}. \tag{5.13}$$

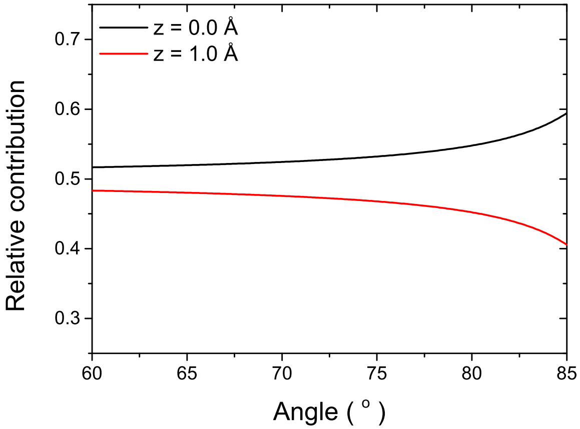

Figure 5.1: Attenuation-induced change in the relative contribution of photoemission stemming from 2 atoms separated by a distance of 1.0 Å, as a function of the electron emission angle relative to the surface normal. Here we have assumed a mean-free path of the photoelectrons of 30 Å

We now introduce the attenuation parameter s_d and the interference parameter s_i, defined as:

$$s_d = \frac{1}{\lambda_{in}\cos(\phi)}, \qquad s_i = 2\pi i \frac{1}{d_{hkl}}, \tag{5.14}$$

which allows us to write eq. 5.13 as:

$$F^h e^{2\pi i P^h} = \frac{\int_{-\infty}^{\infty} dz\, \rho(z) e^{-z\cdot(s_d+s_i)}}{\int_{-\infty}^{\infty} dz'\, \rho(z') e^{-z'\cdot s_d}} \tag{5.15}$$

The integrals in this equation can now be interpreted as Bilateral Laplace transforms of the emitter distribution function $\rho(z)$:

$$F^h e^{2\pi i P^h} = \frac{\rho_{\mathfrak{B}}\left(s_d + s_i\right)}{\rho_{\mathfrak{B}}\left(s_d\right)} \tag{5.16}$$

$$\rho_{\mathfrak{B}}(s) = \int_{-\infty}^{\infty} dz\, \rho(z) e^{-z\cdot s}, \tag{5.17}$$

which gives us an expression that can be used to calculate the expected value of F^h and P^h for a given distribution of emitters $\rho(z)$, as obtained from yield curves measured using photoelectrons leaving the surface under an angle θ, if the inelastic mean-free path λ_{in} is known.

5.2 Mean coherent positions and shape functions for well-ordered multilayer systems

In order to extract physically relevant information from the measured coherent positions and fractions we thus need to develop expressions for $\rho_{\mathfrak{B}}(s)$. If the measured system consists of well-defined layers so that the distance between adjacent layers is much larger than the disorder-induced broadening of individual layers and if the system overall is very well-ordered, then the emitter distribution function for this system can be well-approximated by a sum of Dirac-δ distributions:

$$\rho z = \sum_i a_i \delta(z - z_i), \tag{5.18}$$

$$\rho_{\mathfrak{B}}(s) = \sum_i a_i e^{-z_i \cdot s} \tag{5.19}$$

with a_i the fraction of molecules found in the i'th layer and z_i the position of the i'th layer relative to an arbitrarily chosen Bragg plane. In order to make data analysis more straight-forward it is beneficial to define the positions of the delta functions relative to the position of one of the layers instead and we will refer to this layer as the 'reference layer'. Making use of the shifting property of the Bilateral Laplace transform we can write:

$$\rho_{\mathfrak{B}}(s) = e^{-z_0 \cdot s} \bar{\rho}_{\mathfrak{B}}(s), \quad \bar{\rho}_{\mathfrak{B}}(s) = \sum_i a_i e^{-(z_i - z_0) \cdot s} \tag{5.20}$$

So that the measured coherent fraction and position are equal to:

$$F^h e^{2\pi i P^h} = \frac{e^{-z_0 \cdot (s_d + s_i)}}{e^{-z_0 \cdot s_d}} \frac{\bar{\rho}_{\mathfrak{B}}(s_d + s_i)}{\bar{\rho}_{\mathfrak{B}}(s_d)} \tag{5.21}$$

$$= e^{-2\pi i P_0^h} V(s_i, s_d), \tag{5.22}$$

$$V(s_i, s_d) = \frac{\sum_i a_i e^{-(z_i - z_0) \cdot (s_d + s_i)}}{\sum_i a_i e^{-(z_i - z_0) \cdot s}} \tag{5.23}$$

where we have introduced the coherent position of the reference layer $P_0^h = z_0 \cdot s_i = 2\pi i z_0 / d_{hkl}$. $V(s_i, s_d)$ is the first example of what we will refer to as a shape function. It is called that way because the function $V(s_i, s_d)$ does not change if the entire multilayer structure is shifted, it only depends on the 'shape' of the emitter distribution function $\rho(z)$, which in this case means that it only depends on the interlayer spacing and the relative contributions stemming from each layer. On the other hand, P_0^h does not change if the shape of the distribution function changes, as long as the position of the reference layer stays the same.

As in previous chapters we can represent these coherent fractions and positions using an Argand diagram. To recap, an Argand diagram is a representation of the data points using polar coordinate. Each data point (F^h, P^h) is represented as the head of a vector in the diagram with the length of the vector corresponding to F^h and the angle of the vector to the horizontal axis corresponding to P^h. However, in a typical angle-resolved NIXSW measurement, we do not obtain a single data point but rather we obtain the coherent position and fraction for a range of electron take-off angles ϕ. Taken together, these coherent fractions and positions can be considered as a parametric curve $\left(F^h(\phi), P^h(\phi)\right)$ in the Argand diagram. According to eq. 5.22 the overall shape of this parametric curve then depends on the shape function $V(s_i, s_d)$ while changing P_0^h rotates the curve around the origin of the Argand diagram.

To illustrate this, in fig. 5.2 we have plotted these parametric curves predicted by eq. 5.22 in the range of $60^\circ < \phi < 85^\circ$ for a typical organic bilayer system on Ag(111) (i.e. $d_{hkl} = 2.36\,\text{Å}$, $\lambda_{in} = 30\,\text{Å}$). In fig. 5.2a we have kept the position of the bottom layer fixed and varied the interlayer spacing, corresponding to changing $V(s_i, s_d)$ while keeping P_0^h fixed. As expected, the shape of the parametric curves describing the relationship between (F^h, P^h) and ϕ changes, becoming stretched and changing in tilt. On the other hand, in fig. 5.2b we have kept the interlayer spacing fixed and moved the whole bilayer system, which corresponds to keeping $V(s_i, s_d)$ fixed while changing P_0^h. It can clearly be seen that moving the whole bilayer system preserves the overall shape of these parametric curves, but they are rotated around the center of Argand diagram. Note also that in both plots, all data points lie on a straight line connecting the coherent fraction and position of the top layer to those of the bottom layer. Closer inspection of the shape function reveals that it can be written as:

$$V = \sum_i n_i \vec{X}_i \tag{5.24}$$

$$n_i = \frac{a_i e^{-z_i' \cdot s_d}}{\sum_i a_i e^{z_i' \cdot s_d}} \tag{5.25}$$

with $\vec{X}_i = e^{2\pi i P_i^h}$ a vector in the Argand diagram indicating the relative position of species i to the center of the distribution. This means that the shape function behaves like an interpolation curve connecting vectors in the Argand diagram that belong to the individual layers in the system. In

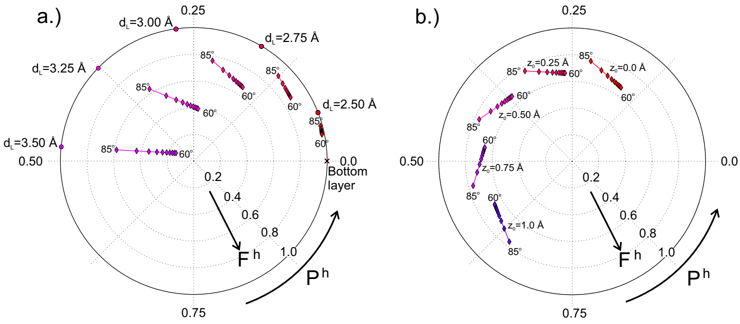

Figure 5.2: Coherent fraction and position as a function of electron take-off angle ϕ predicted by eq. 5.22 for $60° < \phi < 85°$ for a bilayer system consisting of two layers with equal number of emitters per layer, assuming a lattice spacing of $d_{hkl} = 2.36\,\text{Å}$ for the substrate generating the standing wave field and a photoelectron mean-free path of $\lambda_{in} = 30\,\text{Å}$ in the bilayer. a.) Keeping the position of the bottom layer fixed at a Bragg plane while varying the interlayer spacing from $d_L = 2.50\,\text{Å}$ to $d_L = 3.50\,\text{Å}$. Diamonds indicate predicted data points while circles and the cross indicate the coherent position of the top layer and bottom layer respectively. b.) Keeping the interlayer spacing fixed at $d_L = 3.0\,\text{Å}$ and moving the entire bilayer stack so that the position of the bottom layer varies from $z_0 = 0.00\,\text{Å}$ above the nearest Bragg plane to $1.00\,\text{Å}$ above the nearest Bragg plane.

the case of a bilayer system, the expected relationship between angle and the position of the measured data points in the Argand diagram is then particularly straight-forward. Since in this case there are only 2 layers and thus only 2 Argand vectors contributing, all data points are expected to lay on a straight line connecting these data points, as we observe in fig. 5.2.

On the other hand, in systems containing more than 2 layers, eq. 5.25 predicts that the parametric curve describing (F^h, P^h) as a function of ϕ lies in the interior of a polygon. An example of this has been depicted in fig. 5.3, where we have plotted the angle-dependent coherent fractions and positions predicted by eq. 5.22 for a trilayer system. In this case, the $(F^h(\phi), P^h(\phi))$ curve lies on the inside of a triangle and clear deviations from the straight-line observed in fig. 5.2 can be observed. As such, deviations from perfect linear behavior can be used as a visual aide to distinguish bilayer systems from multilayer systems.

So far, we have dealt with multilayer systems in which the spacing between consecutive layers is relatively large. In these cases the difference between the most grazing and least grazing slices is much larger than the expected spread of measured data points obtained using modern 3rd genera-

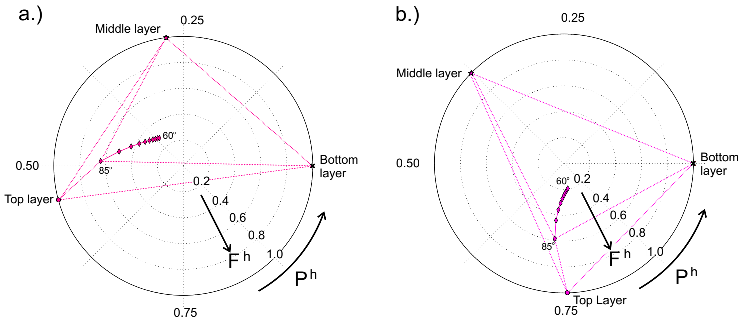

Figure 5.3: Coherent fraction and position as a function of electron take-off angle ϕ predicted by eq. 5.22 for $60° < \phi < 85°$ for a trilayer system consisting of three layers with equal number of emitters per layer and an equal inter-layer spacing between each consecutive layer, assuming a lattice spacing of $d_{hkl} = 2.36\,\text{Å}$ for the substrate generating the standing wave field and a photoelectron mean-free path of $\lambda_{in} = 30\,\text{Å}$ in the bilayer. The interlayer spacings are equal to a.) $d_L = 3.00\,\text{Å}$ and b.) $d_L = 3.25\,\text{Å}$

tion synchrotron light sources. However, as the interlayer spacing is reduced, so is the importance of attenuation and therefore it is useful to estimate the smallest interlayer spacing that would still be distinguishable. In order to analyze this, we first need a measure of the attainable resolution of the XSW method. For this, we use the absolute separation between two points in the Argand diagram, defined as:

$$\left|\Delta\vec{X}\right| = \left|F_1^h e^{2\pi i P_1^h} - F_2^h e^{2\pi i P_2^h}\right|. \tag{5.26}$$

In fig. 5.4 we have plotted the separation in the Argand diagram between the results obtained for a bilayer system from yield curves measured at an electron take-off angle of 85° and 60° according to eq. 5.22, as a function of the interlayer spacing d_L between the two layers for varying values of λ_{in} and assuming $d_{hkl} = 2.36\,\text{Å}$. It can clearly be seen that if data points separated by an absolute distance of $\left|\Delta\vec{X}\right| = 0.05$ can be reliable separated, then for most systems the minimum discernible interlayer spacing lies between 0.4 Å and 0.7 Å, which in some cases might be sufficient to discern adsorbates in hollow sites from those adsorbed in on-top sites. If the minimum discernible distance between points in the Argand diagram can be reduced to $\left|\Delta\vec{X}\right| = 0.01$ (which may be attainable for very stable systems of strong emitters) or if the mean-free path of the emitted electrons is very short (which can be the case for low energy Auger electrons), then the minimum discernible interlayer spacing can

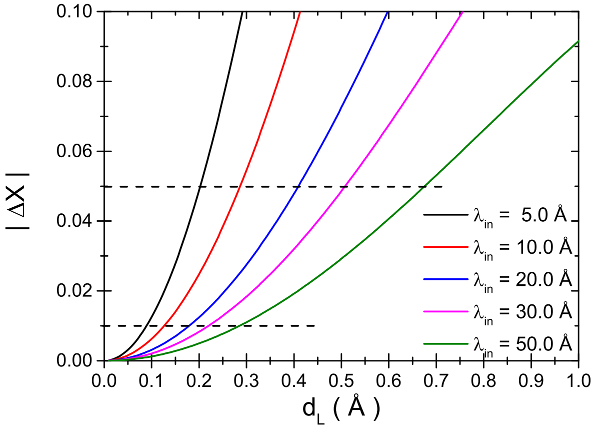

Figure 5.4: Separation $\left|\Delta\vec{X}\right|$ between points in the Argand diagram measured at electron take-off angles of 85° and 60°, for a bilayer system as a function of the interlayer spacing d_L and the photoelectron inelastic mean-free path λ_{in}

become as low as 0.2 Å. Such high accuracies would also open up possibilities for the analysis of disorder caused by, for example, buckling of graphene layers or the tilting of molecules. However, in those situations, the number of possible adsorption sites that have to be considered becomes very large and thus we can no longer approximate the system as a combination of Dirac-δ functions. In the next section we will present an alternative approximation that can be used for these situations.

5.3 Measuring disorder-induced effects: Slant and Clustering of the emitter distribution functions

When the number of adsorption sites contributing to measured XSW curves becomes larger than about 4 or 5, it becomes impossible to approximate the data using a discrete number of well-defined adsorption heights. In addition to that, when disorder is caused by the buckling of a monolayer or the tilting of a molecule, it is fundamentally no longer possible to approximate the distribution of emitters as a sum over discrete adsorption sites. This means that we need to develop a new method to analyze angle-resolved XSW data. Here we will present one such method, which does not rely on prior knowledge of details of the distribution function.

Recall from eq. 5.16 that the coherent position and fraction measured in the presence of attenuation effects can be written as:

$$F^h e^{2\pi i P^h} = \frac{\rho_{\mathfrak{B}}\left(s_d + s_i\right)}{\rho_{\mathfrak{B}}\left(s_d\right)} \tag{5.27}$$

$$\tag{5.28}$$

Now we apply a Taylor expansion to $\rho_{\mathfrak{B}}(s_d + s_i)$ around the point s_i to obtain:

$$\rho_{\mathfrak{B}}(s_i + s_d) = \rho_{\mathfrak{B}}(s_i) + s_d \rho_{\mathfrak{B}}^{(1)}(s_i) + \frac{s_d^2}{2!}\rho_{\mathfrak{B}}^{(2)}(s_i)\ldots \tag{5.29}$$

In the case where the inelastic mean-free path of photoelectrons is much larger than the width of the distribution function, $\rho_{\mathfrak{B}}(s_d+s_i)$ will be affected much more strongly by the attenuation effects than $\rho_{\mathfrak{B}}(s_d)$. As such, to a good approximation $\rho_{\mathfrak{B}}(s_d) = 1$. Further more, we can then also terminate the expansion of $\rho_{\mathfrak{B}}(s_i + s_d)$ after the second term. In that case, we can write eq. 5.16 as:

$$F^h e^{2\pi i P^h} \approx \rho_{\mathfrak{B}}(s_i) + s_d \rho_{\mathfrak{B}}^{(1)}(s_i). \tag{5.30}$$

In this equation, $\rho_{\mathfrak{B}}(s_i)$ corresponds to the coherent fraction and position that would be measured in the absence of attenuation effects, and the parameter $\rho_{\mathfrak{B}}^{(1)}(s_i)$ quantifies the effect of attenuation. However, this parameter is also the derivative of the function $\rho_{\mathfrak{B}}(s)$ at the point $s = s_i$, and as such it contains information about the shape of the distribution function. As discussed in the derivation of eq. 5.22, it is often beneficial to make the periodic nature of the XSW method explicit. We can do this by instead writing:

$$F^h e^{2\pi i P^h} \approx F_0^h e^{2\pi i P_0^h}\left(1 + s_d X^{(1)}\right) \tag{5.31}$$

$$= e^{2\pi i P_0^h} V(s_i, s_d) \tag{5.32}$$

$$X^{(1)} = \frac{\bar{\rho}_{\mathfrak{B}}^{(1)}(s_i)}{\bar{\rho}_{\mathfrak{B}}(s_i)}, \tag{5.33}$$

where we chose P_0^h so that $\bar{\rho}_{\mathfrak{B}}(s_i) = F_0^h$ is purely real. Now we again obtain a shape function $V(s_i, s_d) = F_0^h\left(1 + s_d X^{(1)}\right)$, which only depends on the coherent fraction F_0^h and on the parameter $X^{(1)}$. This parameter contains information about the shape of $\rho(z)$, just like $\rho^{(1)}_{\mathfrak{B}}$, however by the above procedure this information has been decoupled from the position of the center of $\rho(z)$, making it more straight-forward to interpret. In order to elucidate the kind of information we contain, we compute the expected values of $\bar{\rho}_{\mathfrak{B}}(s_i)$ and $\bar{\rho}^{(1)}_{\mathfrak{B}}(s_i)$ for a Gaussian distribution centered on the origin:

$$\bar{\rho}(z) = \frac{1}{\sqrt{2\pi\sigma^2}} e^{-\frac{1}{2}\left(\frac{z}{\sigma}\right)^2} \tag{5.34}$$

$$\bar{\rho}_{\mathfrak{B}}(s) = e^{\frac{1}{2}\sigma^2 s^2} \tag{5.35}$$

$$\bar{\rho}_{\mathfrak{B}}(s_i) = F_0^h = e^{-2\pi^2\left(\frac{\sigma}{d_{hkl}}\right)^2} \tag{5.36}$$

$$\bar{\rho}^{(1)}_{\mathfrak{B}}(s_i) = 2\pi i \frac{\sigma^2}{d_{hkl}} \bar{\rho}_{\mathfrak{B}}(s_i) \tag{5.37}$$

$$X^{(1)} = -\frac{i d_{hkl}}{\pi} \ln F_0^h. \tag{5.38}$$

The first thing we note is that $X^{(1)}$ is purely imaginary. Remember now that $\bar{\rho}_{\mathfrak{B}}(s_i)$ is the derivative with respect to the imaginary quantity $s_i = 2\pi i / d_{hkl}$. A purely imaginary value of $X^{(1)}$ thus implies that the derivative of $\bar{\rho}_{\mathfrak{B}}(s)$ is purely real. Evaluation of $\bar{\rho}_{\mathfrak{B}}(s)$ along the imaginary s-axis corresponds to the Fourier transform of $\bar{\rho}(z)$ and a purely real Fourier transform corresponds to an even function. Following this argument, we can say that for an arbitrary distribution function $R(z)$ (i.e. not necessarily a Gaussian distribution), if $X^{(1)}$ is not purely imaginary, then this implies that $R(z)$ is not symmetric w.r.t. reflections along the center of the distribution or in other words that the distribution is slanted in some way.

The second thing to note is that the magnitude of $X^{(1)}$ gives information about how strongly peaked the distribution function $R(z)$ is, or in other words, how much of the mass of the distribution is in the center of the distribution relative to the amount in the tails. A high value of $\left|X^{(1)}\right|$ means that the derivative of Fourier transform of $\rho(z)$ at s_i is high. Under the assumption that the Fourier transform of $\rho(z)$ is sufficiently smooth, this implies that the Fourier transform is strongly localized. This then immediately implies that the real-space distribution is less strongly localized, but because the standard deviation of the distribution is already fixed by F_0^h, $|X|$ must measure how strongly the tails of the distribution contribute relative to its center, or in other words it measures how strongly the distribution is clustered around the mean value.

In order to now quantify these two effects, we define two new parameters, S^h and K^h, which quantify the two aforementioned propperties of the distribution, according to

$$K^h e^{-2\pi i S^h} = -\frac{\pi X^{(1)}}{i d_{hkl} \ln \frac{1}{F_0^h}}. \tag{5.39}$$

In the following we will refer to S^H and K^H as the slant and clustering of the distribution function respectively.

Using this definition, for a Gaussian distribution, $K^h = 1$ and $S^h = 0$. A value of $K^h < 1$ implies that the tails of the distribution are more pronounced than they are for a Gaussian distribution, while $K^h > 1$ implies the opposite. Likewise, the magnitude of S^h indicates how strongly the distribution is skewed, while a positive sign indicates skewing in the direction of the vacuum and a negative sign indicates skewing in the direction of the bulk. In fig. 5.5a we have plotted the distribution function

$$\rho(z) = c e^{-\frac{1}{2}\left|\frac{z}{\sigma}\right|^p} \tag{5.40}$$

for $p = \{1, 1.5, 2\}$ with c a normalization constant and σ chosen to ensure that F_0^h is approximately equal for all 3 distributions. Figure 5.5c and d show values of F^h and P^h for these distributions obtained by direct numeric evaluation of eq. 5.16, assuming an inelastic mean-free path of $\lambda_{in} = 30\,\text{Å}$ and a periodicity of the standing wave field of $d_{hkl} = 2.36\,\text{Å}$. Although the attenuation effects are quite weak for this system, owing of course to the small width of the distribution function relative to the assumed inelastic mean-free path, the predicted changes in the coherent fraction and position should be measurable on very favorable systems. Also included are lines indicating the result of fitting these simulated data points with eq. 5.31. Finally, in fig. 5.5b we have plotted the value of K^h as function of p, showing that it indeed increases monotonically as mass is displaced from the tails of $\rho(z)$ to the center of the distribution.

Likewise, in fig. 5.6a we have plotted the distribution function

$$\rho(z) = 0.75\, c_1\, e^{-\frac{1}{2}\left(\frac{z}{\sigma}\right)^2} + 0.25\, c_2\, e^{-\frac{1}{2}\left(\frac{z-z_i}{\sigma}\right)^2} \tag{5.41}$$

with c again normalization constants, for $z_i = \{-1.0, 0.0, 1.0\}\text{Å}$ and with σ chosen to ensure approximately equal values of F_0^h. As before, we simulated the expected coherent fractions and positions that would be measured assuming an inelastic mean-free path of $\lambda_{in} = 30\,\text{Å}$ and a periodicity of the standing wave field of $d_{hkl} = 2.36\,\text{Å}$, and these data points are shown in fig. 5.6c and d as symbols, along with lines indicating fits of eq. 5.31 to these simulated data points. From these fits we then obtain the slant depicted in fig. 5.6b, showing that the presence of a second peak closer to the surface than the main peak leads to a negative value of S^h and that the presence of a second peak on the vacuum side of the main peak leads to a positive value of S^h.

5.4 Conclusions

We have shown that, under the assumption of a constant inelastic mean-free path and negligible contributions from diffraction effects, the attenuation of photoelectrons in XSW measurements can be incorporated straightforwardly in the mathematical formalism that describes the relationship between the shape of the emitter distribution curves and the measured yield curves. The effect of such an attenuation takes the form of an angular dependence in

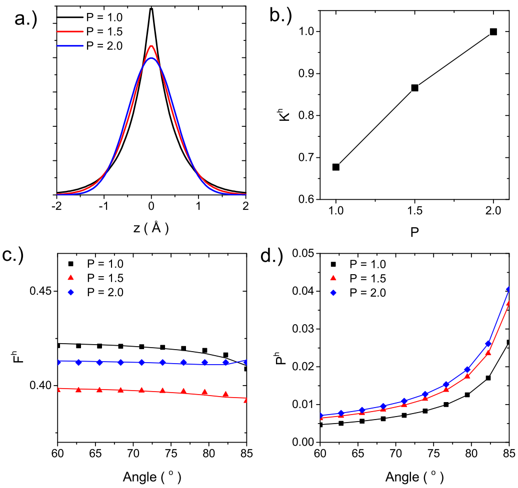

Figure 5.5: Effect of the importance of the tails of a distribution function on the clustering K^h. a.) shows 3 different distribution functions calculated using eq. 5.40 with varying values of p, and with σ chosen to ensure approximately equal coherent fractions. b.) shows the corresponding values of K^h obtained from fits to the simulated angle-dependent coherent fractions and positions depicted in c.) and d.). These data points (indicated with symbols) were simulated by direct numeric evaluation of eq. 5.16 for each distribution function, assuming an inelastic electron mean-free path of $\lambda_{in} = 30\,\text{Å}$ and a standing wave field periodicity $d_{hkl} = 2.36\,\text{Å}$. These simulated data points were subsequently fitted with eq. 5.31 to obtain K^h

the measured coherent fraction F^h and position P^h, which can be related to the Bilateral Laplace transform of the emitter distribution function. Furthermore, we have derived two techniques that, under certain assumptions, can recover information about the emitter distribution function. In the first of these two techniques, the system is assumed to consist of multiple well-ordered adsorption sites, which would be the case e.g. for a bilayer or trilayer system. In this case, the angle dependence of the coherent position and fraction can be interpreted as stemming from a linear interpolation of vectors in an Argand diagram. If the number of different adsorption sites is known then this can be used to recover the adsorption sites from the measured data.

The second technique does not require any prior assumptions about the system, other than that the distribution function is sufficiently narrow that

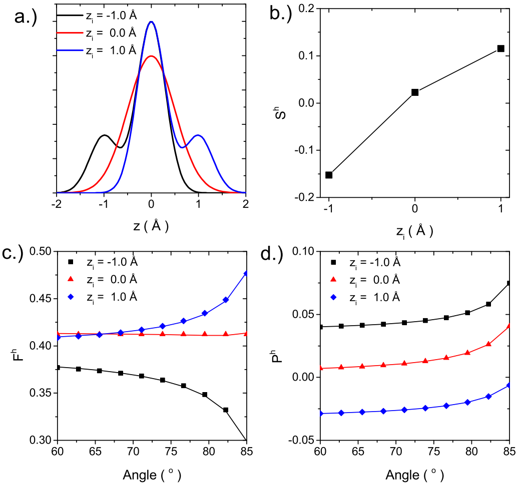

Figure 5.6: Effect of the presence of a second peak in a distribution function on the slant S^h. a.) shows 3 different distribution functions calculated using eq. 5.41 with varying values of z_i, and with σ chosen to ensure approximately equal coherent fractions. b.) shows the corresponding values of S^h obtained from fits to the simulated angle-dependent coherent fractions and positions depicted in c.) and d.). These data points (indicated with symbols) were simulated by direct numeric evaluation of eq. 5.16 for each distribution function, assuming an inelastic electron mean-free path of $\lambda_{in} = 30\,\text{Å}$ and a standing wave field periodicity $d_{hkl} = 2.36\,\text{Å}$. These simulated data points were fitted with eq. 5.31 to obtain S^h

attenuation effects are relatively weak. In this case, we can introduce two new parameters, the slant S^h and the clustering K^h. The measured data points can then be interpreted as stemming from a complex linear equation involving both the true coherent position and fraction, as well as the slant and clustering, and by fitting this equation to the data points it is possible to determine all 4 quantities. Further more, we have shown that the slant can be linked to the asymmetry or skewing of the distribution function, while the clustering can be related to how strongly peaked or localized the distribution function is.

Chapter 6

Conclusions

In this work, the heteromolecular metal-organic interface consisting of SnPc and PTCDA on Ag(111) has been studied and compared with the related system of CuPc and PTCDA on Ag(111). In addition to that, the state of the art of the NIXSW method has been advanced considerably by introducing a theoretical treatment of the effects of experimental geometry and attenuation of photoemission signals.

As described in Chapter 3, SPA-LEED and STM measurements have confirmed that the SnPc+PTCDA/Ag(111) system orders laterally in a way very similar to the CuPc+PTCDA/Ag(111) system. In both systems, both a AB_2 and a A_2B phase can be observed. In addition to that, the CuPc+PTCDA system displays an AB phase. Due to a difference in the interaction strength between the constituent molecules, in the SnPc+PTCDA system, this phase is not found. Instead, a A_2B phase was observed which has a unit cell incommensurate with the AB unit cell, indicating that it is not simply formed by expansion of the AB unit cell due to the presence of Sn-up and Sn-down SnPc molecules. Furthermore, and in contrast to the CuPc+PTCDA system, in the SnPc+PTCDA system the AB_2 phase does not change its precise unit cell parameters with increasing SnPc coverage, but that heating is needed to convert it from its least dense, commensurate form into a more dense, incommensurate structure. STM measurements reveal that this transition is associated with a doubling of the unit cell size caused by a sliding of the molecular rows relative to each other.

NIXSW measurements reveal that mixing PTCDA with SnPc leads to an increase of the PTCDA adsorption height, an effect that was also observed for the PTCDA+CuPc system, and which at first sight conflicts with the observation that upon mixing with a phthalocyanine molecule, the PTCDA-substrate bond is strengthened. For the CuPc+PTCDA system this behavior has been explained in[62] and we propose that a similar explanation is valid for SnPc+PTCDA. However, these measurements also reveal considerable differences between the SnPc+PTCDA/Ag(111) and CuPc+PTCDA/Ag(111) systems. The first notable difference is in the structure of the PTCDA anhydride groups. In the CuPc+PTCDA/Ag(111) A_2B phase the PTCDA molecule adopts an anhydride-up configuration, with the anhydride oxygen located above the perylene plane and the carboxylic oxygens below it, similar to the conformation found in homomolecular PTCDA layers on Ag(111). However, in the SnPc+PTCDA/Ag(111) A_2B phase it immediately adopts the anhydride-down configuration with all oxygen atoms below the perylene plane, which is similar to the conformation found in homomolecular layers on Ag(110) and in the AB_2 phase of both systems studied here.

Furthermore, when comparing the effect of mixing with PTCDA on the phthalocyanine molecules one also observes remarkable differences between CuPc and SnPc. While the adsorption height and conformation of CuPc is essentially unaffected by mixing with PTCDA, the adsorption height of SnPc changes considerably. It is observed that upon mixing the Sn atom is pulled down by over 0.2 Å, and the phthalocyanine ligand follows suit, causing the later to adopt the same adsorption height as found for CuPc.

Finally, through analysis of ARPES measurements with the photoemission tomography technique, a difference has been revealed in the behavior of the SnPc fLUMO upon mixing when compared to the CuPc fLUMO. In both systems a depletion of charge from the phthalocyanine fLUMO occurs as it is shifted to lower binding energies and simultaneously a downward shift and filling of the PTCDA fLUMO takes place. This charge transfer process from the MePc to the PTCDA molecule is complete for CuPc mixed with PTCDA, mixing of SnPc with PTCDA leads to an incomplete charge transfer and some electron density still remains in the SnPc fLUMO, although this does not seem to have a noticeable effect on the binding energy of the PTCDA fLUMO after mixing.

Finally,we show how all these effects can be rationalized in a charge reorganization model. In this model, the phthalocyanine molecules push away electron density in the substrate from their adsorption sites towards the PTCDA adsorption sites. The PTCDA molecules in contrast are charge acceptors, they tend to accept charge from the substrate. Upon mixing both molecules, this leads to a synergistic effect, causing charge to be transferred from the phthalocyanine molecules to the PTCDA molecules. Excess charge pushed towards the PTCDA adsorption sites but not taken up by these molecules leads to an increase of their adsorption height despite the increased surface-PTCDA bond strength. In this model, however, there is a significant difference between CuPc and SnPc. The SnPc central Sn atom is both much closer to the surface and much more easily capable of donating electrons than the CuPc central Cu atom. This means that when SnPc is mixed with PTCDA, more electron density becomes available compared to the CuPc+PTCDA mixed system. This extra electron density is partially used up to form local bonds to the anhydride oxygen atoms, explaining the different PTCDA anhydride conformations found in CuPc+PTCDA and

SnPc+PTCDA. Additionally, some of the extra electron density available is donated back into the SnPc fLUMO, explaining how it still retains some charge in its fLUMO after mixing with PTCDA. Finally, this transfer process leads to a strengthening of the local Sn-surface bond, which explains why SnPc moves so much closer to the surface upon mixing with PTCDA.

In the second part of this thesis, consisting of chapters 4 and 5, we have addressed more technical aspects of the NIXSW technique. Specifically, we have discussed two aspects that have so far been neglected in the analysis of NIXSW data: the precise experimental geometry in which the data has been recorded and the effect of the limited mean-free path of photoemitted electrons in the studied material.

In Chapter 4, it is shown that the equations traditionally used to calculate non-dipolar effects in NIXSW measurements do not properly account for the typical experimental geometries used. In particular, under typical experimental conditions the sample is tilted slightly to separate the Bragg diffracted beam from the incoming beam so that its intensity can be monitored. When the polarization of the beams lie in the plane of this tilt, which is typically the case due to experimental constraints, then this result in the polarization vector of the diffracted beam no longer being parallel to the polarization vector of the incoming beam. This leads to distortions of the angular emission patterns of photoelectrons beyond the distortions due to non-dipolar effects that would be expected if the incoming and diffracted beam were perfectly parallel. New expressions for calculating non-dipolar parameters have been derived that take these effects into account and using these new equations it has been shown that the deviations induced by neglecting the experimental geometry can be significant. In particular, two extreme cases have been analyzed. On the one hand, a perfectly disordered organic layer has been studied to obtain the non-dipolar parameter γ' for various elements. For this system it has been shown that neglecting the experimental geometry leads to a significant underestimation of γ'. On the other hand, when analyzing several well-ordered systems, it has been found that neglecting the experimental geometry leads to a deviation of the structural parameters, i.e. the coherent position and coherent fraction, which depends strongly on the particular system. For systems with a coherent fraction $P^h \approx 0.25$, the deviation is maximal and mainly affects the extracted coherent fraction F^h. For $P^h \approx 0.0$ and $P^h \approx 0.5$, the deviation is of intermediate magnitude and it affects both the extracted coherent position and coherent fraction, while for $P^h \approx 0.75$ the deviations are minimal. Finally, it has been found that these distortions strongly depend on the angle between the incident beam and emitted electron, which means that when working with modern wide-angle electron analyzers, all measurements have to be performed in an angle-resolved mode.

Finally, in Chapter 5, the theory of attenuation effects in NIXSW measurements is presented. It is shown that under the assumption that the dominant process affecting photoelectrons is inelastic scattering and with the assumption that the inelastic mean-free path is constant, it is possible to include attenuation effects in the theoretical treatment of the NIXSW method, which leads to a modified relationship between the actual distribution of emitters and the measured coherent fraction and position. In particular, it is found that the measured coherent position and fraction become angle-dependent and this angular dependence can be exploited to gain information about the distribution of atoms at the surface even when they cannot be chemically resolved. In particular, two different approaches are presented. In the first approach it is assumed that all atoms are found in a small number of discrete adsorption positions, e.g. they occupy different well-ordered layers. In this case it is possible to assign each species a coherent position, which can be interpreted as a vector in an Argand diagram. The measured coherent fraction and position are then given by a vector sum over these Argand vectors, but due to attenuation effects, the relative contribution of each Argand vector depends on the angle of the outgoing photoelectrons used to record the yield curve. In particular it is found that for a bilayer system, all measured coherent fractions and positions form a straight line in the Argand diagram which can be used as a straight-forward diagnostic tool. For more than 2 layers the relationship between angle and position in the Argand diagram becomes more complicated but if the number of layers is known or can be guessed on chemical grounds then the experimental data points can still be fitted to obtain the positions of all contributing layers.

In the second approach, no such restrictive assumption is made about the shape of the emitter distribution function. Instead, it is merely assumed that the distribution function is sufficiently narrow that the measured data points can be adequately described by a Taylor expansion to first order. It is shown that the Taylor coefficients obtained in this way can be related to the true coherent fraction and position of the distribution function in the absence of attenuation effects, to the degree to which the distribution function has been skewed towards or away from the bulk and to how strongly peaked the distribution function is.

In conclusion, we believe that both parts of this thesis represent a significant contribution to the state of the art in surface science. The first part improves the scientific understanding of intermolecular interactions that occur in heteromolecular organic-metal interfaces. The second part provides valuable insight into processes that affect the interpretation of measured NIXSW data. It is also independent of the specific adsorbate system and therefor of general validity for the analysis of photoelectron-monitored NIXSW data.

Bibliography

[1] Y. Yamashita, Sci. Technol. Adv. Mat. **10**, 024313 (2009).

[2] C. Reese, M. Roberts, M.-M. Ling, and Z. Bao, Mater. Today **7**, 20 (2004).

[3] H. Klauk, Chem. Soc. Rev. **39**, 2643 (2010).

[4] T. Hasegawa and J. Takeya, Sci. Technol. Adv. Mat. **10**, 024314 (2009).

[5] C. Dimitrakopoulos and P. Malenfant, Adv. Mater. **14**, 99 (2002).

[6] S. G. Surya, H. N. Raval, R. Ahmad, S. Sonar, K. N. Salama, and V. Ramgopal Rao, **111**, 27 (2019).

[7] J. Nelson, Curr. Opin. Solid St. M. **6**, 87 (2002).

[8] H. Hoppe and N. S. Sariciftci, J. Mater. Res. **19**, 1924 (2004).

[9] C. J. Brabec, S. Gowrisanker, J. J. M. Halls, D. Laird, S. Jia, and S. P. Williams, Adv. Mater. **22**, 3839 (2010).

[10] T. Ameri, P. Khoram, J. Min, and C. J. Brabec, Adv. Mater. **25**, 4245 (2013).

[11] O. A. Abdulrazzaq, V. Saini, S. Bourdo, E. Dervishi, and A. S. Biris, Particul. Sci. Technol. **31**, 427 (2013).

[12] O. Inganäs, Adv. Mater. **30**, 1800388 (2018).

[13] N. Thejo Kalyani and S. Dhoble, Renew. Sust. Energ. Rev. **16**, 2696 (2012).

[14] S. Reineke, M. Thomschke, B. Lüssem, and K. Leo, Rev. Mod. Phys. **85**, 1245 (2013).

[15] K. T. Kamtekar, A. P. Monkman, and M. R. Bryce, Adv. Mater. **22**, 572 (2010).

[16] B. W. D'Andrade and S. R. Forrest, Adv. Mater. **16**, 1585 (2004).

[17] W. Brütting, J. Frischeisen, T. D. Schmidt, B. J. Scholz, and C. Mayr, Phys. Status Solidi A **210**, 44 (2013).

[18] P. K. Bhatnagar, in *Nanomaterials and Their Applications (Advanced Structured Materials)*, edited by Z. H. Khan (Springer, Singapore, East Singapore, Singapore, 2018).

[19] S. R. Forrest, Nature **428**, 911 (2004).

[20] A. Kumatani, Y. Li, P. Darmawan, T. Minari, and K. Tsukagoshi, Sci. Rep. **3**, 1026 (2013).

[21] S. Forrest and P. Burrows, Supramol. Sci. **4**, 127 (1997).

[22] S. D. Oosterhout, M. M. Wienk, S. S. Van Bavel, R. Thiedmann, L. Jan Anton Koster, J. Gilot, J. Loos, V. Schmidt, and R. A. J. Janssen, Nat Mater **8**, 818 (2009).

[23] S. Mannsfeld, M. Toerker, T. Schmitz-Hübsch, F. Sellam, T. Fritz, and K. Leo, Org. Electron. **2**, 121 (2001).

[24] Y. Zou, L. Kilian, A. Schöll, T. Schmidt, R. Fink, and E. Umbach, Surf. Sci. **600**, 1240 (2006).

[25] A. Hauschild, R. Temirov, S. Soubatch, O. Bauer, A. Schöll, B. C. C. Cowie, T.-L. Lee, F. S. Tautz, and M. Sokolowski, Phys. Rev. B **81**, 125432 (2010).

[26] S. Henze, O. Bauer, T.-L. Lee, M. Sokolowski, and F. Tautz, Surf. Sci. **601**, 1566 (2007).

[27] G. Mercurio, O. Bauer, M. Willenbockel, N. Fairley, W. Reckien, C. H. Schmitz, B. Fiedler, S. Soubatch, T. Bredow, M. Sokolowski, and F. S. Tautz, Phys. Rev. B **87**, 045421 (2013).

[28] S. Duhm, A. Gerlach, I. Salzmann, B. Bröker, R. Johnson, F. Schreiber, and N. Koch, Org. Electron. **9**, 111 (2008).

[29] H. Aldahhak, W. Schmidt, and E. Rauls, Surf. Sci. **617**, 242 (2013).

[30] H. Zhang and L. Johansson, Chem. Phys. **439**, 71 (2014).

[31] S. Godlewski, A. Tekiel, W. Piskorz, F. Zasada, J. S. Prauzner-Bechcicki, Z. Sojka, and M. Szymonski, ACS Nano **6**, 8536 (2012).

[32] M. Wießner, D. Hauschild, A. Schöll, F. Reinert, V. Feyer, K. Winkler, and B. Krömker, Phys. Rev. B **86**, 045417 (2012).

[33] M. S. Dyer and M. Persson, New J. Phys. **12**, 063014 (2010).

[34] L. Romaner, D. Nabok, P. Puschnig, E. Zojer, and C. Ambrosch-Draxl, New J. Phys. **11**, 053010 (2009).

[35] H. Marchetto, U. Groh, T. Schmidt, R. Fink, H.-J. Freund, and E. Umbach, Chem. Phys. **325**, 178 (2006).

[36] B. Krause, A. C. Dürr, K. Ritley, F. Schreiber, H. Dosch, and D. Smilgies, Phys. Rev. B **66**, 235404 (2002).

[37] K. Glöckler, C. Seidel, A. Soukopp, M. Sokolowski, E. Umbach, M. Böhringer, R. Berndt, and W.-D. Schneider, Surf. Sci. **405**, 1 (1998).

[38] M. Rohlfing, R. Temirov, and F. S. Tautz, Phys. Rev. B **76**, 115421 (2007).

[39] J. Stanzel, W. Weigand, L. Kilian, H. Meyerheim, C. Kumpf, and E. Umbach, Surf. Sci. **571**, L311 (2004).

[40] M. Wießner, J. Ziroff, F. Forster, M. Arita, K. Shimada, P. Puschnig, A. Schöll, and F. Reinert, Nat. Commun. **4**, 1514 (2013).

[41] L. Kilian, U. Stahl, I. Kossev, M. Sokolowski, R. Fink, and E. Umbach, Surf. Sci. **602**, 2427 (2008).

[42] A. Bendounan, F. Forster, A. Schöll, D. Batchelor, J. Ziroff, E. Umbach, and F. Reinert, Surf. Sci. **601**, 4013 (2007).

[43] A. Schöll, Y. Zou, T. Schmidt, R. Fink, and E. Umbach, J. Phys. Chem. B **108**, 14741 (2004).

[44] C. Stadler, S. Hansen, A. Schöll, T.-L. Lee, J. Zegenhagen, C. Kumpf, and E. Umbach, New J. Phys. **9**, 50 (2007).

[45] A. Gerlach, F. Schreiber, S. Sellner, H. Dosch, I. A. Vartanyants, B. C. C. Cowie, T.-L. Lee, and J. Zegenhagen, Phys. Rev. B **71**, 205425 (2005).

[46] C. Kleimann, B. Stadtmüller, S. Schröder, and C. Kumpf, J. Phys. Chem. C **118**, 1652 (2014).

[47] B. Stadtmüller, I. Kröger, F. Reinert, and C. Kumpf, Phys. Rev. B **83**, 085416 (2011).

[48] C. Stadler, S. Hansen, F. Pollinger, C. Kumpf, E. Umbach, T.-L. Lee, and J. Zegenhagen, Phys. Rev. B **74**, 035404 (2006).

[49] M. Häming, M. Greif, C. Sauer, A. Schöll, and F. Reinert, Phys. Rev. B **82**, 235432 (2010).

[50] C. Stadler, S. Hansen, I. Kröger, C. Kumpf, and E. Umbach, Nat. Phys. **5**, 153 (2009).

[51] J. D. Baran, J. A. Larsson, R. A. J. Woolley, Y. Cong, P. J. Moriarty, A. A. Cafolla, K. Schulte, and V. R. Dhanak, Phys. Rev. B **81**, 075413 (2010).

[52] Y. Huang, E. Wruss, D. Egger, S. Kera, N. Ueno, W. Saidi, T. Bucko, A. Wee, and E. Zojer, Molecules **19**, 2969 (2014).

[53] J. D. Baran and J. A. Larsson, J. Phys. Chem. C **116**, 9487 (2012).

[54] R. Woolley, C. Martin, G. Miller, V. Dhanak, and P. Moriarty, Surf. Sci. **601**, 1231 (2007).

[55] J. M. Gottfried, Surf. Sci. Rep. **70**, 259 (2015).

[56] I. Kröger, B. Stadtmüller, and C. Kumpf, New J. Phys. **18**, 113022 (2016).

[57] I. Kröger, P. Bayersdorfer, B. Stadtmüller, C. Kleimann, G. Mercurio, F. Reinert, and C. Kumpf, Phys. Rev. B **86**, 195412 (2012).

[58] I. Kröger, B. Stadtmüller, C. Kleimann, P. Rajput, and C. Kumpf, Phys. Rev. B **83**, 195414 (2011).

[59] D. Duncan, W. Unterberger, K. Hogan, T. Lerotholi, C. Lamont, and D. Woodruff, Surf. Sci. **604**, 47 (2010).

[60] C. Bobisch, T. Wagner, A. Bannani, and R. Möller, J. Chem. Phys. **119**, 9804 (2003).

[61] B. Stadtmüller, S. Schröder, F. Bocquet, C. Henneke, C. Kleimann, S. Soubatch, M. Willenbockel, B. Detlefs, J. Zegenhagen, T.-L. Lee, F. Tautz, and C. Kumpf, Phys. Rev. B **89**, 161407 (2014).

[62] B. Stadtmüller, D. Lüftner, M. Willenbockel, E. M. Reinisch, T. Sueyoshi, G. Koller, S. Soubatch, M. G. Ramsey, P. Puschnig, F. S. Tautz, and C. Kumpf, Nat. Commun. **5**, 3685 (2014).

[63] B. Stadtmüller, C. Henneke, S. Soubatch, F. S. Tautz, and C. Kumpf, New J. Phys. **17**, 023046 (2015).

[64] B. Stadtmüller, S. Schröder, and C. Kumpf, J. Electron Spetrosc. Relat. Phenom. **204**, 80 (2015).

[65] B. Stadtmüller, *Study of intermolecular interactions in hetero-organic thin films*, Ph.D. thesis, Forschungszentrum, Zentralbibliothek, Jülich (2013).

[66] E. Goiri, M. Matena, A. El-Sayed, J. Lobo-Checa, P. Borghetti, C. Rogero, B. Detlefs, J. Duvernay, J. E. Ortega, and D. G. De Oteyza, Phys. Rev. Lett. **112**, 117602 (2014).

[67] A. El-Sayed, P. Borghetti, E. Goiri, C. Rogero, L. Floreano, G. Lovat, D. J. Mowbray, J. L. Cabellos, Y. Wakayama, A. Rubio, J. E. Ortega, and D. G. De Oteyza, ACS Nano **7**, 6914 (2013).

[68] J. L. Cabellos, D. J. Mowbray, E. Goiri, A. El-Sayed, L. Floreano, D. G. De Oteyza, C. Rogero, J. E. Ortega, and A. Rubio, J. Phys. Chem. C **116**, 17991 (2012).

[69] A. El-Sayed, D. J. Mowbray, J. M. García-Lastra, C. Rogero, E. Goiri, P. Borghetti, A. Turak, B. P. Doyle, M. DellAngela, L. Floreano, Y. Wakayama, A. Rubio, J. E. Ortega, and D. G. De Oteyza, J. Phys. Chem. C **116**, 4780 (2012).

[70] E. Goiri, P. Borghetti, A. El-Sayed, J. E. Ortega, and D. G. De Oteyza, Adv. Mater. **28**, 1340 (2016).

[71] M. Horn-von Hoegen, Z. Krist.-Cryst. Mater. **214**, 591 (1999).

[72] H. Lüth, *Solid surfaces, interfaces and thin films* (Springer-Verlag, Heidelberg; New York, 2010).

[73] C. Stellwag, G. Held, and D. Menzel, Surf. Sci. **325**, L379 (1995).

[74] T. Sirtl, J. Jelic, J. Meyer, K. Das, W. M. Heckl, W. Moritz, J. Rundgren, M. Schmittel, K. Reuter, and M. Lackinger, Phys. Chem. Chem. Phys. **15**, 11054 (2013).

[75] K. Heinz, Rep. Prog. Phys. **58**, 637 (1995).

[76] R. L. Park and H. H. Madden, Surf. Sci. **11**, 188 (1968).

[77] S. Agnoli, T. Onur Menteş, M. A. Niño, A. Locatelli, and G. Granozzi, Phys. Chem. Chem. Phys. **11**, 3727 (2009).

[78] P. Bayersdorfer, *SPA-LEED-Studie zur Adsorption von metallfreien Phthalocyaninen auf Ag(111) im Bereich kleiner Bedeckungen*, Ph.D. thesis, Universität Würzburg, Würzburg (2008).

[79] D. E. Hooks, T. Fritz, and M. D. Ward, Adv. Mater. **13**, 227 (2001).

[80] F. C. Frank and J. H. Van Der Merwe, P. R. Soc. A. **198**, 216 (1949).

[81] I. Kröger, B. Stadtmüller, C. Stadler, J. Ziroff, M. Kochler, A. Stahl, F. Pollinger, T.-L. Lee, J. Zegenhagen, F. Reinert, and C. Kumpf, New J. Phys. **12**, 083038 (2010).

[82] U. Scheithauer, G. Meyer, and M. Henzler, Surf. Sci. **178**, 441 (1986).

[83] I. Kröger, *Adsorption von Phthalocyaninen auf Edelmetalloberflächen*, Ph.D. thesis, Universität Würzburg, Würzburg (2011).

[84] M. Henzler, Surf. Sci. **152-153**, 963 (1985).

[85] J. Als-Nielsen, *Elements of modern X-ray physics*, 2nd ed. (Wiley, Hoboken, 2011).

[86] I. Fernández Torrente, K. J. Franke, and J. Ignacio Pascual, J. Phys.: Condens. Matter **20**, 184001 (2008).

[87] P. J. Feibelman and D. E. Eastman, Phys. Rev. B **10**, 4932 (1974).

[88] W. D. Grobman, Phys. Rev. B **17**, 4573 (1978).

[89] P. Puschnig, S. Berkebile, A. J. Fleming, G. Koller, K. Emtsev, T. Seyller, J. D. Riley, C. Ambrosch-Draxl, F. P. Netzer, and M. G. Ramsey, Science **326**, 702 (2009).

[90] B. Stadtmüller, M. Willenbockel, E. M. Reinisch, T. Ules, F. C. Bocquet, S. Soubatch, P. Puschnig, G. Koller, M. G. Ramsey, F. S. Tautz, and C. Kumpf, EPL **100**, 26008 (2012).

[91] P. Puschnig, E.-M. Reinisch, T. Ules, G. Koller, S. Soubatch, M. Ostler, L. Romaner, F. S. Tautz, C. Ambrosch-Draxl, and M. G. Ramsey, Phys. Rev. B **84**, 235427 (2011).

[92] P. Puschnig, A. D. Boese, M. Willenbockel, M. Meyer, D. Lüftner, E. M. Reinisch, T. Ules, G. Koller, S. Soubatch, M. G. Ramsey, and F. S. Tautz, J. Phys. Chem. Lett. **8**, 208 (2017).

[93] X. Yang, L. Egger, J. Fuchsberger, M. Unzog, D. Lüftner, H. F., P. Hurdax, M. Jugovac, G. Zamborlini, V. Feyer, G. Koller, P. Puschnig, F. S. Tautz, M. G. Ramsey, and S. Soubatch, J. Phys. Chem. Lett. **10**, 6438 (2019).

[94] F. Allegretti, D. Woodruff, V. Dhanak, C. Mariani, F. Bussolotti, and S. DAddato, Surface Science **598**, 253 (2005).

[95] S. Duhm, C. Bürker, J. Niederhausen, I. Salzmann, T. Hosokai, J. Duvernay, S. Kera, F. Schreiber, N. Koch, N. Ueno, and A. Gerlach, ACS Appl. Mater. Interfaces **5**, 9377 (2013).

[96] J. M. Gottfried, New J. Phys. **18**, 111002 (2016).

[97] I. Shuttleworth, C. Fisher, J. Lee, R. G. Jones, and D. Woodruff, Chem. Phys. Lett. **351**, 208 (2002).

[98] O. Bauer, G. Mercurio, M. Willenbockel, W. Reckien, C. Heinrich Schmitz, B. Fiedler, S. Soubatch, T. Bredow, F. S. Tautz, and M. Sokolowski, Phys. Rev. B **86**, 235431 (2012).

[99] B. Stadtmüller, T. Sueyoshi, G. Kichin, I. Kröger, S. Soubatch, R. Temirov, F. S. Tautz, and C. Kumpf, Phys. Rev. Lett. **108**, 106103 (2012).

[100] H. Yamane, A. Gerlach, S. Duhm, Y. Tanaka, T. Hosokai, Y. Y. Mi, J. Zegenhagen, N. Koch, K. Seki, and F. Schreiber, Phys. Rev. Lett. **105**, 046103 (2010).

[101] S. Entani, L. Y. Antipina, P. V. Avramov, M. Ohtomo, Y. Matsumoto, N. Hirao, I. Shimoyama, H. Naramoto, Y. Baba, P. B. Sorokin, and S. Sakai, Nano Res. **8**, 1535 (2015).

[102] I. A. Vartanyants and J. Zegenhagen, in *The X-ray Standing Wave Technique* (World Scientific Pub Co Pte Lt, 2013) pp. 181–215.

[103] G. Binnig, H. Rohrer, C. Gerber, and E. Weibel, Appl. Phys. Lett. **40**, 178 (1982).

[104] J. Tersoff and D. R. Hamann, Phys. Rev. B **31**, 805 (1985).

[105] G. Van Straaten, M. Franke, S. Soubatch, B. Stadtmüller, D. A. Duncan, T.-L. Lee, F. S. Tautz, and C. Kumpf, J. Phys. Chem. C **122**, 8491 (2018).

[106] S. Braun, W. R. Salaneck, and M. Fahlman, Adv. Mater. **21**, 1450 (2009).

[107] D. Natali and M. Caironi, Adv. Mater. **24**, 1357 (2012).

[108] M. Oehzelt, N. Koch, and G. Heimel, Nat. Commun. **5**, 4174 (2014).

[109] F.-J. Meyer zu Heringdorf, M. C. Reuter, and R. M. Tromp, Nature **412**, 517 (2001).

[110] M. Häming, A. Schöll, E. Umbach, and F. Reinert, Phys. Rev. B **85**, 235132 (2012).

[111] M. Willenbockel, B. Stadtmüller, K. Schönauer, F. C. Bocquet, D. Lüftner, E. M. Reinisch, T. Ules, G. Koller, C. Kumpf, S. Soubatch, P. Puschnig, M. G. Ramsey, and F. S. Tautz, New J. Phys. **15**, 033017 (2013).

[112] J. Ziroff, S. Hame, M. Kochler, A. Bendounan, A. Schöll, and F. Reinert, Phys. Rev. B **85**, 161404 (2012).

[113] M. Willenbockel, D. Lüftner, B. Stadtmüller, G. Koller, C. Kumpf, S. Soubatch, P. Puschnig, M. G. Ramsey, and F. S. Tautz, Phys. Chem. Chem. Phys. **17**, 1530 (2015).

[114] B. Stadtmüller, N. Haag, J. Seidel, G. van Straaten, M. Franke, C. Kumpf, C. M. Cinchetti, and M. Aeschlimann, Phys. Rev. B **94**, 235436 (2016).

[115] B. Stadtmüller, J. Seidel, N. Haag, L. Grad, C. Tusche, G. van Straaten, M. Franke, J. Kirschner, C. Kumpf, C. M. Cinchetti, and M. Aeschlimann, Phys. Rev. Lett. **117**, 096805 (2016).

[116] P. Gargiani, M. Angelucci, C. Mariani, and M. G. Betti, Phys. Rev. B **81**, 085412 (2010).

[117] P. Gargiani, G. Rossi, R. Biagi, V. Corradini, M. Pedio, S. Fortuna, A. Calzolari, S. Fabris, J. C. Cezar, N. B. Brookes, and M. G. Betti, Phys. Rev. B **87**, 165407 (2013).

[118] Y. L. Huang, W. Chen, F. Bussolotti, T. C. Niu, A. T. S. Wee, N. Ueno, and S. Kera, Phys. Rev. B **87**, 085205 (2013).

[119] H. Karacuban, M. Lange, J. Schaffert, O. Weingart, T. Wagner, and R. Möller, Surf. Sci. **603**, L39 (2009).

[120] A. Mugarza, R. Robles, C. Krull, R. Korytár, N. Lorente, and P. Gambardella, Phys. Rev. B **85**, 155437 (2012).

[121] E. Salomon, P. Amsalem, N. Marom, M. Vondracek, L. Kronik, N. Koch, and T. Angot, Phys. Rev. B **87**, 075407 (2013).

[122] T. Stock and J. Nogami, Appl. Phys. Lett. **104**, 071601 (2014).

[123] A. J. Heeger, Adv. Mater. **26**, 10 (2014).

[124] B. Lüssem, M. Riede, and K. Leo, Phys. Status Solidi A **210**, 9 (2013).

[125] C. Henneke, J. Felter, D. Schwarz, F. Stefan Tautz, and C. Kumpf, Nat. Mater. **16**, 628 (2017).

[126] Y. L. Huang, W. Chen, H. Li, J. Ma, J. Pflaum, and A. T. S. Wee, Small **6**, 70 (2010).

[127] S. Fortuna, P. Gargiani, M. G. Betti, C. Mariani, A. Calzolari, S. Modesti, and S. Fabris, J. Phys. Chem. C **116**, 6251 (2012).

[128] D. A. Egger, V. G. Ruiz, W. A. Saidi, T. Bučko, A. Tkatchenko, and E. Zojer, J. Phys. Chem. C **117**, 3055 (2013).

[129] G. Van Straaten, M. Franke, F. C. Bocquet, F. S. Tautz, and C. Kumpf, J. Electron Spetrosc. **222**, 106 (2018).

[130] (2017), tORRICELLI is an XSW data analysis and simulation program written by G. Mercurio, M. Franke and F. C. Bocquet. Copies can be obtained from the authors of this publication.

[131] I. K. Robinson, W. K. Waskiewicz, P. H. Fuoss, J. B. Stark, and P. A. Bennett, Phys. Rev. B **33**, 7013 (1986).

[132] I. K. Robinson and D. J. Tweet, Rep. Prog. Phys. **55**, 599 (1992).

[133] H. Meyerheim and W. Moritz, Appl. Phys. A **67**, 645 (1998).

[134] C. Kumpf, O. Bunk, J. Zeysing, M. Nielsen, M. Nielsen, R. Johnson, and R. Feidenhans'l, Surf. Sci. **448**, L213 (2000).

[135] C. Kumpf, D. Smilgies, E. Landemark, M. Nielsen, R. Feidenhans'l, O. Bunk, J. H. Zeysing, Y. Su, R. L. Johnson, L. Cao, J. Zegenhagen, B. O. Fimland, L. D. Marks, and D. Ellis, Phys. Rev. B **64**, 075307 (2001).

[136] T.-L. Lee, C. Kumpf, A. Kazimirov, P. F. Lyman, G. Scherb, M. J. Bedzyk, M. Nielsen, R. Feidenhans'l, R. L. Johnson, B. O. Fimland, and J. Zegenhagen, Phys. Rev. B **66**, 235301 (2002).

[137] C. Kumpf, W. Weigand, A. Müller, J. Wagner, V. Wagner, P. Bach, G. Schmidt, L. Molenkamp, J. Geurts, and E. Umbach, Phys. Stat. Sol. (c) **4**, 3183 (2007).

[138] D. Woodruff, Surf. Sci. Rep. **62**, 1 (2007).

[139] D. Kreikemeyer-Lorenzo, W. Unterberger, D. A. Duncan, M. K. Bradley, T. J. Lerotholi, J. Robinson, and D. P. Woodruff, Phys. Rev. Lett. **107**, 046102 (2011).

[140] D. Kreikemeyer Lorenzo, M. Bradley, W. Unterberger, D. Duncan, T. Lerotholi, J. Robinson, and D. Woodruff, Surf. Sci. **605**, 193 (2011).

[141] D. Woodruff, Nucl. Instr. Meth. Phys. Res. **547**, 187 (2005).

[142] D. Woodruff, Prog. Surf. Sci. **57**, 1 (1998).

[143] J. Zegenhagen, Surf. Sci. **554**, 77 (2004).

[144] R. G. Jones, A. S. Y. Chan, M. G. Roper, M. P. Skegg, I. G. Shuttleworth, C. J. Fisher, G. J. Jackson, J. J. Lee, D. P. Woodruff, N. K. Singh, and B. C. C. Cowie, J. Phys.: Condens. Matter **14**, 4059 (2002).

[145] L. Kilian, W. Weigand, E. Umbach, A. Langner, M. Sokolowski, H. L. Meyerheim, H. Maltor, B. C. C. Cowie, T. Lee, and P. Bäuerle, Phys. Rev. B **66**, 075412 (2002).

[146] G. Mercurio, R. J. Maurer, W. Liu, S. Hagen, F. Leyssner, P. Tegeder, J. Meyer, A. Tkatchenko, S. Soubatch, K. Reuter, and F. S. Tautz, Phys. Rev. B **88**, 035421 (2013).

[147] B. Stadtmüller, M. Willenbockel, S. Schröder, C. Kleimann, E. Reinisch, T. Ules, S. Soubatch, P. Puschnig, G. Koller, M. Ramsey, F. Tautz, and C. Kumpf, Phys. Rev. B **91**, 155433 (2015).

[148] B. Stadtmüller, M. Gruenewald, J. Peuker, R. Forker, T. Fritz, and C. Kumpf, J. Phys. Chem. C **118**, 28592 (2014).

[149] J. R. Patel and J. A. Golovchenko, Phys. Rev. Lett. **50**, 1858 (1983).

[150] B. W. Batterman, Phys. Rev. Lett. **22**, 703 (1969).

[151] J. A. Golovchenko, B. W. Batterman, and W. L. Brown, Phys. Rev. B **10**, 4239 (1974).

[152] S. K. Andersen, J. A. Golovchenko, and G. Mair, Phys. Rev. Lett. **37**, 1141 (1976).

[153] S. Thiess, T.-L. Lee, C. Aruta, C. T. Lin, F. Venturini, N. B. Brookes, B. C. C. Cowie, and J. Zegenhagen, Phys. Rev. B **92**, 075117 (2015).

[154] T.-L. Lee, C. Bihler, W. Schoch, W. Limmer, J. Daeubler, S. Thieß, M. S. Brandt, and J. Zegenhagen, Phys. Rev. B **81**, 235207 (2010).

[155] J. A. Golovchenko, J. R. Patel, D. R. Kaplan, P. L. Cowan, and M. J. Bedzyk, Phys. Rev. Lett. **49**, 560 (1982).

[156] G. Materlik, A. Frahm, and M. J. Bedzyk, Phys. Rev. Lett. **52**, 441 (1984).

[157] L. Cheng, P. Fenter, M. J. Bedzyk, and N. C. Sturchio, Phys. Rev. Lett. **90**, 255503 (2003).

[158] V. Kohli, M. J. Bedzyk, and P. Fenter, Phys. Rev. B **81**, 054112 (2010).

[159] J. S. Okasinski, C.-Y. Kim, D. A. Walko, and M. J. Bedzyk, Phys. Rev. B **69**, 041401 (2004).

[160] S. Stoltz, D. Ellis, and M. Bedzyk, Surface Science **633**, 8 (2015).

[161] D. P. Woodruff, Rep. Prog. Phys. **68**, 743 (2005).

[162] B. Krässig, M. Jung, D. S. Gemmell, E. P. Kanter, T. Lebrun, S. H. Southworth, and L. Young, Phys. Rev. Lett. **75**, 4736 (1995).

[163] I. A. Vartanyants and J. Zegenhagen, Soild State Commun. **113**, 299 (1999).

[164] J. Lee, C. Fisher, D. Woodruff, M. Roper, R. Jones, and B. Cowie, Surf. Sci. **494**, 166 (2001).

[165] I. Vartanyants, T.-L. Lee, S. Thiess, and J. Zegenhagen, Nucl. Instr. Meth. Phys. Res. **547**, 196 (2005).

[166] J. A. Prins, Z. Physik **63**, 477 (1930).

[167] F. Schreiber, K. Ritley, I. Vartanyants, H. Dosch, J. Zegenhagen, and B. Cowie, Surf. Sci. **486**, L519 (2001).

[168] J. W. Cooper, Phys. Rev. A **47**, 1841 (1993).

[169] M. Trzhaskovskaya, V. Nefedov, and V. Yarzhemsky, Atom. Data Nucl. Data **77**, 97 (2001).

[170] A. Hauschild, K. Karki, B. C. C. Cowie, M. Rohlfing, F. S. Tautz, and M. Sokolowski, Phys. Rev. Lett. **94**, 036106 (2005).

[171] M. Eremtchenko, D. Bauer, J. A. Schaefer, and F. S. Tautz, New J. Phys. **6**, 4 (2004).

[172] J. Sforzini, L. Nemec, T. Denig, B. Stadtmüller, T.-L. Lee, C. Kumpf, S. Soubatch, U. Starke, P. Rinke, V. Blum, F. C. Bocquet, and F. S. Tautz, Phys. Rev. Lett. **114**, 106804 (2015).

[173] J. D. Emery, B. Detlefs, H. J. Karmel, L. O. Nyakiti, D. K. Gaskill, M. C. Hersam, J. Zegenhagen, and M. J. Bedzyk, Phys. Rev. Lett. **111**, 215501 (2013).

[174] C. Fadley, R. Baird, W. Siekhaus, T. Novakov, and S. Bergström, J. Electron Spetrosc. **4**, 93 (1974).

[175] P. J. Cumpson, J. Electron Spetrosc. **73**, 25 (1995).

[176] B. Lesiak, A. Jablonski, Z. Prussak, and P. Mrozek, Surf. Sci. **223**, 213 (1989).

List of Figures

List of publications

Published papers included in this thesis:

Role of the central metal atom in substrate-mediated molecular interactions in phthalocyanine-based heteromolecular monolayers
G. van Straaten, *M. Franke, S. Soubatch, B. Stadtmüller, D. A. Duncan, T.-L. Lee, F. S. Tautz and C. Kumpf*
Journal of Physical Chemistry C **122** (15) (2018) 8491-8504

Non-dipolar effects in photoelectron-based normal incidence X-ray standing wave experiments
G. van Straaten, *M. Franke, F. C. Bocquet, F. S. Tautz and C. Kumpf*
Journal of Electron Spectroscopy and Related Phenomena **222** (2018) 106-116

Published papers not included in this thesis:

Structural and electronic properties of nitrogen-doped graphene
J. Sforzini, P. Hapala, M. Franke, ***G. van Straaten****, A. Stöhr, S. Link, S. Soubatch, P. Jelínek, T.-L. Lee, U. Starke, M. Švec, F. C. Bocquet and F. S. Tautz*
Physical Review Letters **116** (12) (2016) 126805

Modifying the surface of a Rashba-split Pb-Ag alloy using tailored metal-organic bonds
B. Stadtmüller, J. Seidel, N. Haag, L. Grad, C. Tusche, ***G. van Straaten****, M. Franke, J. Kirschner, C. Kumpf, M. Cinchetti, M. Aeschlimann*
Physical Review Letters **117** (9) (2016) 096805

Adsorption heights and bonding strength of organic molecules on a Pb-Ag surface alloy
B. Stadtmüller, N. Haag, J. Seidel, ***G. van Straaten****, M. Franke, C. Kumpf, M. Cinchetti, M. Aeschlimann*
Physical Review B **94** (23) (2016) 235436

Fully atomistic understanding of the Eelectronic and optical properties of a prototypical doped charge-transfer interface
A. Baby, M. Gruenewald, C. Zwick, F. Otto, R. Forker, ***G. van Straaten****, M. Franke, B. Stadtmüller, C. Kumpf, G. P. Brivio, G. Fratesi, T. Fritz, E. Zojer*
ACS Nano **11** (2017) 10495-10508

Atomic Layer Deposition of Cobalt Using H_2-, N_2-, and NH_3-Based Plasmas: On the Role of the Co-reactant
M. F. J. Vos, ***G. van Straaten****, W. M. M. Kessels, A. J. M. Mackus*
Journal of Physical Chemistry C **122** (39) (2018) 22519-22529

Torricelli: A software to determine atomic spatial distributions from normal incidence x-ray standing wave data
F. C. Bocquet, G. Mercurio, M. Franke, ***G. van Straaten****, S. Weiss, S. Soubatch, C. Kumpf, F. S. Tautz*
Computer Physics Communications **235** (2019) 502-513

Acknowledgments

I would hereby like to acknowledge all people who have made the present work possible, first among them being Prof. Dr. Christian Kumpf. I sincerely appreciate him giving me the opportunity to carry out my PhD thesis, as well as his continual support, encouragement and guidance.

I would also like to extend my gratitude to Prof. Dr. Moritz Sokolowski and Prof. Dr. Uwe Klemradt for taking the time to co-referee my thesis.

In addition to that, I thank my colleagues at the PGI-3 institute, first among them Dr. Serguey Soubatch, for making possible some of the measurements presented in this work, as well as for his extensive support during many synchrotron beam times. Further thanks I extend to Dr. Sonja Schröder, Dr. Caroline Henneke, Dr. François Posseik, Markus Franke, Dr. Janina Keller, Simon Weiss, Xiaosheng Yang, Matthew Green, Philipp Leinen and Helmut Stollwerk. Their moral and technical support, as well as the many discussions we have had were indispensable for this project and without them this thesis would have been just a pipe dream.

I would further like to acknowledge Jun-Prof. Dr. Benjamin Stadtmüller, Johannes Seidel and Dr. Norman Haag from the University of Kaiserslautern, Prof. Dr. Torsten Fritz, Dr. Roman Forker and Dr. Marco Grünewald from the University of Jena, Ina Krieger and Prof. Dr. Moritz Sokolowski from the University of Bonn for our fruitful collaborations. In addition to that I would like to thank Prof. Dr. Peter Puschnig from the University of Graz in particular for his support in the photoemission tomography analysis presented in chapter 3, as well as Prof. Dr. Phill Woodruff from Warwick University and Dr. Jörg Zegenhagen from Diamond Light Source for fruitful discussions that contributed greatly to the results presented in chapter 4.

I am also grateful to all the staff of the I09 beamline, in particular T.-L. Lee, P. K. Thakur and D. McCue. (Diamond Light Source, Didcot, United Kingdom) for their technical and scientific support, and for going above and beyond in providing assistance even during weekends and in the middle of the night.

My final thanks goes out to my friends back in the Netherlands as well as to all the friends I made in Germany during this PhD project, and to my parents, who never let the border between us affect their unwavering support for me.

Curriculum Vitae

Gerben van Straaten
born on November 7th. 1990 in Son en Breugel, the Netherlands.
Nationality: Dutch.

Education

2008 Graduated from Udens College, Uden, The Netherlands.

2008-2012 Bachelor of Science study in Chemical Engineering & Chemistry at Eindhoven University of Technology.

2012 Bachelor of Science degree.
Thesis title: *Nucleation kinetics of porphyrine stacking.*
Advisor: Dr. Pieter A. Korevaar & Prof. Dr. Bert Meijer.

2011-2013 Master of Science study in Chemical Engineering & Chemistry at Eindhoven University of Technology.

2013 Master of Science Degree
Thesis title: *The effect of applied voltage and temperature on charge separation in OPVs.*
Advisors: Dr. Stefan C. J. Meskers & Prof. Dr. Rene Janssen.

2013-2017 PhD student at Peter Grünberg Institut (PGI-3), Forschungszentrum Jülich.
Thesis title: *Geometric and Electronic Properties of Heteromolecular Organic Monolayers on Noble Metal Substrates Studied by Photoemission Spectroscopy and X-ray Standing Waves.*
Advisor: Prof. C. Kumpf.

Since September 2017 Postdoctoral Researcher at Department of Applied Physics, Eindhoven University of Technology

Band / Volume 222
Tools and Workflows for Data & Metadata Management of Complex Experiments
Building a Foundation for Reproducible & Collaborative Analysis in the Neurosciences
J. Sprenger (2020), X, 168 pp
ISBN: 978-3-95806-478-2

Band / Volume 223
Engineering of *Corynebacterium glutamicum* towards increased malonyl-CoA availability for polyketide synthesis
L. Milke (2020), IX, 117 pp
ISBN: 978-3-95806-480-5

Band / Volume 224
Morphology and electronic structure of graphene supported by metallic thin films
M. Jugovac (2020), xi, 151 pp
ISBN: 978-3-95806-498-0

Band / Volume 225
Single-Molecule Characterization of FRET-based Biosensors and Development of Two-Color Coincidence Detection
H. Höfig (2020), XVIII, 160 pp
ISBN: 978-3-95806-502-4

Band / Volume 226
Development of a transcriptional biosensor and reengineering of its ligand specificity using fluorescence-activated cell sorting
L. K. Flachbart (2020), VIII, 102 pp
ISBN: 978-3-95806-515-4

Band / Volume 227
Strain and Tool Development for the Production of Industrially Relevant Compounds with *Corynebacterium glutamicum*
M. Kortmann (2021), II, 138 pp
ISBN: 978-3-95806-522-2

Band / Volume 228
Complex magnetism of nanostructures on surfaces: from orbital magnetism to spin excitations
S. Brinker (2021), III, 208 pp
ISBN: 978-3-95806-525-3

Band / Volume 229
High-throughput All-Electron Density Functional Theory Simulations for a Data-driven Chemical Interpretation of X-ray Photoelectron Spectra
J. Bröder (2021), viii, 169, XL pp
ISBN: 978-3-95806-526-0

Band / Volume 230
Molecular tools for genome engineering of *Corynebacterium glutamicum*
C. K. Sonntag (2021), VIII, 111 pp
ISBN: 978-3-95806-532-1

Band / Volume 231
Interface Functionalization of Magnetic Oxide $Fe_3O_4/SrTiO_3$ Heterostructures
M. H. A. Hamed (2021), xvii, 151 pp
ISBN: 978-3-95806-535-2

Band / Volume 232
Optically induced magnetization reversal in Co/Pt multilayers
Role of domain wall dynamics
U. Parlak (2021), ix, 162, XII pp
ISBN: 978-3-95806-536-9

Band / Volume 233
Application of Silicon Photomultipliers in Neutron Detectors
S. Kumar (2021), xxvi, 157 pp
ISBN: 978-3-95806-537-6

Band / Volume 234
Towards Magneto-Elastomeric Nanocomposites with Supramolecular Activity
L. S. Fruhner (2021), XVI, 213 pp
ISBN: 978-3-95806-538-3

Band / Volume 235
Geometric and Electronic Properties of Heteromolecular Organic Monolayers on Noble Metal Substrates Studied by Photoemission Spectroscopy and X-ray Standing Waves
G. van Straaten (2021), vii, 115 pp
ISBN: 978-3-95806-539-0

Weitere ***Schriften des Verlags im Forschungszentrum Jülich*** unter
http://wwwzb1.fz-juelich.de/verlagextern1/index.asp

Schlüsseltechnologien / Key Technologies
Band / Volume 235
ISBN 978-3-95806-539-0

Mitglied der Helmholtz-Gemeinschaft

JÜLICH
Forschungszentrum